UCLouvain
Institute of Mechanics,
Materials and Civil Engineering

Numerical methods for granular media in multiphase fluids

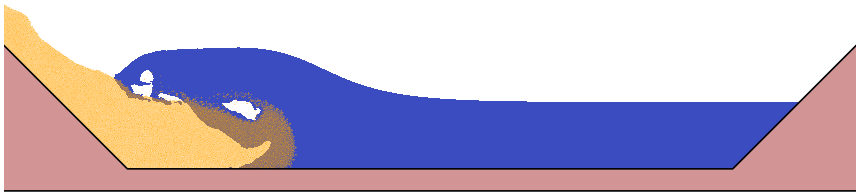

Michel Henry

Thesis typescript submitted in partial fulfilment of the requirements
for the Ph.D Degree in Engineering Science

Thesis Committee

Advisors	Vincent Legat	UCLouvain
	Jonathan Lambrechts	UCLouvain
Jury	Frédéric Dubois	CNRS-LMGC/UM
	Nicolas Moës	UCLouvain
	Miguel Cabrera	TUDelft
	Olivier Bruls	ULiège
	Stéphane Dorbolo	ULiège
Chairperson	Paul Fisette	UCLouvain

Louvain-la-Neuve, 9th September 2025

Abstract

Immersed granular flows, which are mixtures of solid particles and interstitial fluid, are found in a wide range of natural and industrial processes, including landslides and sediment transport and fluidised beds. Modelling them is particularly challenging due to the complex interplay between solid contacts, fluid dynamics, and evolving interfaces.

Numerical simulation is a powerful way of exploring such systems, providing detailed, time-resolved insights that are often difficult or impossible to capture experimentally. It enables key physical mechanisms to be isolated, hypotheses to be tested, and extreme conditions to be examined, making it a valuable complement to theoretical analysis and experimental work.

This thesis focuses on the modelling of immersed granular flows across multiple regimes and scales. It begins with the challenge of simulating grains comparable in size to fluid discretisation within the Volume-Averaged Navier–Stokes (VANS) framework using an overlap-wise grain representation and semi-implicit time integration. These extensions enable simulation from coarse to fine discretisation and restore the flexibility of the Finite Element Method for handling complex geometries without mesh size restrictions.

The model is extended further to include heat transfer, for which a new correlation is proposed for forced convection in granular suspensions. Spontaneous digging by a water droplet in a hot granular bed is investigated to reveal the main physical mechanisms involved. The model successfully reproduces the key phases of the digging process observed in experiments.

Finally, the Particle Finite Element Method (PFEM) is employed to model immersed granular flows with free surfaces that are subject large deformations. This Lagrangian formulation enables domain motion and interface tracking to be handled robustly. The historical Lituya Bay landslide and tsunami are simulated to demonstrate the model's capabilities and fidelity to real-world phenomena. Overall, the framework provides a versatile tool for exploring complex, multiphase granular phenomena.

Remerciements

Nous y sommes : au début de ce manuscrit qui marque la fin de ce parcours de thèse. Cette étape de vie n'aurait pas été possible sans le soutien de nombreuses personnes, que je souhaite remercier ici.

Je pense avant tout à ma famille, pour leur soutien inconditionnel, leur écoute face à mes doutes et leurs encouragements constants. Malgré nos chemins uniques, j'ai eu la chance d'avoir toujours eu des proches sur qui compter.

Une thèse est une expérience formatrice, et j'ai pu bénéficier de la pédagogie et de la bienveillance de mes deux promoteurs, Jonathan et Vincent. Je leur suis profondément reconnaissant pour leurs conseils avisés et leur accompagnement. De la recherche d'une question scientifique à la rédaction des articles, en passant par l'implémentation du code, j'ai appris énormément à chaque étape et si je ressors grandi de ces années, c'est en grande partie grâce à eux.

J'ai également eu le privilège d'évoluer dans un pôle de recherche dynamique, où régnaient convivialité, entraide et esprit de collaboration. Merci à mes collègues, devenus des amis, pour leur soutien, leur humour et tous ces moments partagés, que ce soit à la cafétéria, dans le A.012 ou le A.016 : Ange, Insaf, Chiheb, Nathan, Mattéo, Mohammed, Antoine, Thomas, Guillaume & Guillaume, Alexandre, Anthony, Simon, Miguel, Illy, Florian, Gatien, Nathan et Yana. J'espère n'avoir oublié personne... Je n'oublierai jamais nos moments d'humour avec Simon et Antoine, nos casques sur la tête, les discussions et débats animés avec Ange ou Nathan(s) suivis de soirées inattendues avec Mattéo, les bons moments et fructueuses collaborations avec Thomas, la découverte de la géométrie différentielle avec Miguel, ces interminables combats de regard avec Gatien en nous délectant des pâtisseries de Yana. Bref, tous ces beaux moments font de MEMA un pôle si particulier à mes yeux. Je n'oublie évidemment pas non plus tous les collègues et amis du bâtiment, comme Clémence, Seb, Philémon, Julien, Rémy ou Yassine. Les agréables discussions autour d'un café ou nos matchs de foot ont toujours été un plaisir. Tous ces souvenirs resteront gravés.

Je n'oublie pas mes amis musiciens et mes amis d'études, qui m'ont accompagné dans d'autres dimensions de ma vie et contribué à façonner la personne que je suis aujourd'hui.

Enfin, pour citer Dee Dee Ramone: *"I'd like to congratulate myself and thank myself and give myself a big pat on the back."* Je l'ai fait, et je suis fier du travail accompli.

Contents

CHAPTER 1

Introduction

> Every word is like an unnecessary stain on silence and nothingness.
>
> Samuel Beckett.

From the sandcastles we build as children to the concrete that forms our homes, and from the cells in our blood that are pumped around our bodies by our hearts to the asteroids that delivered minerals to Earth, granular materials are all around us, often going unnoticed. They are ubiquitous in nature, industry, the human body, and everyday life. Their range is remarkable, spanning everything from the grains of sugar in a cup of coffee to metre-sized boulders in landslides and kilometre-scale asteroids in space. This diversity of size, shape and composition gives rise to a wide variety of behaviours, ranging from flowing like a fluid in submarine avalanches to behaving like a solid in a stable sand pile. This unique combination of these properties makes granular materials a fascinating subject of study, with applications in various fields such as geophysics, civil engineering, and materials science. From viruses [1], nanoparticles [2] or colloids [3] at a few nanometres, to the motion of microplactics in the atmosphere [4] or red blood cells in our veins [5] at the microscale, to the motion of sand [6], or the flows of debris and boulders [7] to a few metres, from icebergs [8] to the asteroids [9] up to kilometres, the length scales span widely, as well as the range of applications. Figure 1.1 illustrates these examples based

on the characteristic temporal – length scale.

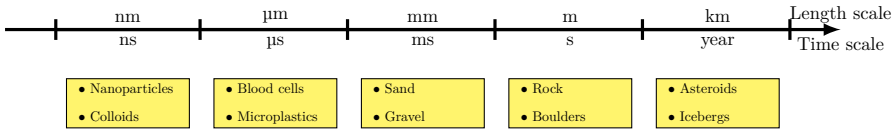

Figure 1.1: Characteristic scale of granular flows: some applications.

Due to the wide range of interactions grains can have, it is useful to classify granular flows based on the dominant ones [10]. For particles smaller than a micrometre, thermal agitation from the surrounding medium becomes significant, and Brownian motion dominates their dynamics. As particle size increases to the order of tens to hundreds of micrometres, colloidal forces – such as electrostatic interactions and van der Waals attractions – become the primary mechanisms governing particle behaviour. As the thermal agitation becomes negligible, such a system is said to be non-Brownian. For particles larger than approximately 100 micrometres, direct contact interactions and hydrodynamic forces drive the system. As particle motion induces displacement of the interstitial fluid, the rheology and dynamics of the mixture are highly coupled with the grains dynamics. This regime is the focus of this thesis, in particular the immersed case where the flow is incompressible and the particles are fully submerged. Such a flow is reffered to as an immersed granular flow or a non-Brownian granular suspension [11].

In view of the complexity of the interactions between grains and the fluid, numerical modelling is a powerful tool to study granular flows [12, 13]. Indeed, experimental studies are often limited to observable quantities and cannot provide detailed information about the internal structure of the flow. Numerical simulation, on the other hand, allows for a detailed analysis of the flow field, particle interactions, and the evolution of the system over time. The accuracy of a simulation depends directly on the quality of the model and its ability to capture the relevant physical phenomena. It is always worth keeping in mind that modelling is a simplification of reality, and the choice of model should be guided by the specific problem at hand.

Providing a comprehensive overview of the physics of granular flows is a daunting task, given the vast range of phenomena and applications involved. In this chapter, we will focus on the fundamental principles and challenges associated with modelling granular flows, particularly in the context of immersed conditions. We will begin by discussing the unique behaviour of granular materials, highlighting their solid-like, liquid-like, and gas-like states. Some of the most important phenomena associated with granular flows, such as jamming and segregation, will be introduced. Then, an overview of the main numerical methods used to model granular flows will be presented. From grain modelling to the fluid dynamics, we will discuss the various approaches used to simu-

late immersed granular flows. Finally, the main objectives of this thesis will be outlined, with a focus on the development of a new numerical method for simulating immersed granular flows.

Contents

Dense granular flows are ubiquitous in both natural and industrial settings, comprising the movement of large collections of discrete solid particles such as sand, gravel, grains, or powders. In industry, granular materials are integral to processes in pharmaceuticals, agriculture, mining, and construction, where efficient handling, transport, and processing of bulk solids are essential for productivity and safety. Granular flows also play a critical role in geophysical phenomena, including landslides, debris flows, avalanches, and volcanic pyroclastic flows, where understanding flow behaviour is vital for hazard prediction and risk mitigation. Despite their prevalence, granular flows are challenging to model due to their inherently discrete, nonlinear, and often non-continuum nature. Their dynamics are governed by complex inter-particle interactions, friction, and energy dissipation, which vary widely depending on particle properties and flow conditions. As such, accurately simulating granular flows is a central concern across disciplines, from designing industrial equipment to predicting large-scale natural disasters. The goal of this section is to provide a comprehensive overview of the fundamental principles and challenges associated with modelling granular flows, particularly in the context of immersed conditions.

1.1 Granular Media: Between Solid and Fluid Phases

Despite being composed of discrete solid particles, granular materials can exhibit behaviour that mimics the classical states of matter: solid, liquid, and gas. Several factors influence the state of a granular system, including particle interactions such as friction and collisions, external forces, packing density, and energy input.

Solid-like Regime – In densely packed configurations under low stress or low deformation, granular materials behave like a solid. They resist shear and maintain a fixed shape, often forming stable structures such as piles. This regime is crucial in geotechnical applications, such as the stability analysis of retaining walls or embankment design in civil engineering.

Liquid-like Regime – Once the shear stress exceeds a certain threshold, granular materials can flow like a liquid. Each layer of particles can slide over the others, resembling the dynamics of a viscous fluid. Such a behaviour is observed during the discharge of a silo and in the avalanches of granular materials.

Gas-like Regime – At high shear rates or low packing fractions, granular materials can behave like gas. The contact forces are weak and the particles are highly mobile, leading to rapid, random collisions similar to gas molecules. This regime is observed in fluidised beds, where particles

are suspended in a gas or liquid, allowing for enhanced mixing and heat transfer.

As these conditions may change within a system, the three states are not mutually exclusive and can coexist or transition into one another. Figure 1.2 illustrates one such application, an hourglass, where the three states can be observed. In the upper part of the hourglass, the grains are in a solid-like state and their motion is limited by friction. In the central part, the grains are in a liquid-like state and are able to flow, which leads to the discharge of the grains. Once discharged, they fall freely, leading to a gas-like state. Finally, the grains are stopped by the ground, returning to a solid-like state.

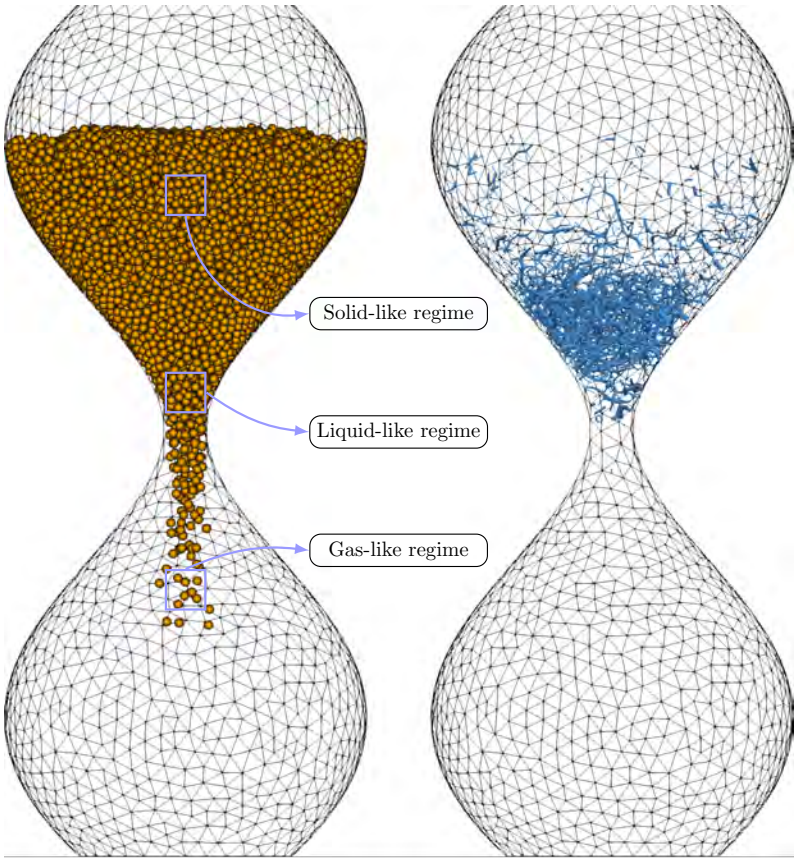

Figure 1.2: Granular materials can exhibit solid-like, liquid-like, and gas-like as observed in an hourglass. On the left, the grains are shown. On the right, the contact network is highlighted.

In order to understand the complex behaviour of granular materials, it is essential to consider the network formed by the particle–particle interaction forces. When a dense granular system is compressed or sheared, the particles in contact with the external load will transmit it to their direct neighbours. In return, these neighbours will pass the load on their neighbours, and so on. This creates a network of force chains that can transmit stress throughout the system. It is important to note that these force chains are not static structures, but rather dynamic networks that can change in response to external forces and rearrangements of the particles. The contact network can be heterogenous, with some regions experiencing high stress and others low stress. This change can occur instantaneously and locally. This complex behaviour gives rise to the emergence of phenomena not present in idealised states of matter, such as jamming and segregation.

Jamming – Jamming characterizes the transition from a flowing state to a solid-like state. The jamming transition occurs when the packing fraction and applied stress exceed critical thresholds, resulting in the formation of a rigid contact network that resists further deformation [14, 15]. Figure 1.3 illustrates jamming in a silo with monodisperse grains. At the particle level, jamming occurs when particles can no longer rearrange due to the formation of force chains and frictional contacts [16]. This phenomenon is not exclusive to dry granular materials; it also arises in immersed granular flows [11, 17, 18]. For frictionless spheres, this critical packing fraction is typically around 0.64, known as the random close packing limit. Understanding the jamming transition is crucial for predicting the behaviour of granular materials in various applications, ranging from silo discharge to the stability of boulder assemblies. Recently, the jamming transition has been studied using pressure-imposed rheometers [19], which allow the macroscopic properties of the system to be measured close to its jamming packing fraction [20, 21].

Segregation– Granular segregation is a phenomenon that occurs when particles of different sizes, shapes, or densities separate from each other during flow or mixing. A well-known example of this is the Brazil nut effect, whereby larger particles rise to the surface of a shaken granular mixture. This behaviour is commonly observed in the food industry, where it can be exploited to separate grains or seeds based on their physical properties. Although segregation can be useful for sorting particles, it can present challenges in industrial processes that require uniform mixing. For example, consistent blending of active ingredients and excipients is critical for product quality in pharmaceutical manufacturing. To illustrate the effects of segregation, consider the mixing process in a V-blender, as shown in Figure 1.4. Two dry powders with different particle sizes are introduced from either side of the blender. As the blender rotates about

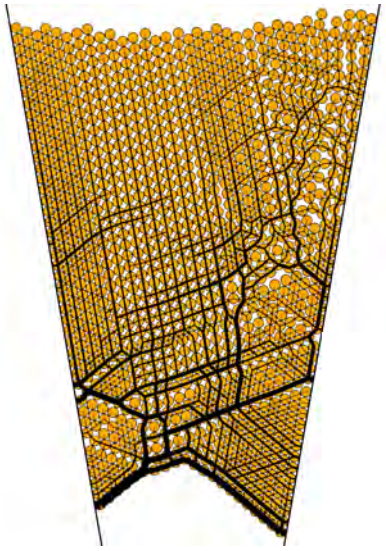

Figure 1.3: Jammed granular flow in a silo, formed by the contact arch network between the grains.

the horizontal axis, the powders repeatedly split and recombine, which promotes mixing. However, due to differences in particle size, complete homogenisation is not achieved. Instead, segregation persists, resulting in a non-uniform mixture.

1.2 Hydrodynamic Effects on Granular flows

Granular flows can occur in a range of fluid environments, from completely dry to fully immersed, with partially saturated states lying in between. The presence and nature of the interstitial fluid can dramatically alter the mechanical behaviour of granular materials, influencing particle interactions, rheology, and flow regimes.

Dry – In dry granular flows, the absence of an interstitial fluid means that particle dynamics are almost entirely governed by contact interactions, including friction, inelastic collisions, and geometric constraints. Depending on particle shape, packing fraction, and external forcing, these systems often exhibit complex behaviour such as jamming, dilatancy, or shear banding.

Partially Saturated – Between the two extremes, dry and immersed, lie partially saturated granular systems, where small amounts of liquid are

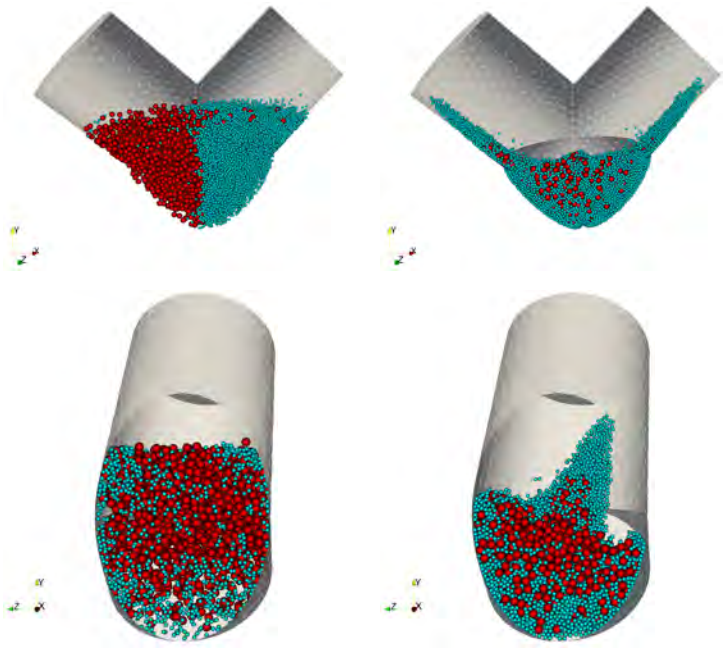

Figure 1.4: Mixing of bidisperse powders in a V-blender rotating about the x-axis. Top: front view; bottom: lateral view. Left: initial configuration of the powders; right: state after 40s of mixing.

present within the pore space but do not fully submerge the grains. These systems are of particular interest because they combine solid-solid contact mechanics with capillary and void interactions, resulting in highly nonlinear and history-dependent behaviours. A common way to characterise the state of a partially saturated granular system is to define a saturation level, S, as the ratio of the volume of liquid to the volume of voids in the system,

$$S = \frac{V_l}{V_v} = \frac{V_l}{V_T - V_s} \tag{1.1}$$

where V_l is the volume of liquid, V_v is the volume of voids, V_T is the total volume of the system, and V_s is the volume of solid particles. The impact of the interstitial fluid can be modelled as a cohesive force acting on the particles. Figure 1.5 illustrates the different saturation levels, the associated cohesion and their corresponding flow regimes.

Pendular State – At low saturation levels $S \leq 0.25$, the system enters

the pendular state, where discrete capillary bridges form between particles at contact points. These bridges generate cohesive forces due to surface tension, increasing the yield stress and apparent viscosity of the material. Such systems behave similarly to weakly cohesive powders and are sensitive to particle size, surface properties, and liquid characteristics.

Funicular State – As the liquid content increases $0.25 < S < 0.9$, individual bridges begin to coalesce, marking the transition to the funicular state. In this regime, some pores remain filled with air, while others become saturated with liquid. The coexistence of air-liquid interfaces and larger fluid clusters introduces both capillary and hydrodynamic forces, resulting in a highly sensitive mechanical response to saturation, shear rate, and fluid rheology.

Capillary State – At even higher saturations $S \geq 0.9$, the system may approach the capillary state, where most pores are filled, and capillary suction plays a reduced role. Eventually, the system becomes fully saturated, and behaves like immersed granular materials.

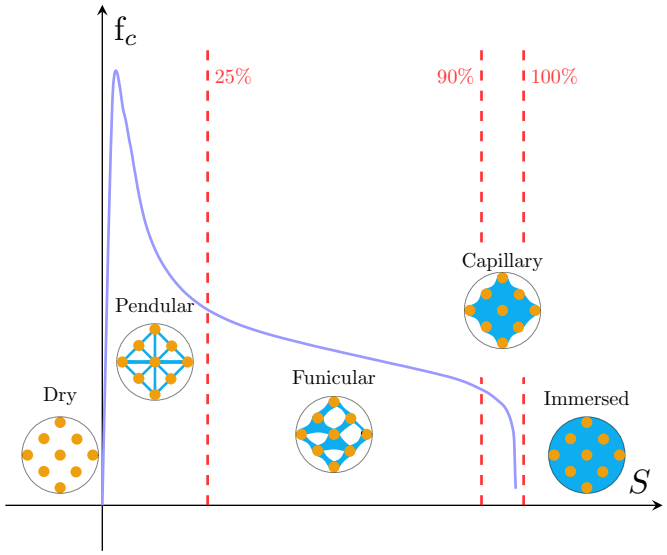

Figure 1.5: Immersed granular flows: the influence of the interstitial fluid on the flow regime.

Immersed – In immersed systems, grains are fully submerged in a fluid, and hydrodynamic interactions play a dominant role in the system's be-

haviour. These interactions include drag, lubrication, added mass, and Basset history forces, all of which arise from the fluid's viscosity and inertia. The balance between viscous and inertial forces, often characterized by the Stokes number, determines whether the flow is in the viscous or inertial regime. In the viscous regime, fluid-particle coupling damps motion, while in the inertial regime, grain inertia dominates. The properties of the interstitial fluid, such as its density and viscosity, can either suppress or enhance granular flow dynamics. Due to the fluid's viscosity, the fluid–grain interface is subject to the no-slip condition, meaning the fluid velocity at the particle's surface matches that of the particle itself. This condition leads to the formation of a boundary layer of fluid that is carried along with the particle. The force exerted by the fluid on the particle is expressed as:

$$\mathbf{F} = \int_S \boldsymbol{\sigma} \cdot \boldsymbol{n} \, \mathrm{d}s = \int_S (-p\boldsymbol{n} + \boldsymbol{\tau} \cdot \boldsymbol{n}) \, \mathrm{d}s \tag{1.2}$$

where $\boldsymbol{\sigma}$ is the stress tensor, S is the surface of the particle, $\boldsymbol{n}$ is the normal vector to the surface, p is the pressure, and $\boldsymbol{\tau}$ is the viscous stress tensor. The first term represents the pressure force acting on the particle, while the second term accounts for the viscous shear stress acting on its surface. There is no general analytical expression for this force, as it depends strongly on both the flow regime and the shape of the particle. However, various approximations exist for idealised cases. In many practical contexts, the total force is estimated by summing the contributions from several idealized force components. Below, we review the most common hydrodynamic forces acting on a particle in a fluid:

Drag force – The drag force is the resistive force experienced by a particle moving through a fluid [22]. It acts in the opposite direction to the particle's motion and is aligned with the flow. Figure 1.6a illustrates the drag force acting on a particle in a potential flow. Analytical solutions exist for spherical particles in creeping flow, and constitutive models have been developed to extend these to higher Reynolds numbers [23], as well as to dense suspensions [24].

Buoyancy force – The buoyancy force is the upward force exerted by the fluid on a submerged particle, counteracting gravity. It equals the weight of the displaced fluid and acts in the opposite direction to the gravitational force. Figure 1.6b illustrates this force. Buoyancy plays a key role in processes involving submerged or floating particles, such as sedimentation and underwater transport [25].

Magnus force – The Magnus force arises when a rotating particle moves through a fluid [26, 27]. The rotation induces a difference in fluid

velocity on either side of the particle, leading to a pressure differential and resulting in a force perpendicular to the direction of motion. As a lift force, it acts orthogonally to the main flow. Figure 1.6c shows the Magnus force acting on a spinning particle. This effect is particularly relevant to the motion of spinning objects, such as sports balls or rotating spheres in fluid environments.

Saffman force – The Saffman force is a lift force caused by velocity gradients, by a shear, in the fluid around a particle [28, 29]. Velocity asymmetry leads to a pressure difference across the particle, resulting in a net force acting on it. This force acts perpendicular to the direction of motion. It can drive particle migration in a shear flow, causing particles to move towards regions of higher velocity. Figure 1.6d depicts the Saffman force acting on a particle in Poiseuille flow.

Added mass force – When a particle accelerates in a fluid, it must also accelerate some of the surrounding fluid. This results in an additional inertial resistance called the added mass force [30, 31]. This force is proportional to the particle's acceleration and is especially important in dense or unsteady flows. The added mass effect also arises in inviscid flows, even when the particle velocity is constant, due to the inertia of the displaced fluid.

Basset force – The Basset force, like the added mass force, originates from the particle's acceleration, but it is due to viscous effects and has a memory component [32, 33]. It depends on the history of the particle's motion and is proportional to the time derivative of its velocity. This force is particularly relevant in low Reynolds number flows where viscous effects dominate.

As the number of grains in a suspension increases, its macroscopic behaviour is governed by both fluid dynamics and inter-particle interactions. Depending on the suspension's physical properties and the imposed flow conditions, the particles can exhibit a wide range of collective behaviours [17]. To classify these regimes, researchers often rely on dimensionless parameters such as the Stokes number and the density ratio. The Stokes number (St) quantifies the relative importance of inertial forces compared to viscous forces acting on a particle in a fluid and is defined as:

$$\mathrm{St} = \frac{\rho_g \dot{\gamma} d^2}{\eta} \tag{1.3}$$

where ρ_g is the particle density, $\dot{\gamma}$ is the shear rate, d is the particle diameter, and η is the dynamic viscosity of the fluid. When the Stokes number is small, $\mathrm{St} \ll 1$, viscous forces dominate and the system operates in the viscous regime. In contrast, at high Stokes numbers, $\mathrm{St} \gg 1$, where

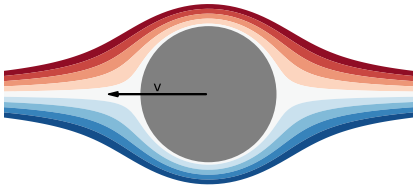

(a) Drag force. The coloured field indicated isovalues of the stream function generated by a particle moving in a fluid.

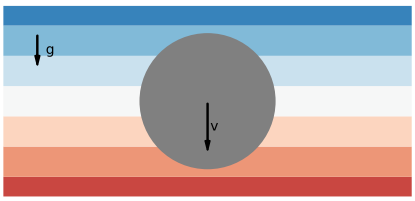

(b) Buoyancy force. The coloured field shows isovalues of an hydrostatic pressure field.

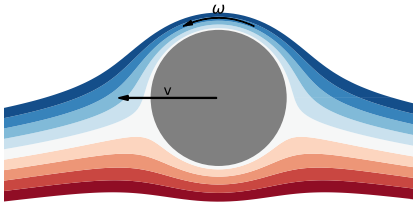

(c) Magnus force. Isovalues of the stream function generated by a rotating particle in a fluid are indicated with the continuous field.

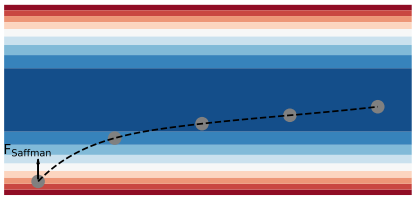

(d) Saffman force. Isovalues of the Poiseuille velocity profile are plotted. The particle is moving towards the high velocity region. The particle trajectory is indicated by the dash line.

Figure 1.6: Hydrodynamic forces acting on a particle in a fluid.

inertial effects become significant, the system enters the inertial regime. If, in addition, the particle density is much higher than the fluid density, the behaviour closely resembles that of a dry granular flow.

As the fluid alters the dynamics of the particles, the particles in turn influence the macroscopic properties of the fluid. The presence of particles distorts the streamlines, leading to an increase in the effective viscosity of the suspension. For buoyant particles with a packing fraction of less than 0.1, the effective viscosity follows a quadratic dependence on the packing fraction according to [34]:

$$\eta_{\text{eff}} = \eta \left(1 + 2.5\phi + 7.6\phi^2\right). \tag{1.4}$$

At higher packing fractions, the effective viscosity increases sharply and approaches a divergence as the system nears the jamming transition. The Krieger–Dougherty model [35] is often used to describe this behaviour:

$$\eta_{\text{eff}} = \eta \left(1 - \frac{\phi}{\phi_c}\right)^{-\alpha} \tag{1.5}$$

where ϕ_c is the critical packing fraction and α is a fitting exponent, these two parameters depend on the shape and size distribution of the particles.

This nonlinear behaviour highlights the complex interplay between the fluid and the particles. The effective viscosity is not only a function of fluid properties but also of particle characteristics and their interactions. Consequently, a suspension may behave like a Newtonian fluid in dilute, fluidized regions and like a highly viscous or even jammed medium in denser regions.

Developing a unified model that resolves the flow of individual particles at a microscopic level and their collective motion is computationally expensive and often relies on approximations or constitutive laws. The key challenge lies in selecting a model that captures the essential physics of the system while remaining computationally feasible. In the case of immersed granular flows relevant to the present applications, it is the drag force and the pressure gradient that dominate the particle dynamics. Consequently, modelling will focus on these forces while disregarding the others.

1.3 Granular Flows: A modelling Perspective

The variety of application domains and the complexity of the interactions between the grains and fluids have given rise to a wide range of modelling approaches. The choice of a model depends on the specific problem being addressed, the desired level of detail, and the available computational resources. In this section, we will review the main modelling approaches used to study immersed granular flows. For the sake of clarity, we will distinguish between models that describe the grains and models that describe the fluid.

1.3.1 Grains modelling

One of the main challenges in modelling immersed granular flows lies in accurately representing the particles, which may vary significantly in size, shape, and material properties. From the macroscopic continuum scale to the microscopic contact scale, we review below the most common modelling approaches used to describe such particles. An extensive review can be found in [13].

2-Fluid Model – The two-fluid model adopts a continuum perspective in which the granular material is treated as a continuous phase and effectively smoothing out its discrete nature. Constitutive laws are introduced to relate the macroscopic stress tensor to local variables such as the packing fraction and the velocity field. This approach is computationally efficient and can capture the bulk behaviour of the system. However, it may fail to represent important microscale phenomena, such as individual particle interactions and localised heterogeneities.

Discrete Element Method (DEM) – The DEM is a particle-based numerical method that simulates the motion and interaction of individual particles [36]. Each particle is treated as a discrete entity whose dynamics are governed by the Newton-Euler equations. Interactions between particles are modelled through contact forces, hydrodynamic forces, and external loading. The DEM is particularly well-suited to granular flows, as it directly captures the discrete nature and detailed dynamics of particle interactions. To compute the forces acting on each particle, the method typically employs a *soft-sphere* approach, whereby particles are permitted to overlap slightly during contact [37]. This overlap is resolved using a spring-dashpot model that combines elastic and damping components in both the normal and tangential directions. Key parameters include normal and tangential stiffness coefficients, damping factors, and a friction coefficient. The method is explicit: contact forces are computed based on the overlap and relative velocities at the start of the time step. Consequently, the time step must be sufficiently small to maintain numerical stability and accuracy, particularly in dense or highly dynamic systems.

Non-Smooth Contact Dynamics (NSCD) – The Non-Smooth contact dynamics method is a variant of the DEM [38]. Unlike the soft-sphere approach, overlapping particles is prohibited, hence its name the *hard-sphere* approach. Contact forces and velocities are determined by solving a complementarity problem, which enforces non-overlapping constraints and friction laws [39, 40]. This method does not rely on artificial force-penalty parameters and treats contacts as instantaneous within each time step. An iterative solver is required to solve the contact network, which can lead to a non-unique solution that may change abruptly. NSCD is implicit in nature and allows for larger time steps than traditional soft-sphere DEM.

Meshed Particles – In scenarios where the shape of the particles plays a critical role, a meshed representation can be employed [41]. Particles are modelled as deformable solids using finite element methods, which enable the detailed resolution of particle shape and internal stress fields. While this approach provides high-fidelity contact modelling based on solid mechanics, it is computationally intensive and requires fine meshing to maintain accuracy.

1.3.2 Resolved Fluid Description

To capture the fluid dynamics around particles, various modelling approaches have been developed. If the spatial discretisation of the fluid is fine enough to resolve the flow around the particles, the fluid can be described using a resolved approach. This approach becomes computationally expensive for a large

number of particles. The two main families of spatial discretisation method commonly used to describe the fluid are mesh-based and meshless methods.

Mesh-Based Methods

Mesh-based methods rely on a discretisation of the domain using a mesh or grid. The mesh can either be conformal or non-conformal to the shape of the particles. Conformal meshes are typically used in finite element methods (FEM), where the mesh adapts to the particles' geometry. To account for moving particles, the mesh can be distorted using an Arbitrary Lagrangian-Eulerian (ALE) approach [42] or using the Particle Finite Element Method [43] where the mesh nodes are advected with the fluid velocity. Non-conformal meshes on the other hand do not capture the particle boundary but will modify the discretised conservation equations to account for the particles' presence. Two of these common methods are the immersed boundary method (IBM) and the cut finite element method (CUT–FEM). The IBM uses a fixed mesh and introduces a force term in the Navier-Stokes equations to account for the presence of the particles [44]. In the CUT–FEM, the discretised variational formulation is modified in order to maintain the same level of accuracy and convergence as the classical FEM [45]. Figure 1.7a and 1.7b illustrate the difference between conformal and non-conformal meshes.

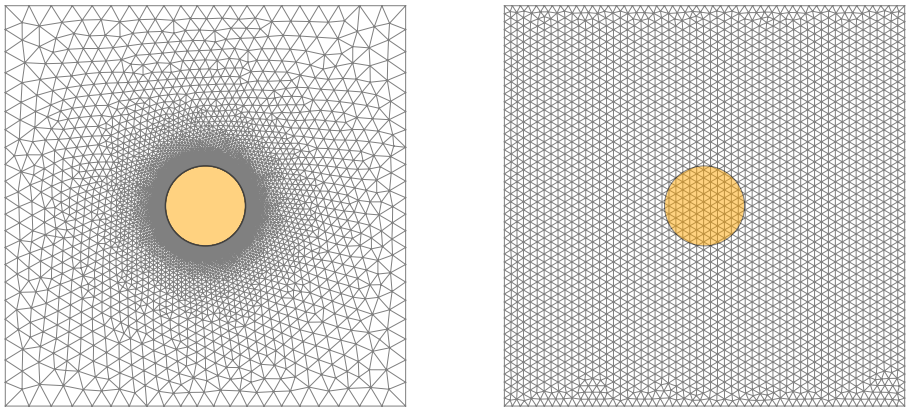

(a) Conformal mesh.

(b) Non-conformal mesh.

Figure 1.7: On the left, the mesh is conform to the particle geometry. On the right, the mesh is independent of the particle geometry.

Meshless Methods

Unlike mesh-based methods, meshless methods do not rely on a fixed mesh and can adapt to the motion of the grains. They are particularly useful for simulating large deformations or complex geometries. The two most common meshless methods are Smoothed Particle Hydrodynamics (SPH) and the Lattice Boltzmann Method (LBM). In the SPH method, the fluid is represented as a collection of particles, each of which carries properties such as mass, velocity, and density [46]. Fluid properties are computed using a kernel function that interpolates the properties of neighbouring particles. In contrast, the LBM is a lattice-based method that simulates fluid flow by tracking the evolution of particle distribution functions on a lattice grid [47]. It solves the Boltzmann equation instead of the Navier-Stokes equations. Figure 1.8a and 1.8b illustrate SPH and LBM methods. One of the main advantages of meshless methods is their ability to handle complex geometries and large deformations without the need for remeshing. However, imposing boundary conditions can be a more challenging task compared to mesh-based methods.

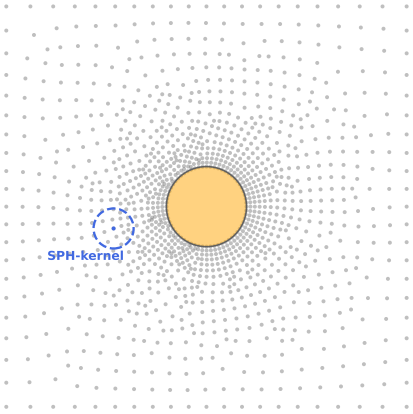

(a) Smooth Particle Hydrodynamics discretisation.

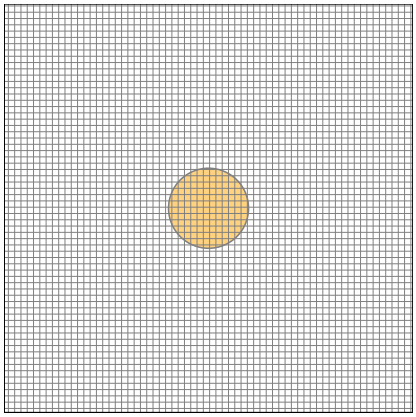

(b) Lattice Boltzmann discretisation.

1.3.3 Unresolved Fluid Approach

In many applications, the number of particles and their interactions can be so complex that resolving the fluid around each particle becomes computationally prohibitive. In such cases, a non-conformal unresolved approach is often used where the fluid discretisation is much larger than the particle size. The fluid-grain interaction force is simplified into a body force that can be added to the particle dynamics and to the fluid dynamics. This approach is particularly useful for large-scale simulations, in which the focus is on the macroscopic

behaviour of the system rather than on the detailed interactions between individual particles. The unresolved approach typically assumes the particles to be spherical and small compared to the fluid domain. The Volume-Averaged Navier-Stokes equations (VANS) can be used to describe the fluid dynamics [48]. These equations are derived from the Navier-Stokes equations by averaging the fluid properties over a control volume that includes both the fluid and the particles. To account for the presence of particles, either a continuous representation of the particles is used leading to the so-called 2-fluid model [11] or a discrete representation of the particles leading to the hybrid class of CFD-DEM models [49, 50, 51]. At the edge of the unresolved approach lies the semi-resolved one where the mesh size is comparable to the particle size [52, 53]. Such an approach balances the computational cost with a better representation of the flow.

Figure 1.9: 2-Fluid solid velocity representation.

Figure 1.10: Unresolved CFD-DEM solid velocity representation.

1.4 Thesis objectives – My PhD journey

As research invariably builds upon prior work, so does this thesis. It was conducted within the research group developing MigFlow in UCLouvain, which started as a collaboration with the LMGC lab in Montpellier. Two previous theses have been completed in this context, focusing on developing a numerical model for immersed granular flows. The first thesis, by Constant [54], focused on the development of a numerical model for immersed granular flows using an unresolved approach combined with the Discrete Element Method (DEM) and Non-Smooth Contact Dynamics (NSCD) to model grain dynamics [55]. The model was then validated against air injection fluidisation experiments [56] and density sorting experiments [57]. The second thesis, by Coppin [58], focused on the numerical analysis of drag forces in immersed granular flows [59] and the modelling of granular collapse events [60]. Frictional collisions and disc clustering were developed in this context. In both theses, the fluid phase is described using the Volume-Averaged Navier–Stokes equations, discretised with a first-order velocity–pressure scheme. Stabilisation techniques, such as Streamline Upwind Petrov-Galerkin (SUPG) and Pressure-Stabilizing Petrov-Galerkin (PSPG), are employed to ensure numerical stability and convergence, due to the use of equal-order interpolation shape function and to address convective terms. Coupling between the fluid and granular phases is achieved via a force term and the fluid volume fraction (i.e. porosity). The grain representation is point-based, and all fluid–grain interaction forces are computed at the particle center using drag force constitutive laws.

The objective of my thesis is first to extend the numerical model to the **semi-resolved** scale, where the mesh size is comparable to the particle size. This extension is crucial for simulating polydisperse flows, where particles of different sizes coexist. Secondly, the digging of a water droplet into a hot granular bed is investigated, leading to the modelling of **heat transfer**. Finally, I study immersed granular flows with **free surfaces**, which have applications in landslides and granular collapse events.

1.4.1 A semi-resolved model

My first objective is to extend the current numerical model to support mesh sizes on the order of the particle diameter, a regime commonly referred to as *semi-resolved*. Previous studies have suggested using a Gaussian filtering kernel instead of the current kernel based on the finite element shape functions. However, fully resolved approaches such as Cut-FEM or the Volume Penalisation Method do not require such kernels and can operate at fine resolutions without compromising stability. My aim is to develop a fluid–solid coupling strategy that remains stable under mesh refinement and does not rely on additional smoothing kernels. Unresolved approaches often suffer from numerical insta-

bilities, which are typically mitigated through artificial diffusion [49]. Recent work by Blaise et al. [53] has demonstrated that a continuous representation of particles, in both space and time, can provide inherent numerical stability without requiring such diffusion. Building on this idea, I will investigate time integration schemes that preserve stability, eliminating the need for artificial numerical diffusion. One of the main challenges is keeping the computational cost low while ensuring the accuracy of the results. Moreover, all previous numerical experiments must be repeated to validate the coupling. As a benchmark, we will simulate the granular Rayleigh-Taylor instability which occurs when particles that are heavier than the fluid below them are released. This leads to the formation of fingers that, unlike in the classical Rayleigh–Taylor instability, increase in width and cause fluid bubbles to rise. Figure 1.11 illustrates this behaviour.

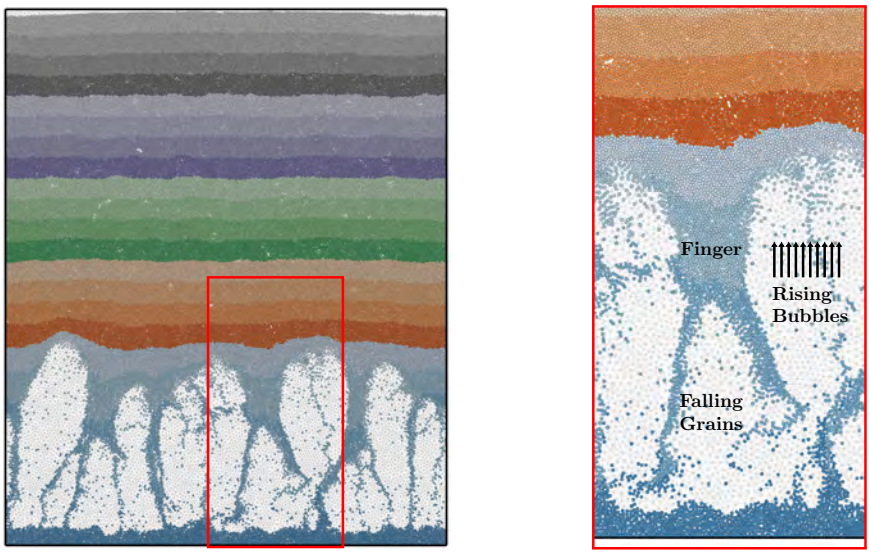

Figure 1.11: Granular Rayleigh-Taylor instability.

1.4.2 Water droplet digging

My second objective is to incorporate heat transfer into the numerical model to simulate the intrusion of a water droplet into a hot granular bed. In many industrial applications, such as fluidized bubbling bed boilers, granular materials are used as thermal energy storage media. When required, heat is released through fluidisation. This process is usually achieved by injecting a fluid into the granular bed, with the fluid acting as the heat carrier. A recent experimental study [61] have revealed a Leidenfrost-based digging mechanism, whereby a water droplet can penetrate a hot granular bed without instant evaporation. As the droplet digs into the bed, it cools the surrounding grains locally, providing an alternative approach to extract heat from the medium. The digging process stops either when vapour ejection is either too weak to displace particles or strong enough to completely lift the droplet. My aim is to reproduce this phenomenon numerically and to investigate the underlying physical mechanisms. Figure 1.12 illustrates the intrusion of a droplet into a hot granular bed. To this end, I will extend the current numerical model to incorporate heat transfer. This extension will involve two main components. Firstly, I will implement heat conduction within the solid phase, to enable simulation of thermal diffusion through the dry granular bed. Secondly, I will incorporate volume-averaged heat transfer in the fluid phase, leveraging the previously developed semi-resolved model to simulate the droplet-induced digging process. Similarly to the drag force, a constitutive law to model forced convection between particles and fluid should be introduced. To track the droplet motion, the Arbitrary Lagrangian-Eulerian (ALE) method will be employed.

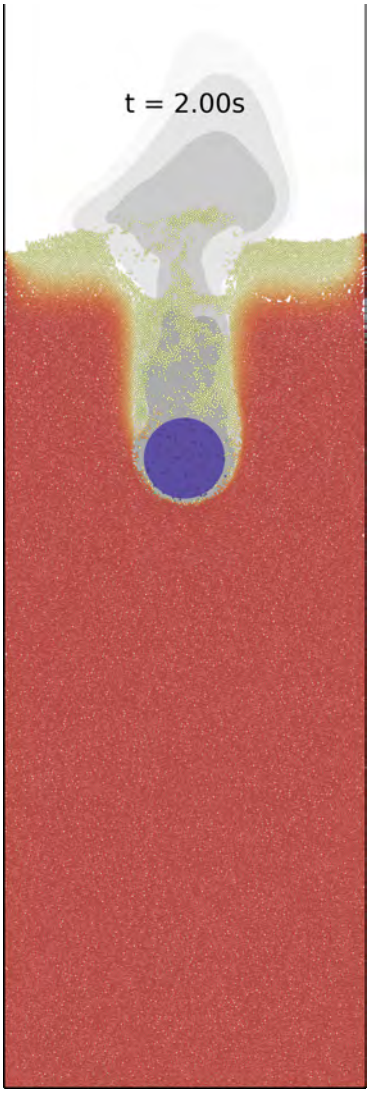

Figure 1.12: Digging of a droplet in a hot granular bed.

1.4.3 Landslides and free surface flows

My third objective is to extend the numerical model to simulate free-surface flows, with a particular focus on landslide dynamics. Landslides are complex natural phenomena that can be triggered by various factors, such as intense rainfall, seismic activity, or anthropogenic disturbances. They pose a significant risk to infrastructure and human life, so it is crucial to understand the mechanisms that drive their initiation and propagation in order to develop effective mitigation strategies. In this context, I will investigate the influence of the fluid phase on landslide dynamics, with particular attention to the historical event in Lituya Bay, Alaska. This event was triggered by a massive rockslide into the bay, caused by an earthquake, which displaced a large volume of water and generated a wave that reached a run-up height exceeding 524 metres. The Lituya Bay case serves as a compelling study for understanding the interaction between granular landslides and the generation of free-surface waves. Figure 1.13 illustrates the wave formation resulting from the landslide. To simulate such complex phenomena, I will couple the developed semi-resolved fluid–grain model with the Particle Finite Element Method (PFEM) [62]. While the implementation of PFEM itself will be carried out by my colleague Thomas Leyssens, my contribution will focus on coupling PFEM with the semi-resolved fluid–grain model. PFEM, a Lagrangian method, is particularly well suited for problems involving large domain deformations and topological changes, which are characteristic of wave formation in landslide events. However, PFEM is known to suffer from inherent volume loss, necessitating the use of mesh refinement techniques to mitigate those losses. Applying these techniques requires a careful balance between computational cost, accuracy, and the robustness of the fluid–grain coupling, particularly as the computational domain transitions from unresolved regions, far from the free surface, to semi-resolved regions near the fluid–granular interface. To validate the proposed coupling strategy, I will simulate the collapse of a granular column into a fluid basin and compare the results with experimental data [63]. Finally, I will apply the model to simulate the Lituya Bay event and compare the results with experimental reconstructions [64].

Supporting publications

- Leyssens, T., **Henry, M.**, Lambrechts, J., Legat, V., Remacle, J.-F., (2025),
  A Coupled PFEM-DEM Model for Fluid-Granular Flows with Free Surface Dynamics Applied to Landslides. Journal of Computational Physics. In this publication, the Lituya Bay tsunami, triggered by a landslide, is simulated using our novel coupled PFEM-DEM model. The two first authors contributed equally to this work. The PFEM model was devel-

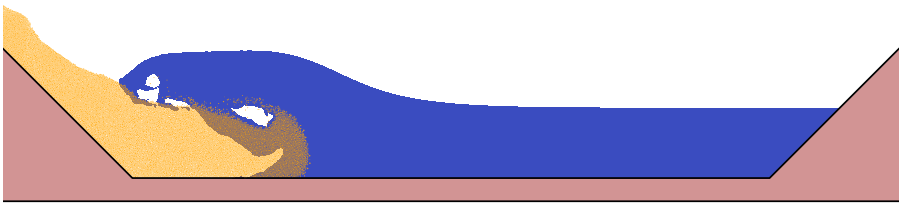

Figure 1.13: Lituya Bay wave generated by a landslide.

oped by Thomas Leyssens, while I was responsible for the coupling with the semi-resolved fluid–grain model and the numerical simulations. Both authors contributed to the numerical analysis and the physical interpretation of the results.

- **Henry, M.**, Coppin, N., Dorbolo, S., Legat, V., Lambrechts, J., (2025), *Multiscale FEM-DEM model for spontaneous droplet digging in a hot granular bed*. International Journal of Heat and Mass Transfer.
  This paper investigates the penetration of a water droplet into a hot granular bed. To this end, I extended the previous unresolved FEM-DEM model to a semi-resolved scale, enabling the representation of droplet–granular bed interactions. Heat transfer and vapourisation was incorporated into the model, allowing for the simulation of the droplet-induced digging process.

- Leyssens, T., **Henry, M.**, Lambrechts, J., Remacle J.-F., (2024),
  A Delaunay refinement algorithm for the particle finite element method applied to free surface flows. International Journal for Numerical Methods in Engineering.
  This publication presents a Delaunay refinement algorithm for the Particle Finite Element Method (PFEM). By refining the mesh near the free surface, the algorithm enhances the handling of topological changes and improves overall mesh quality. As a result, volume loss due to the filtering of elements by the α-shape criterion is significantly reduced. My contribution to this work involved supporting and developing the coupling between the mesh algorithms and our in-house fluid solver.

- Coppin, N., **Henry, M.**, Cabrera, M., Azéma, E., Dubois, F., Legat, V., Lambrechts, J., (2023).
  Collapse dynamics of two-dimensional dry and immersed granular columns of elongated grains . Physical Review Fluids.
  This paper investigates the collapse of granular columns composed of

elongated grains, under both dry and immersed conditions. To this end, the Discrete Element Method (DEM) was extended to handle clusters of discs, and the fluid–grain interaction forces were updated accordingly to account for the cluster geometry through the same disc decomposition. I contribute on the implementation of the cluster model.

Conferences talks

- **Henry, M.**, Coppin, N., Dorbolo, S., Lambrechts, J., Legat, V. (2025).
  FEM-DEM model of a water droplet digging in hot granular bed.
  COUPLED 2025, Villasimius, Italy.

- **Henry, M.**, Dorbolo, S., Dubois, F., Lambrechts, J., Legat, V. (2024).
  La modélisation du tranfert de chaleur dans les écoulements granulaires immergés par une approche multi-échelle.
  CSMA 2024, Presqu'île de Giens, France.

- **Henry, M.**, Dorbolo, S., Lambrechts, J., Legat, V. (2023).
  Unresolved FEM-DEM model for heated immersed granular flows.
  Particles 2023, Milano, Italy.

- **Henry, M.**, Dorbolo, S., Lambrechts, J., Legat, V. (2023).
  Unresolved FEM-DEM model for the penetration of a water droplet into hot granular materials.
  CFC 2023, Cannes, France.

- **Henry, M.**, Lambrechts, J., Legat, V. (2022)
  A multi-scale FEM-DEM model to exhibit viscoelastic properties of colloidal suspension.
  BGR2022, Leuven, Belgium.

- **Henry, M.**, Legat, V., Lambrechts, J. (2022)
  Multi-scale model for the study of the viscoelastic properties of a suspension.
  ACOMEN 2022, Liège, Belgique.

- **Henry, M.**, J. Fraiture, C. Jevens, Dubois, F., Legat, V., Lambrechts, J. (2022).
  Simulation du gonflement retardé au moyen d'un modèle multi-échelles d'une suspension en vue de l'étude des propriétés viscoélastiques.
  CSMA 2022, Presqu'île de Giens, France.

CHAPTER 2

Non-Smooth Dynamics in Granular Physics

> If you can't explain it simply, you don't understand it well enough.
>
> — Albert Einstein.

Granular materials consist of macroscopic particles that interact through contact forces, friction, and collisions. Unlike fluids or conventional solids, granular matter lacks a clear scale separation between microscopic interactions and macroscopic behaviour, making it difficult to describe with classical continuum mechanics [65, 66, 67]. In particular, defining consistent constitutive laws, that relate stress and strain in a predictive way, is challenging due to the discrete nature of the medium, history dependence, and strong heterogeneities in force transmission [68]. These limitations motivate the use of numerical approaches that resolve grain-scale interactions directly.

One such approach is the Discrete Element Method (DEM) originally developed by Cundall and Strack [36] for geomechanical problems. Particles are modeled as rigid bodies whose motion and contact interactions are governed by Newton-Euler's laws of motion. By treating grains as rigid bodies, DEM avoids the need to define bulk constitutive relationships, instead computing macroscopic responses as an emergent result of contact-level physics. Each grain's

position and orientation evolve according to forces arising from inter-particle contacts, gravity, and possibly fluid interactions. This particle-scale resolution provides a natural way to capture phenomena such as jamming, segregation, dilatancy, and energy dissipation. These features are difficult to encode in continuum models [69, 70, 71].

Traditional implementations of the Discrete Element Method (DEM) often rely on smooth contact laws, whereby small overlaps between particles are used to model elastic or viscoelastic behaviour [72]. This approach, known as the soft-sphere model, enables efficient explicit time integration, which is particularly well-suited for GPU-based parallelization [37]. While effective for loosely packed or weakly interacting granular systems, soft-sphere DEM can encounter stability and efficiency issues when applied to densely packed, stiff, or quasi-rigid materials. In these regimes, large numbers of simultaneous contacts and rapidly changing contact networks can lead to numerical instabilities and require prohibitively small time steps to maintain accuracy and robustness. To overcome these limitations, the Non-Smooth Contact Dynamics (NSCD) approach has been developed [73, 74, 75]. NSCD treats particles as perfectly rigid bodies and resolves contact interactions through complementarity conditions or variational inequalities, which enforce non-penetration and Coulomb friction constraints directly, without relying on artificial dissipation or elastic deformation. This framework is particularly advantageous for modelling dense granular flows, where persistent contacts, sudden transitions between sticking and sliding, and highly intermittent force chains are common. Unlike soft-sphere, NSCD is capable of resolving large contact networks and discontinuous motion in a stable and consistent manner, without requiring small time steps or the regularization of contact laws. This makes it especially suitable for applications such as quasi-static deformation, compaction, or impact-driven granular dynamics, where the accurate treatment of contact conditions is critical.

In real-world scenarios, granular flows often occur in the presence of an interstitial fluid, such as air or water. The interaction between the grains and the fluid can dramatically influence the flow behaviour due to added mass effects, buoyancy, drag, lubrication, and variations in pore pressure. The force applied by the fluid to each grain can be incorporated directly into the DEM framework through an external fluid-grain interaction force. This external force can be explicitly integrated into the NSCD framework, enabling the simulation of immersed granular flows. Additionally, since overlapping particles are not allowed, the numerical scheme naturally satisfies particle volume conservation.

The Discrete Element Method (DEM) can be summarised as follows. Algorithm 1 provides an overview of the key steps involved in a single time step of the DEM. First, the *free velocity* of each particle is computed by integrating the external forces (such as gravity and fluid–grain interactions) over the time step, assuming no contact interactions. Next, the *contact detection* step identifies all potential contacts between particles and between particles and

boundaries. These contacts are used to formulate the contact constraints, such as non-penetration and frictional sliding. Once contacts have been detected, the *contact problem* is solved using a Non-Smooth Contact Dynamics (NSCD) approach. This involves computing the *contact impulse* necessary to enforce the contact constraints. This impulse is then applied to adjust the velocities so that they satisfy both Newton's laws and the contact conditions. Finally, the particle positions and orientations are updated using the post-contact velocities, thus completing the time step. These updated states are then used to advance to the next time step in the simulation.

In this chapter, we present the fundamentals of the Discrete Element Method as applied to the particulate phase in fluid–granular systems, with a focus on its non-smooth dynamics formulation. We detail the theoretical framework of NSCD and its numerical implementation.

Algorithm 1: Iteration of a DEM Solver.

Require: $\mathbf{q}^n, \mathbf{v}^n, \mathbf{f}_e^n, \Delta t$

$\mathbf{v}^-$	$\leftarrow$	$\mathbf{v}^n + \Delta t \mathbf{f}_e^n$
$\mathcal{C}$	$\leftarrow$	Contact Detection
$\mathbf{p}^{n+1}, \mathbf{v}^{n+1}$	$\leftarrow$	Solve the contacts problem
$\mathbf{q}^{n+1}$	$\leftarrow$	Update the bodies position

Contents

2.1 Non-Smooth Newton–Euler Dynamics

Originally developed for geomechanical applications [36], the Discrete Element Method (DEM) has evolved into a widely adopted numerical approach for simulating the behaviour of granular materials. In this framework, each particle is modelled as a rigid body, and its motion is governed by the Newton–Euler equations. The discontinuous nature of collisions and contact interactions necessitates a non-smooth formulation of the dynamics. Generalised configuration variables are introduced to describe the particle's position and orientation, providing a comprehensive representation of its motion. This formulation leads to a concise set of equations that govern the particle's dynamics, including both linear and angular momentum balances which will be suitable to describe the contact dynamics.

2.1.1 Rigid body kinematics

A rigid body can be described using generalised coordinates, which represent its position $\mathbf{y} \in \mathbb{R}^3$ and its orientation, represented by a unit quaternion $\boldsymbol{\theta} \in \mathbb{H}^4$ in the Euclidean space $\mathbb{R}^3$. For two-dimensional systems, a single angle is sufficient to describe the orientation. For numerical purposes, unit quaternions are often preferred to Euler angles or a rotation matrix due to their computational efficiency and numerical stability. The generalised velocity, denoted $\mathbf{v}$, relates the generalised coordinates to the linear and angular velocities in the body-fixed reference frame:

$$\mathbf{q} = \begin{bmatrix} \mathbf{y} \\ \boldsymbol{\theta} \end{bmatrix}, \qquad \mathbf{v} = \begin{bmatrix} \dot{\mathbf{y}} \\ \boldsymbol{\omega} \end{bmatrix} \tag{2.1}$$

where $\dot{\mathbf{y}} \in \mathcal{R}^3$ is the linear velocity and $\boldsymbol{\omega} \in \mathcal{R}^3$ is the angular velocity.

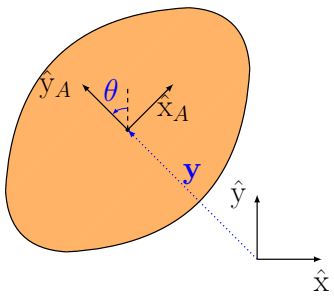

Figure 2.1: Configuration variables of a rigid body.

The time derivative of the orientation, $\boldsymbol{\theta} \in \mathbb{H}^4$ is related to the angular velocity, $\boldsymbol{\omega} \in \mathbb{R}^3$ by:

$$\dot{\boldsymbol{\theta}} = \frac{1}{2}\mathbf{Q}(\boldsymbol{\theta})\boldsymbol{\omega} \tag{2.2}$$

$$\dot{\boldsymbol{\theta}} = \frac{1}{2}\begin{bmatrix} -\omega_x\theta_x - \omega_y\theta_y - \omega_z\theta_z \\ \omega_x\theta_w + \omega_y\theta_z - \omega_z\theta_y \\ \omega_y\theta_w - \omega_x\theta_z + \omega_z\theta_x \\ \omega_z\theta_w + \omega_x\theta_y - \omega_y\theta_x \end{bmatrix} \tag{2.3}$$

It follows that the time derivative of the generalised coordinates $\mathbf{q}$ can be expressed as:

$$\dot{\mathbf{q}} = \mathbf{T}(\mathbf{q})\mathbf{v} \tag{2.4}$$

where $\mathbf{T}(\mathbf{q})$ is the transformation matrix from the generalised velocities to the generalised coordinates based on Equation (2.3). The generalised coordinates are defined by six degrees of freedom in three-dimensional space and three degrees of freedom in two-dimensional space. Figure 2.1 illustrates the rigid body configuration.

2.1.2 Non-Smooth Dynamics

The dynamics of a rigid body are governed by the Newton–Euler equations, which describe the motion of the particle in terms of its linear and angular momentum. External impulses act on the particle, which can be due to contact forces, fluid forces, or external forces such as gravity. Figure 2.2 illustrates the motion of a particle subjected to gravity and an external forces. To account for the non-smooth nature of contact interactions, the dynamics equations are formulated in a differential form [76, 74] :

$$\mathbf{M}\mathrm{d}\mathbf{v} = \mathbf{f}_\mathrm{e}\mathrm{d}t + \mathbf{f}_\mathrm{q}\mathrm{d}t + \mathrm{d}\mathbf{p} \tag{2.5}$$

where $\mathrm{d}\mathbf{v}$ is the differential measure of the velocity, $\mathbf{f}_\mathrm{e}$ is the external generalised force, $\mathrm{d}\mathbf{p}$ is the generalised impulse and $\mathbf{M}$ is the generalised mass matrix defined as:

$$\mathbf{M} = \begin{bmatrix} m\mathbf{I} & \mathbf{0} \\ \mathbf{0} & \mathbf{J} \end{bmatrix} \tag{2.6}$$

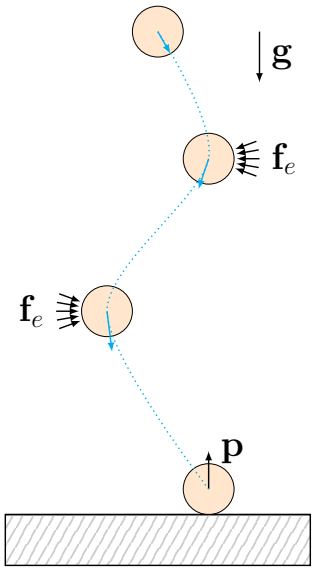

Figure 2.2: A disc subjected to external forces.

where m is the mass of the body, $\mathbf{I} \in \mathbb{R}^{3\times3}$ is the identity matrix, $\mathbf{J} \in \mathbb{R}^{3\times3}$ is the inertia matrix and $\mathbf{0} \in \mathbb{R}^{3\times3}$ is the null matrix. The generalised external force $\mathbf{f}_\mathrm{e}$ includes the external forces and moments acting on the particle, such as gravity or fluid forces. Contact forces and moments are included in the generalised impulse. Gyroscopic moments are included in the generalised quadratic force $\mathbf{f}_\mathrm{q}$, which is defined as:

$$\mathbf{f}_\mathrm{q} = \begin{bmatrix} \mathbf{0} \\ -\boldsymbol{\omega} \times \mathbf{J}\boldsymbol{\omega} \end{bmatrix} \tag{2.7}$$

For a sphere or bidimensional system, the quadratic force is zero because the inertia matrix is diagonal. This term will be omitted from the following equations, since only two-dimensional systems and symmetric particles will be considered. To model contact interactions, inequalities are used to enforce non-penetration and frictional constraints. The Discrete Element Method (DEM) solves the equations of motion for each particle in the system, Equation (2.5), neighboring particles interact through contact forces and moments.

In order to address the discontinuous nature of the contact impulse, the generalised velocity $\mathbf{v}$ is assumed to be a right continuous locally bounded variation function. This means that the measure of $]t_0, t]$ by $\mathrm{d}\mathbf{v}$ is

$$\int_{]t_0,t]} \mathrm{d}\mathbf{v} = \mathbf{v}(t) - \mathbf{v}(t_0). \tag{2.8}$$

The kinematics and dynamics of a rigid body in the non-smooth framework can be expressed as:

$$\mathbf{q}(t) - \mathbf{q}(t_0) = \int_{]t_0,t]} \mathbf{T}(\mathbf{q})\ \mathrm{d}\mathbf{v}, \tag{2.9}$$

$$\mathbf{M}\Big(\mathbf{v}(t) - \mathbf{v}(t_0)\Big) = \int_{]t_0,t]} \mathbf{f}_\mathrm{e}\ \mathrm{d}t + \mathbf{p}. \tag{2.10}$$

The unknowns in these equations are the generalised coordinates $\mathbf{q}$, the generalised velocities $\mathbf{v}$, and the generalised impulses $\mathbf{p}$. In practice, the external force $\mathbf{f}_\mathrm{e}$ is integrated explicitly, and the *free velocity* $\mathbf{v}^-$ is defined as the velocity the body would get in the absence of contact interactions:

$$\mathbf{v}^- = \mathbf{v}(t_0) + \mathbf{M}^{-1}\mathbf{f}_\mathrm{e}\Delta t, \tag{2.11}$$

where $\mathbf{M}$ is the mass matrix and Δt is the time step. It leads to the following expression for the body dynamics:

$$\mathbf{M}(\mathbf{v}^+ - \mathbf{v}^-) = \mathbf{p}, \tag{2.12}$$

where $\mathbf{v}^+$ and $\mathbf{v}^-$ denote the post and pre-impact velocities, respectively. The unknown quantities in this equation are the post-impact velocity $\mathbf{v}^+$ and the contact impulse $\mathbf{p}$. The next section introduces the *Contact Dynamics* method, which uses non-overlapping and frictional contact constraints to determine these quantities.

2.2 Contact Dynamics

The core principle of the Non-Smooth Contact Dynamics (NSCD) method is to treat contact events as discontinuous impulse. All contacts occurring within a time step are considered instantaneous and are solved simultaneously. This approach enables the simulation of contact dynamics even when the duration of contact tends toward zero. However, a fundamental trade-off of this method is the loss of uniqueness of the solution, meaning that multiple valid outcomes may exist for a given configuration. The method can be divided into three main stages:

Contact Detection involves identifying potential contact pairs. This is done by computing the distance between particles and checking whether they are sufficiently close to interact. A naive approach would involve checking all possible particle pairs, but this becomes computationally infeasible for large systems. To address this issue, tree-based spatial partitioning algorithms are employed to efficiently detect potential contacts using particle bounding boxes. As a consequence of the detection step, a time step restriction arises from this stage to ensure accurate detection.

Local Contact Resolution Once potential contacts have been identified, each one is treated individually. A local contact frame is then defined at each contact point to serve as the reference basis for expressing contact conditions. Within this frame, non-overlapping constraints, friction, and inelastic collision conditions are formulated as inequalities. The contact dynamics are therefore expressed in terms of complementarity conditions within this local frame.

Global Resolution Solving the full contact problem involving multiple interacting bodies requires iterative algorithms. Since multiple contacts can act simultaneously on a single body, the contact problem is inherently coupled and nonlinear. To handle these interdependencies and ensure a consistent global solution, iterative schemes are employed to progressively converge towards a stable configuration. Commonly used methods include the *Nonlinear Gauss–Seidel* algorithm [40, 77], *Conjugate Gradient*

methods [78], and optimisation-based approaches such as the *Accelerated Gradient Scheme* [39].

This section details the procedures for both local and global contact resolution. First, we introduce the kinematics of contact, including the definition of the contact frame and the associated transformation matrix. Next, we present Signorini's condition, which enforces the non-penetration constraint between interacting bodies. This is followed by a discussion of Coulomb's friction law, which governs the tangential forces that arise at contact points. Finally, we describe the Gauss–Seidel algorithm, an efficient iterative method for solving the global multi-contact problem.

2.2.1 Contact Kinematics

To express the equations of motion in the local frame, we introduce a local frame associated with the contact point. Let $\mathbf{n}$ be the unit normal vector to the contact plane and $\mathbf{s}$ and $\mathbf{t}$ be the two tangential vectors in the contact plane. The normal vector is defined as the unit vector pointing from the two closest point between body A and body B. It leads that the gap between the two bodies is given by,

$$g(t) = \mathbf{n} \cdot (\mathbf{y}_A^{\mathrm{c}} - \mathbf{y}_B^{\mathrm{c}}), \tag{2.13}$$

where $\mathbf{y}_A^{\mathrm{c}}$ is the closest point from body A to body B and $\mathbf{y}_B^{\mathrm{c}}$ is the closest point to body A on body B. Figure 2.3 illustrates the local frame associated with the contact point.

We seek to express the equations of motion in the local frame associated with the contact point. The absolute velocity at the contact point in the global frame is given by :

$$\mathbf{v} = \dot{\mathbf{y}} + \boldsymbol{\omega} \times \mathbf{y}^{\mathrm{c}}, \tag{2.14}$$

$$= \begin{bmatrix} \mathbf{I} & \mathbf{R} \end{bmatrix} \begin{bmatrix} \dot{\mathbf{y}} \\ \boldsymbol{\omega} \end{bmatrix} \tag{2.15}$$

$$\tag{2.16}$$

where $\mathbf{I}$ is the identity matrix, $\mathbf{R}$ the skew-symmetric matrix use to express the vector cross-product as a matrix-vector product:

$$\mathbf{R} = \begin{bmatrix} 0 & \mathrm{z}^{\mathrm{c}} & -\mathrm{y}^{\mathrm{c}} \\ -\mathrm{z}^{\mathrm{c}} & 0 & \mathrm{x}^{\mathrm{c}} \\ \mathrm{y}^{\mathrm{c}} & -\mathrm{x}^{\mathrm{c}} & 0 \end{bmatrix}, \tag{2.17}$$

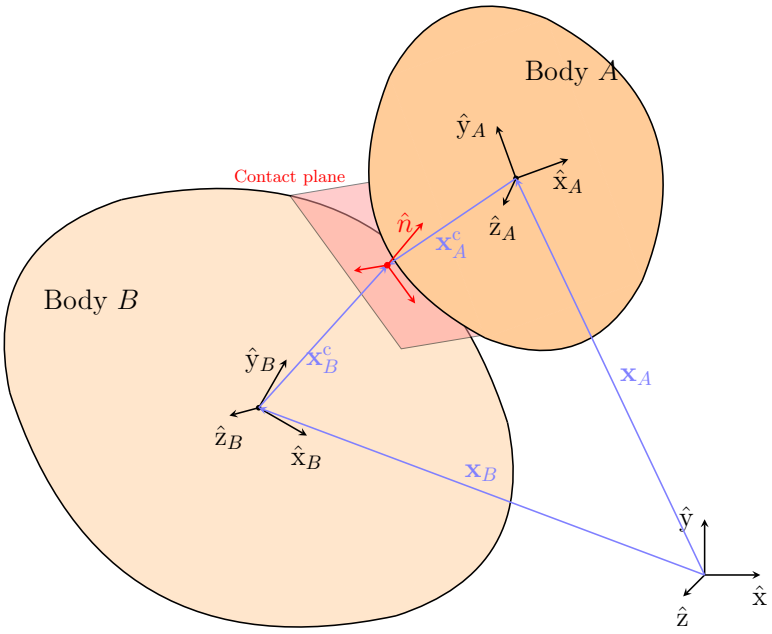

Figure 2.3: Local frames associated with the contact problem.

The absolute velocity and the contact impulse, respectively denoted by $\mathbf{u}$ and $\mathbf{r}$, can be expressed in the local frame as:

$$\mathbf{u} = \mathbf{H}^T \mathbf{v}, \tag{2.18}$$
$$\mathbf{p} = \mathbf{H}\mathbf{r}, \tag{2.19}$$

where $\mathbf{H}$ maps the global frame to the local frame at the contact point, defined as:

$$\mathbf{H} = \begin{bmatrix} \mathbf{I} \\ \mathbf{R} \end{bmatrix} \mathbf{B}, \qquad \mathbf{B} = \begin{bmatrix} \mathbf{n} & \mathbf{s} & \mathbf{t} \end{bmatrix}, \tag{2.20}$$

where $\mathbf{B}$ is change of basis matrix from the local frame to the global frame. It should be recall that the contact point and The transformation matrix $\mathbf{H}$ are not known a priori as they depends on the bodies configuration.

Over a singleton $\{t^c\}$, the jump velocity at the contact point, Equation

(2.12), can be expressed in the local frame as:

$$\mathbf{M}(\mathbf{v}^+ - \mathbf{v}^-) = \mathbf{p}, \tag{2.21}$$
$$\mathbf{v}^+ - \mathbf{v}^- = \mathbf{M}^{-1}\mathbf{p}, \tag{2.22}$$
$$\mathbf{H}^T(\mathbf{v}^+ - \mathbf{v}^-) = \mathbf{H}^T\mathbf{M}^{-1}\mathbf{H}\mathbf{r}, \tag{2.23}$$
$$\mathbf{u}^+ - \mathbf{u}^- = \mathbf{H}^T\mathbf{M}^{-1}\mathbf{H}\mathbf{r}, \tag{2.24}$$

It is convenient to introduce the Delassus operator $\mathbf{W}$ which describes the change of velocity at the contact point due to the contact impulse,

$$\mathbf{u}^+ - \mathbf{u}^- = \mathbf{W}\mathbf{r}, \qquad \mathbf{W} = \mathbf{H}^T\mathbf{M}^{-1}\mathbf{H}, \tag{2.25}$$

At the contact point between two bodies A and B, the dynamics at the contact point is expressed as:

$$\mathbf{u}_A^+ = \mathbf{u}_A^- + \mathbf{W}_A\mathbf{r}, \qquad \mathbf{W}_A = \mathbf{H}_A^T\mathbf{M}_A^{-1}\mathbf{H}_A \tag{2.26}$$
$$\mathbf{u}_B^+ = \mathbf{u}_B^- - \mathbf{W}_B\mathbf{r}, \qquad \mathbf{W}_B = \mathbf{H}_B^T\mathbf{M}_B^{-1}\mathbf{H}_B \tag{2.27}$$

Let $\delta\mathbf{u} = \mathbf{u}_A - \mathbf{u}_B$ be the relative velocity at the contact point. The dynamics at the contact point is:

$$\delta\mathbf{u}^+ = \delta\mathbf{u}^- + \mathbf{W}\mathbf{r}, \qquad \mathbf{W} = \mathbf{W}_A + \mathbf{W}_B \tag{2.28}$$

Regarding this equation, both the contact impulse $\mathbf{r}$ and the relative velocity $\delta\mathbf{u}^+$ are unknown. In three-dimensional space, six unknowns have to be solved, the contact dynamics, Equation (2.28) only provides three equations. To close the system, non-overlapping conditions are imposed at the contact point and constitutive laws are introduced to model tangential reactions with inelastic collisions.

2.2.2 Signorini's Condition

Non-smooth methods seek to prevent overlapping between two bodies. This is why they are also referred as hard-sphere methods. To ensure non-overlapping, the gap, Equation (2.13), is set to be non-negative

$$g(t) \geq 0, \tag{2.29}$$

This condition is referred as the unilateral constraint. As two bodies are close to one another without contact, the gap is positive and the normal contact impulse is zero. When the two bodies are in contact, the gap is zero and the

normal contact impulse is positive. This situation is referred as the Signorini's condition:

$$g(t) \geq 0, \qquad \text{(Impenetrability)}, \tag{2.30}$$
$$\mathrm{r}_n(t) \geq 0, \qquad \text{(No attraction)}, \tag{2.31}$$
$$\mathrm{r}_n(t) g(t) = 0, \qquad \text{(Signorini's condition)}, \tag{2.32}$$

where r_n is the normal contact impulse. Figure 2.4a illustrates the Signorini's condition.

2.2.3 Frictional Contact Law

In order to fully describe the contact dynamics, constitutive laws are required to model the contact forces. Inelastic shock and Coulomb's friction law are the ones considered in this work. The inelastic shock states that if a contact occurs, the contact normal velocity vanishes after the contact,

$$g(t) = 0 \Rightarrow \mathrm{r}_n(t) \geq 0, \qquad \delta \mathrm{u}_n^+ = 0. \tag{2.33}$$

Coulomb's friction law states that the tangential contact impulse is opposite to the tangential velocity at the contact point and that its magnitude belongs to the friction cone with a friction coefficient μ. Figure 2.4b illustrates the Coulomb's friction law for a two-dimensional system. In the contact frame, the Coulomb's friction law can be expressed as:

$$\|\mathbf{r}_t\| \leq \mu \mathrm{r}_n, \tag{2.34}$$
$$\left\|\delta \mathbf{u}_t^+\right\| \neq 0 \Rightarrow \mathbf{r}_t = -\mu \mathrm{r}_n \frac{\delta \mathbf{u}_t^+}{\left\|\delta \mathbf{u}_t^+\right\|}. \tag{2.35}$$

where $\mathbf{r}_t$ is the tangential contact impulse and $\delta \mathbf{u}_t^+$ is the tangential velocity at the contact point defined as:

$$\mathbf{r}_t = \mathbf{r} - \mathrm{r}_n \mathbf{n}, \qquad \delta \mathbf{u}_t^+ = \delta \mathbf{u}^+ - \delta \mathrm{u}_n^+ \mathbf{n}. \tag{2.36}$$

2.2.4 A Brief Summary

For a given contact point, the contact impulse and the relative velocity are determined to satisfy the contact dynamics, the Signorini condition (impenetrability), Coulomb's friction law (Coulomb's cone and slipping), and the inelastic impact condition (no restitution).

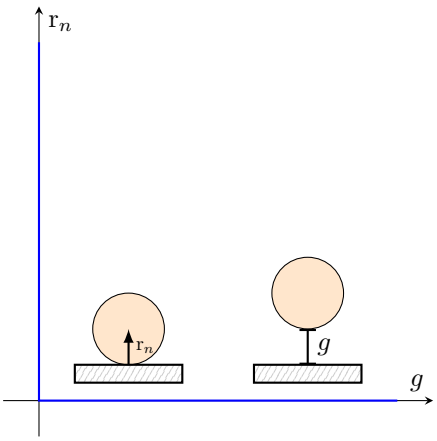

(a) Signorini's condition.

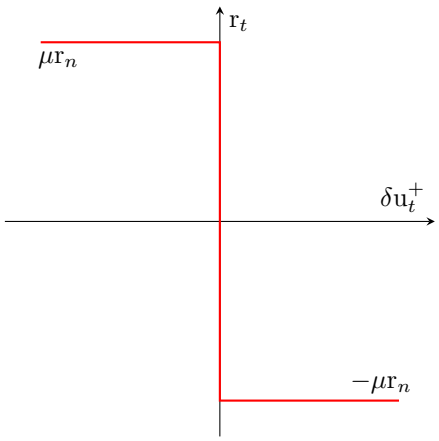

(b) Coulomb's friction law.

$$
\begin{aligned}
&\delta \mathbf{u}^+ = \delta \mathbf{u}^- + \mathbf{W}\mathbf{r}, && \text{(Contact Dynamics)}\\
&g(t) \geq 0, && \text{(Impenetrability)},\\
&r_n(t) \geq 0, && \text{(No attraction)},\\
&r_n(t) g(t) = 0, && \text{(Signorini's condition)},\\
&g(t) = 0 \Rightarrow r_n(t) \geq 0, \delta u_n^+ = 0, && \text{(No restitution)}.\\
&\|\mathbf{r}_t\| \leq \mu r_n, && \text{(Coulomb's cone)}\\
&\left\|\delta \mathbf{u}_t^+\right\| \neq 0 \Rightarrow \mathbf{r}_t = -\mu r_n \frac{\delta \mathbf{u}_t^+}{\left\|\delta \mathbf{u}_t^+\right\|}, && \text{(Slipping)}.
\end{aligned}
\tag{2.37}
$$

The complete contact problem is inherently nonlinear, so finding a solution is not trivial. Fortunately, in two-dimensional problems, an explicit solution can often be obtained using a graphical interpretation of the contact laws. This allows for a direct construction of the contact impulse that satisfies the Signorini condition, Coulomb's friction law, and the inelastic impact condition. However, in three-dimensional configurations, the contact space becomes more complex, and an iterative procedure is typically required to find the correct contact impulse at each contact point. The following paragraph illustrates how the contact solution can be obtained explicitly in a bidimensional problem.

A bidimensional example — Let us assume an active contact between two bidimensional bodies, *i.e.* the gap is zero. The contact solution is the relative velocity and the contact impulse such that both the contact dynamics and the Coulomb's friction law are satisfied. The solution can be found graphically by determining the intersection between the contact dynamics and the

Coulomb friction law, as illustrated in Figure 2.5. To discuss this intersection, we introduce the stick impulse, which is the impulse such that the relative velocity vanishes:

$$\mathbf{r}^{\text{stick}} = -\mathbf{W}^{-1}\delta\mathbf{u}^{-}. \tag{2.38}$$

If the stick solution is inside the friction cone, then the contact is in stick mode and the contact impulse is equal to the stick impulse. If the stick solution is outside the friction cone, then the contact is in slip mode and the contact impulse is equal to the boundary of the friction cone. The sign of the stick tangential impulse determines the direction of the slip either forward or backward,

$$\text{if } \mathrm{r}_t^{\text{stick}} - \mu \mathrm{r}_n^{\text{stick}} < 0, \quad \text{then } \mathrm{r}_t = -\mu \mathrm{r}_n \tag{2.39}$$

$$\text{if } \mathrm{r}_t^{\text{stick}} + \mu \mathrm{r}_n^{\text{stick}} > 0, \quad \text{then } \mathrm{r}_t = \quad \mu \mathrm{r}_n \tag{2.40}$$

Finally, the tangential contact impulse is injected into the contact dynamics, a 2×2 system of linear equations is obtained,

$$\begin{bmatrix} 0 \\ \delta \mathrm{u}_t^{+} \end{bmatrix} = \begin{bmatrix} \mathrm{W}_{nn} & \mathrm{W}_{nt} \\ \mathrm{W}_{tn} & \mathrm{W}_{tt} \end{bmatrix} \begin{bmatrix} \mathrm{r}_n \\ \mathrm{r}_t \end{bmatrix} + \begin{bmatrix} \delta \mathrm{u}_n^{-} \\ \delta \mathrm{u}_t^{-} \end{bmatrix}. \tag{2.41}$$

From this system, the tangential velocity and the normal impulse can be isolated and thus, the contact problem has been fully solved.

In this section, we present the Non-Smooth Contact Dynamics (NSCD) framework for modelling a single collision between two bodies. The dynamics are described in a local frame associated with the contact point. To ensure non-penetration at all times, Signorini's condition is applied. To close the system of equations, constitutive laws are introduced to model the contact forces–specifically, the inelastic impact condition and Coulomb's friction law. However, in practical scenarios, multiple contacts typically occur within a single time step. Resolving these interactions requires solving a global multi-contact problem. The following section details the iterative algorithm used to compute a consistent set of contact impulses that satisfies all constraints.

2.3 When One Contact Isn't Enough

In most realistic scenarios, multiple contacts occur simultaneously within a single time step. The objective is to determine a global contact impulse such that each local contact problem satisfies the conditions outlined in Equation (2.2.4).

Given that the current implementation is sequential, we assume contacts are resolved one after another. However, this resolution introduces a challenge: solving one contact updates the velocities of the involved bodies, which

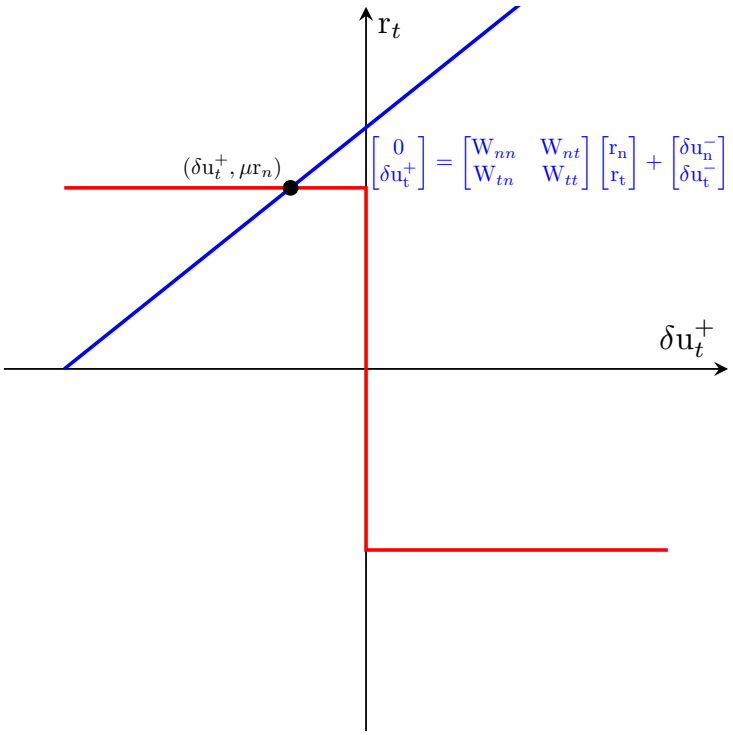

Figure 2.5: Coulomb's friction contact solution procedure.

may, in turn, affect other previously solved contacts. To address this coupling, iterative schemes are employed to achieve convergence. Common methods include the *Nonlinear Gauss–Seidel* algorithm [40, 77] and *Conjugate Gradient methods* [78]. Optimisation-based approaches such as the *Accelerated Gradient Scheme* [39] have also shown promise, offering efficient convergence properties.

In this work, we adopt the Nonlinear Gauss–Seidel method to solve the multi-contact problem. Algorithm 2 summarizes the procedure. Let us assume that all detected contacts are stored in a list $\mathcal{C}$. The algorithm begins with an initial guess for the contact impulses, denoted $\mathbf{r}_0$. It then iteratively loops through each contact in $\mathcal{C}$. For each contact, the previously applied contact impulse is removed from the bodies. Then the local contact problem is solved using Equation (2.2.4), yielding an updated contact impulse. This contact impulse is then re-applied to the bodies involved in the contact. To assess local convergence, the displacement at the contact point is compared to that from the previous iteration. If the change is below a specified tolerance ξ, the contact is considered to have converged and the previous contact impulse is applied. The algorithm terminates once all contacts satisfy the local convergence criterion.

Algorithm 2: Non-Linear Gauss Seidel Loop.

Data: Initial guess $\mathbf{r}_0$
k = 0;
converged = False;
while *not converged* **do**
  for *Each contact* $\alpha \in \mathcal{C}$ **do**
    k += 1;
    $\mathbf{v}_0^\alpha, \mathbf{v}_1^\alpha \rightarrow$ Unapply the contact impulse $\mathbf{r}_{k-1}^\alpha$;
    $\delta\mathbf{u}_k^\alpha, \mathbf{r}_k^\alpha \rightarrow$ Solve the local contact problem;
    $\mathbf{v}_0^\alpha, \mathbf{v}_1^\alpha \rightarrow$ Apply the contact impulse $\mathbf{r}_k^\alpha$;
    if $\left\|\delta\mathbf{u}_k^\alpha - \delta\mathbf{u}_{k-1}^\alpha\right\|\Delta t < \xi$ **then**
      converged = True;
      $\mathbf{v}_0^\alpha, \mathbf{v}_1^\alpha \rightarrow$ Unapply the contact impulse $\mathbf{r}_k^\alpha$;
      $\mathbf{v}_0^\alpha, \mathbf{v}_1^\alpha \rightarrow$ Apply the contact impulse $\mathbf{r}_{k-1}^\alpha$;
    end
  end
end

Optimisation As observed in the previously described algorithm, even if only a few contacts require additional iterations to converge, the algorithm continues to loop over all contacts at each step. This inefficiency has been addressed by introducing a queue to manage contact resolution more effectively. Initially, all detected contacts are inserted into the queue. We then iterate through the queue, solving one contact at a time. If a contact fails to converge, it is reinserted back into the queue, along with all contacts involving the same bodies. This strategy focuses computational effort on unresolved contacts and their immediate neighbors, which are most likely to be affected. Consequently, the algorithm becomes more efficient by dynamically adapting its focus to the regions of the system where convergence has not yet been achieved.

Conclusion

In this chapter, we present the Non-Smooth Contact Dynamics (NSCD) framework for modelling contact interactions between rigid bodies. This method treats contact events as instantaneous and discontinuous, represented through impulses. The NSCD approach enables the robust simulation of systems with many simultaneous contacts, such as granular materials.

Algorithm 3 summarises the overall procedure for the NSCD method. The free velocity $\mathbf{v}^-$ is computed based on the external forces acting on the bodies. Potential contacts are detected, and the contact impulse is computed using the Nonlinear Gauss–Seidel algorithm. Finally, the bodies positions are updated

based on the computed velocities. The time step Δt must be chosen to ensure stability in the explicit force computation and to allow for an accurate contact detection.

Algorithm 3: NSCD Overview.

Require: $\mathbf{q}^n, \mathbf{v}^n, \mathbf{f}_e^n, \Delta t$

$\mathbf{v}^-$	$\leftarrow$	$\mathbf{v}^n + \Delta t \mathbf{f}_e^n$
$\mathcal{C}$	$\leftarrow$	Contact Detection
$\mathbf{p}^{n+1}, \mathbf{v}^{n+1}$	$\leftarrow$	NonLinear Gauss-Seidel
$\mathbf{q}^{n+1}$	$\leftarrow$	Update the bodies position

In the next chapter, we turn our attention to the fluid phase representation and detail the coupling strategy between the fluid and solid phases.

CHAPTER 3

Numerical Modelling of Immersed Granular Flows

> In theory, there is no difference
> between theory and practice.
> In practice, there is.
>
> — Yogi Berra.

Immersed granular flows involve the motion of solid particles that are either fully or partially suspended in a surrounding fluid. Such systems are prevalent in both natural and industrial environments, with examples including sediment transport in rivers, slurry conveyance in pipelines, and debris flows triggered by landslides. A defining characteristic of immersed granular flows is the complex interplay between the particles and the interstitial fluid, leading to a diverse range of behaviours that span the continuum from fluid-like to solid-like dynamics. Accurately capturing these behaviours is essential for predictive modelling in environmental and engineering applications.

In such systems, hydrodynamic interactions play a key role in determining particle motion. These interactions include drag, lubrication forces, added mass effects, and Basset history forces, all of which stem from the fluid's viscous and inertial properties. A key dimensionless parameter that governs the nature of these flows is the Stokes number, St, which expresses the relative importance

of particle inertia compared to viscous forces: $\mathrm{St} = \frac{\rho_g \dot{\gamma} d^2}{\eta}$, where ρ_g is the particle density, $\dot{\gamma}$ is the shear rate, d is the particle diameter, and η is the dynamic viscosity of the fluid. For small Stokes numbers ($\mathrm{St} \ll 1$), viscous forces dominate and strongly couple particle and fluid motion. In contrast, for large Stokes numbers ($\mathrm{St} \gg 1$), inertial effects prevail, and the system behavior approaches that of dry granular flows.

The presence of particles also alters the macroscopic rheology of the fluid-particle suspension. In dilute systems ($\phi < 0.1$), the effective viscosity increases approximately quadratically with the particle volume fraction [34]. As the suspension becomes denser, the viscosity rises sharply and may diverge near the jamming transition. This non-linear increase is well described by the Krieger–Dougherty model [35]: $\eta_{\text{eff}} = \eta \left(1 - \frac{\phi}{\phi_c}\right)^{-\alpha}$, where ϕ_c denotes the critical packing fraction and α is a fitting exponent. Such behavior highlights the intricate coupling between particle interactions and fluid rheology, resulting in suspensions that may behave like Newtonian fluids in dilute regions, and as highly viscous or jammed materials in dense zones.

Simulating immersed granular flows poses significant computational challenges due to the multiscale and multiphase nature of the system. While fully resolving the fluid motion around each individual particle would offer the most accurate representation, it is prohibitively expensive for large-scale applications. Consequently, a variety of numerical strategies have been developed, each balancing physical accuracy and computational efficiency.

The two-fluid model treats the solid and fluid phases as interpenetrating continua, which are governed by volume-averaged conservation laws for mass, momentum, and energy [11]. Coupling terms such as drag force account for interphase interactions. Although this approach is computationally efficient and well-suited to large-scale simulations, it often struggles to capture particle-scale effects and requires empirical closure relations to approximate unresolved microscale physics.

A more detailed alternative is the CFD-DEM method, which combines the Discrete Element Method (DEM) to model particle motion with classical Computational Fluid Dynamics (CFD) methods to model the fluid phase [49, 51, 48]. This hybrid framework explicitly resolves particle-particle and particle-fluid interactions, enabling accurate modelling of complex phenomena such as clustering, jamming, and segregation. However, its computational cost increases steeply with the number of particles and the complexity of the interactions, particularly in dense suspensions. Like the two-fluid model, its accuracy is highly dependent on the closure relations used to model the interphase forces.

The semi-resolved method [52, 53] bridges the gap between fully resolved and unresolved approaches. In this method, the resolution of the fluid, i.e. the mesh size, is comparable to the diameter of the particles, enabling the partial resolution of near-field flow structures without fully capturing the boundary

layers. To achieve this, a smoothing kernel is typically introduced to distribute particle forces and velocities onto the fluid mesh. This kernel spreads the particle quantities over a region larger than a single mesh element. Near boundaries, renormalisation of the kernel is often necessary to ensure conservation of volume. While the semi-resolved method improves accuracy over purely unresolved approaches, it still inherits their stability limitations and can be difficult to apply in geometrically complex domains.

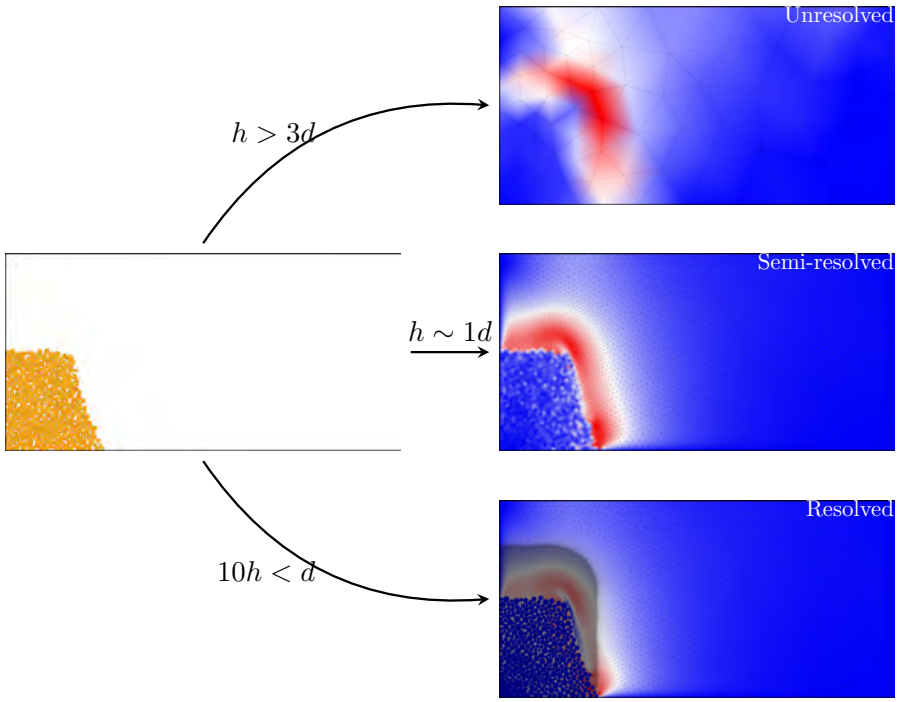

Figure 3.1: Grains representation paradigms. On the left, an avalanche of grains in a box. On the right, the filtered fluid velocity $\varepsilon\|u\|$, The mesh is shown in gray. From top to bottom, the three paradigms are : unresolved, semi-resolved and resolved.

In this chapter, we revisit the volume-averaged fluid formulation coupled with a discrete granular phase in the context of the Finite Element Method. Next, we introduce an overlap-wise particle integration scheme to transfer particle forces to the fluid mesh, eliminating the need for an additional kernel interpolation. A semi-implicit time integration scheme ensures stability and prevents degeneracy, even when mesh elements are fully occupied by particles. This enables the method to handle arbitrary mesh sizes and complex geometries, making it well-suited for free-surface and dense granular flows. A key feature of our approach is its ability to transition seamlessly between un-

resolved, semi-resolved, and resolved regimes without altering the numerical scheme, as shown in Figure 3.1. This is demonstrated by various test cases, including a sedimentation test and the granular Rayleigh–Taylor instability. The method remains computationally efficient by modelling fine-scale boundary effects through constitutive laws rather than mesh refinement, while still capturing key hydrodynamic interactions such as drag and momentum exchange.

Contents

3.1 Fluid Governing Equations

The dynamics of an incompressible Newtonian fluid are described by the Navier–Stokes equations, subject to no-slip boundary conditions at the fluid–solid interface. While the motion of individual grains is governed by the Newton–Euler equations, directly resolving the fluid flow around each grain becomes computationally infeasible for large-scale systems.

To overcome this limitation, a volume-averaged description is adopted, based on the framework introduced by Anderson [48]. This methodology extends the fluid phase over the granular domain using a filtering operation, which necessitates closure models for fluid–grain interaction and unresolved stress contributions. The resulting Volume-Averaged Navier–Stokes (VANS) equations enable the fluid phase to be simulated across the mixture domain without explicitly resolving the flow around each particle. Figure 3.2 illustrates the unresolved representation of the flow, as the fluid phase is captured at the mesh scale and the grains are captured by the Discrete Element Method.

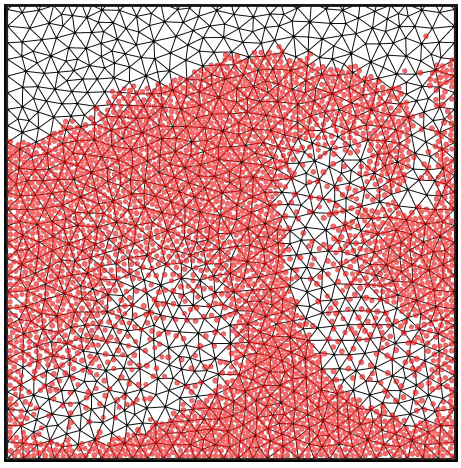

Figure 3.2: Unresolved flow representation: The fluid phase is governed by the volume-averaged Navier–Stokes equations at the mesh scale, while particles (red discs) are modeled using the Discrete Element Method (DEM).

This section presents the derivation of the VANS equations. The process begins with the Navier–Stokes equations, proceeds through the introduction of a filtering operator, and concludes with the derivation of the VANS equations and their associated closure models. Readers who are already familiar with the VANS equations can skip ahead to Section 3.1.4, which summarises of the governing equations.

We consider a domain composed of a fluid region Ω_f and a solid region Ω_s, where the no-slip condition is enforced on the surface of each grain, denoted

by Γ_s. The problem for the fluid phase is:

$$\begin{cases} \boldsymbol{\nabla} \cdot \boldsymbol{u} = 0, & \text{in } \Omega_f, \\ \partial_t(\rho \boldsymbol{u}) + \boldsymbol{\nabla} \cdot (\rho \boldsymbol{u} \otimes \boldsymbol{u}) = \boldsymbol{\nabla} \cdot \boldsymbol{\sigma} + \rho \boldsymbol{g}, & \text{in } \Omega_f, \\ \boldsymbol{u} = \boldsymbol{v}, & \text{on } \Gamma_s, \end{cases} \tag{3.1}$$

where $\boldsymbol{u}$ is the fluid velocity, $\boldsymbol{v}$ is the solid velocity, ρ is the fluid density, $\boldsymbol{\sigma}$ is the Cauchy stress tensor, and $\boldsymbol{g}$ is the gravitational acceleration. The stress tensor is defined as

$$\boldsymbol{\sigma} = -p\boldsymbol{I} + \mu \left(\boldsymbol{\nabla} \boldsymbol{u} + \boldsymbol{\nabla}^{\mathrm{T}} \boldsymbol{u} \right), \tag{3.2}$$

where p denotes the pressure, μ is the dynamic viscosity, and $\boldsymbol{I}$ is the identity tensor. The force exerted by the fluid on an individual grain is given by

$$\mathbf{f} = \int_{\Gamma_s} \boldsymbol{\sigma} \cdot \boldsymbol{n} \ \mathrm{d}S, \tag{3.3}$$

where $\boldsymbol{n}$ is the unit normal vector on Γ_s.

3.1.1 Filtering Operation

The filtering operation decomposes the fluid properties into macroscopic (filtered) and microscopic (fluctuating) components. For any field $\boldsymbol{a}(\boldsymbol{x}, t)$, we write:

$$\boldsymbol{a}(\boldsymbol{x}, t) = \bar{\boldsymbol{a}}(\boldsymbol{x}, t) + \tilde{\boldsymbol{a}}(\boldsymbol{x}, t), \tag{3.4}$$

where $\bar{\boldsymbol{a}}$ represents the filtered quantity and $\tilde{\boldsymbol{a}}$ the fluctuation. Filtering is performed using a kernel $\delta(r)$, where $r = \|\boldsymbol{x} - \boldsymbol{y}\|$, satisfying:

$$\begin{aligned} &\delta(r) \geq 0, \qquad \frac{\mathrm{d}\delta(r)}{\mathrm{d}r} \leq 0 \\ &\delta(r) \in \mathbb{L}^{\infty}, \quad \int_{\Omega} \delta(r) \ \mathrm{d}\Omega = 1. \end{aligned} \tag{3.5}$$

Figure 3.5 illustrates a typical kernel $\delta(r)$ function, the Gaussian kernel. This kernel determines the influence of neighbouring points within the fluid domain. The local void fraction, i.e. the fluid volume fraction, at position $\boldsymbol{x}$ is defined as

$$\varepsilon(\boldsymbol{x}, t) = \int_{\Omega_f} \delta(r) \ \mathrm{d}\Omega, \tag{3.6}$$

and the local particle volume fraction is given by

$$\phi(\boldsymbol{x}, t) = \int_{\Omega_p} \delta(r) \ \mathrm{d}\Omega. \tag{3.7}$$

These two fields form a partition of unity,

$$\varepsilon(\boldsymbol{x},t)+\phi(\boldsymbol{x},t)=1. \tag{3.8}$$

The filtered value of $\boldsymbol{a}$ then satisfies

$$\varepsilon(\boldsymbol{x},t)\bar{\boldsymbol{a}}(\boldsymbol{x},t)=\int_{\Omega_f}\boldsymbol{a}(\boldsymbol{y},t)\;\delta(\|\boldsymbol{x}-\boldsymbol{y}\|)\;\;\mathrm{d}\boldsymbol{y}. \tag{3.9}$$

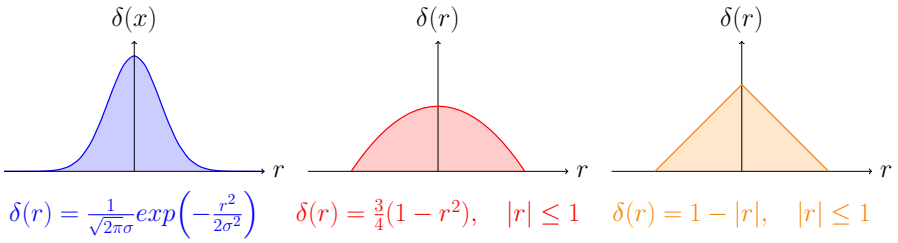

Figure 3.3: Filtering operation: the kernel $\delta(r)$ is centered at $\boldsymbol{x}$ and integrates over the fluid domain Ω_f. From left to right: Gaussian kernel, Epanechnikov kernel, and triangular kernel.

3.1.1.1 Derivative operators

Applying the filtering operation to derivatives introduces additional surface contributions due to the moving boundary and the grains presence:

$$\int_{\Omega_f}\partial_t\boldsymbol{a}\,\delta(\|\boldsymbol{x}-\boldsymbol{y}\|)\;\mathrm{d}\boldsymbol{y}=\;\;\partial_t\left(\varepsilon\bar{\boldsymbol{a}}\right)\;\;+\int_{\Gamma_s}(\boldsymbol{n}\cdot\boldsymbol{v})\boldsymbol{a}\delta(\|\boldsymbol{x}-\boldsymbol{y}\|)\;\mathrm{d}\boldsymbol{y}, \tag{3.10}$$

$$\int_{\Omega_f}\boldsymbol{\nabla}\cdot\boldsymbol{a}\,\delta(\|\boldsymbol{x}-\boldsymbol{y}\|)\;\mathrm{d}\boldsymbol{y}=\boldsymbol{\nabla}\cdot\left(\varepsilon\bar{\boldsymbol{a}}\right)-\int_{\Gamma_s}(\boldsymbol{n}\cdot\boldsymbol{a})\delta(\|\boldsymbol{x}-\boldsymbol{y}\|)\;\mathrm{d}\boldsymbol{y}, \tag{3.11}$$

$$\int_{\Omega_f}\boldsymbol{\nabla}\boldsymbol{a}\,\delta(\|\boldsymbol{x}-\boldsymbol{y}\|)\;\mathrm{d}\boldsymbol{y}=\;\;\boldsymbol{\nabla}\left(\varepsilon\bar{\boldsymbol{a}}\right)\;\;-\int_{\Gamma_s}(\boldsymbol{n}\otimes\boldsymbol{a})\delta(\|\boldsymbol{x}-\boldsymbol{y}\|)\;\mathrm{d}\boldsymbol{y}. \tag{3.12}$$

These surface terms come from the integration by parts and the application of the divergence theorem.

3.1.2 Volume-averaged Navier-Stokes equations

The VANS equations are obtained by multiplying the pointwise Navier–Stokes equations by the filtering kernel and integrating the result over the fluid domain Ω_f.

Continuity equation

Applying the filtering operation to the incompressibility constraint (3.1) yields:

$$\nabla \cdot (\varepsilon \bar{\boldsymbol{u}}) - \int_{\Gamma_s} (\boldsymbol{n} \cdot \boldsymbol{u})\ \delta(\|\boldsymbol{x} - \boldsymbol{y}\|)\ \mathrm{d}\boldsymbol{y} = 0. \tag{3.13}$$

Using the no-slip boundary condition and the filtered time derivative property (3.10), we obtain:

$$\frac{\partial \varepsilon}{\partial t} + \nabla \cdot (\varepsilon \bar{\boldsymbol{u}}) = 0. \tag{3.14}$$

Similarly, the continuity equation for the solid phase is:

$$\frac{\partial \phi}{\partial t} + \nabla \cdot (\phi \bar{\boldsymbol{v}}) = 0. \tag{3.15}$$

Adding these two equations together results in the conservation of the total volume:

$$\nabla \cdot (\varepsilon \bar{\boldsymbol{u}} + \phi \bar{\boldsymbol{v}}) = 0, \tag{3.16}$$

where the term $(\varepsilon \bar{\boldsymbol{u}} + \phi \bar{\boldsymbol{v}})$ represents the volume-averaged mixture velocity.

Momentum equation

When the momentum equation (3.1) is filtered, the left-hand side becomes:

$$\begin{aligned} \int_{\Omega_f} \Big(\partial_t(\rho \boldsymbol{u}) + \boldsymbol{\nabla \cdot} (\rho \boldsymbol{u} \otimes \boldsymbol{u}) \Big) \delta(\|\boldsymbol{x} - \boldsymbol{y}\|)\ \mathrm{d}\boldsymbol{y} \\ = \partial_t(\varepsilon \rho \bar{\boldsymbol{u}}) + \boldsymbol{\nabla \cdot} (\varepsilon \rho \bar{\boldsymbol{u}} \otimes \bar{\boldsymbol{u}}) + \boldsymbol{\nabla \cdot} \boldsymbol{R}, \end{aligned} \tag{3.17}$$

where the residual stress tensor is

$$\boldsymbol{R} = \int_{\Omega_f} (\rho \tilde{\boldsymbol{u}} \otimes \tilde{\boldsymbol{u}})\, \delta(\|\boldsymbol{x} - \boldsymbol{y}\|)\ \mathrm{d}\boldsymbol{y}. \tag{3.18}$$

This term accounts for the unresolved stress contributions caused by the fluctuating velocity field. It is similar to the Reynolds stress tensor in the context of turbulence modelling.

Filtering the divergence of the stress tensor gives

$$\int_{\Omega_f} (\boldsymbol{\nabla \cdot} \boldsymbol{\sigma}) \delta(\|\boldsymbol{x} - \boldsymbol{y}\|)\ \mathrm{d}\boldsymbol{y} = \boldsymbol{\nabla \cdot} (\varepsilon \bar{\boldsymbol{\sigma}}) - \int_{\Gamma_s} (\boldsymbol{n} \cdot \boldsymbol{\sigma}) \delta(\|\boldsymbol{x} - \boldsymbol{y}\|)\ \mathrm{d}\boldsymbol{y}, \tag{3.19}$$

The stress tensor is split into a filtered part and a fluctuating part $\boldsymbol{\sigma} = \bar{\boldsymbol{\sigma}} + \tilde{\boldsymbol{\sigma}}$. The fluid-grain interaction force is then used to close the system. The macroscopic stress tensor can be approximated as

$$\int_{\Gamma_s} (\boldsymbol{n} \cdot \bar{\boldsymbol{\sigma}}) \delta(\|\boldsymbol{x} - \boldsymbol{y}\|) \, \mathrm{d}\boldsymbol{y} \approx \bar{\boldsymbol{\sigma}} \cdot \boldsymbol{\nabla} \varepsilon, \tag{3.20}$$

based on the divergence theorem and a change of variables, as well as the assumption that the filtered stress and its derivatives varies slowly over the particle scale. A constitutive relation is then required for the fluctuating stress contribution. The force exerted by the fluid on the solid phase is assumed to take the form:

$$\phi \boldsymbol{f} \approx \phi(\boldsymbol{f}_\mathrm{d} - \boldsymbol{\nabla} \bar{p}). \tag{3.21}$$

where $\boldsymbol{f}_\mathrm{d}$ is the drag force density encompassing both filtered and fluctuating viscous effects and only pressure fluctuations, and $\boldsymbol{\nabla} \bar{p}$ accounts for filtered pressure gradient.

By decomposing the stress tensor into pressure and viscous components, and using Equations (3.19), (3.20) and (3.21), the filtered divergence of the stress becomes:

$$\int_{\Omega_f} (\boldsymbol{\nabla} \cdot \boldsymbol{\sigma}) \delta(\|\boldsymbol{x} - \boldsymbol{y}\|) \, \mathrm{d}\boldsymbol{y} = \boldsymbol{\nabla} \cdot (\varepsilon \bar{\boldsymbol{\tau}} + \boldsymbol{R}_{\boldsymbol{\tau}}) - \varepsilon \boldsymbol{\nabla} p - \phi \boldsymbol{f}_\mathrm{d} \tag{3.22}$$

where $\boldsymbol{R}_{\boldsymbol{\tau}}$ is the residual stress tensor associated with the viscous term, (3.19).

Thus, the volume-averaged momentum equation is:

$$\partial_t (\rho \varepsilon \bar{\boldsymbol{u}}) + \boldsymbol{\nabla} \cdot (\varepsilon \rho \bar{\boldsymbol{u}} \otimes \bar{\boldsymbol{u}}) = -\varepsilon \boldsymbol{\nabla} \bar{p} + \boldsymbol{\nabla} \cdot (\varepsilon \bar{\boldsymbol{\tau}} + \boldsymbol{R}_{\boldsymbol{\tau}} - \boldsymbol{R}) - \phi \boldsymbol{f}_\mathrm{d} + \varepsilon \rho \boldsymbol{g}, \tag{3.23}$$

or equivalently,

$$\partial_t (\rho \varepsilon \bar{\boldsymbol{u}}) + \boldsymbol{\nabla} \cdot (\varepsilon \rho \bar{\boldsymbol{u}} \otimes \bar{\boldsymbol{u}}) = -\boldsymbol{\nabla} \bar{p} + \boldsymbol{\nabla} \cdot (\varepsilon \bar{\boldsymbol{\tau}} + \boldsymbol{R}_{\boldsymbol{\tau}} - \boldsymbol{R}) - \phi \boldsymbol{f} + \varepsilon \rho \boldsymbol{g}, \tag{3.24}$$

The first form of the momentum equation (3.23) is referred to as the *model A* and the second form (3.24) as the *model B* [51].

These two models are equivalent but they differ in the way that the fluid–grain interaction force is treated. In *model B*, the total fluid-grain interaction force is expressed directly in the momentum equation. From the implementation point of view, this ensures action–reaction forces between the fluid and solid phases. On the other hand, *model A* is the intuitive one as the drag force is directly expressed in the momentum equation to ensure the no-slip condition. However, careful consideration is required when expressing the viscous term and the pressure gradient. In practice, both models are equivalent as long

as the pressure gradient over the solid phase is exactly computed. The choice between the two is a matter of implementation preference.

As will be shown in the next section, computing a precise, non-filtered porosity for each particle enhances the solid-phase representation and enables arbitrary spatial resolution.

3.1.3 Closures

As a result of filtering the equations of motion for the fluid phase, sub-grid terms arise and require closure. The general problem consists of formulating expressions for those terms based on filtered quantities, applicable over a wide range of particle Stokes and Reynolds numbers from the dilute to the dense limit. These terms are:

Residual stress tensor This stress originates from the advection of velocity fluctuations, as described in Equations (3.18), and is analogous to the Reynolds stress tensor encountered in turbulent flows.

$$\boldsymbol{R} \triangleq \boldsymbol{\nabla} \cdot (\rho \tilde{\boldsymbol{u}} \otimes \tilde{\boldsymbol{u}}) \approx \eta_t (\boldsymbol{\nabla} \bar{\boldsymbol{u}} + \boldsymbol{\nabla} \bar{\boldsymbol{u}}^T) \tag{3.25}$$

In immersed granular flows, depending on the Stokes number and concentration of the particle phase, the dispersed particles may either enhance or suppress turbulence relative to the single-phase case [79]. Experimental and numerical studies have demonstrated that dilute particle suspensions within the fluid boundary layer tend to dampen turbulence generation, whereas larger particles can amplify Reynolds stresses [80]. In the case of dense suspensions, fluidisation is typically associated with two distinct sources of turbulence: small-scale velocity fluctuations arising from granular agitation, such as interparticle collisions and wake-induced instabilities, and mesoscale structures like particle clusters and bubbles. Consequently, conventional turbulence models are generally inadequate for capturing these effects [81]. In this thesis, the Reynolds numbers encountered remain relatively low; therefore, the contribution of turbulence to the momentum balance is considered negligible.

Filtered Viscous term Filtering the velocity gradient in the viscous terms introduces unclosed stress contributions, since the gradients of velocity fluctuations can lead to additional dissipation:

$$\varepsilon \bar{\boldsymbol{\tau}} + \boldsymbol{R}_{\boldsymbol{\tau}} \approx \eta_{\text{eff}} \left(\boldsymbol{\nabla} \bar{\boldsymbol{u}} + \boldsymbol{\nabla} \bar{\boldsymbol{u}}^T \right) \tag{3.26}$$

As the particles resist deformation, their internal stresses increase, resulting in a larger effective viscosity. Modelling this increase is challenging,

because the resistance to deformation is already implicitly represented by the fluid–grain interaction forces and the discrete grain representation. For dilute suspensions ($\phi < 0.1$), the effective viscosity of the mixture can be described using Einstein or Batchelor's law [82, 34]:

$$\eta_{\text{eff}} \approx \eta \left(1 + 2.5\phi + 7.6\phi^2\right), \tag{3.27}$$

as supported by studies such as [83, 84]. However, in dense regimes, particle–particle interactions and collisions become the dominant source of internal stress [18], and the effective viscosity of the suspension diverges: Once the regime becomes dense, particle collisions become the main source of internal stress [18] and the suspension's effective viscosity diverges. This effect can be modelled by Krieger-Dougherty law [35]:

$$\eta_{\text{eff}} = \eta \left(1 - \frac{\phi}{\phi_m}\right)^{-n} \tag{3.28}$$

where ϕ_m is the maximum packing fraction and n is a fitting parameter, typically set to 2.

This effect is captured directly by the discrete particle model and should not be duplicated in the fluid phase. For dense suspensions, neglecting any increase in effective viscosity in the fluid phase has been shown to still yield accurate results [85].

$$\varepsilon \bar{\boldsymbol{\tau}} \approx \eta \left(\boldsymbol{\nabla} \bar{\boldsymbol{u}} + \boldsymbol{\nabla} \bar{\boldsymbol{u}}^T\right) \tag{3.29}$$

$$\boldsymbol{R}_{\boldsymbol{\tau}} \approx \mathbf{0} \tag{3.30}$$

This approach is also adopted in this thesis, since the fluid–grain parameterisation interaction forces already incorporate the local effects of the particles.

Particle scale force As the no-slip boundary condition is not explicitly resolved, the particle scale force provides the missing link between the fluid and solid phases. It is designed to ensure that the fluid–grain interaction force is consistent with the no-slip condition and the momentum balance based on a constitutive relation.

The total fluid–grain interaction force includes the contributions from both viscous and pressure forces acting on the particle. The viscous contribution is assumed to be fully captured by the constitutive model.

In contrast, only the fluctuating component of the pressure gradient is included in the constitutive relation, while the filtered (mean) pressure gradient is incorporated directly into the fluid–particle interaction force, as defined in Equation (3.21). Among the possible fluid–grain forces, **solely the drag force** is considered in the parameterisation, and grain rotation is not taken into account. The drag force is modeled using Dallavalle's empirical correlation, combined with the Di Felice voidage correction which accounts for the influence of neighbouring particles [23, 24]. The drag force density over particles is given by:

$$\boldsymbol{f}_{\mathrm{d}} = \sum_p \gamma_p(\boldsymbol{u} - \mathbf{v}_p), \tag{3.31}$$

$$\gamma_p = \varepsilon^{-2.8}\left(0.77\sqrt{\varepsilon \mathrm{Re}_p} + 5.88\right)^2 \frac{\eta}{d_p^2} \tag{3.32}$$

where d_p is the grain diameter, $\mathrm{Re}_p = \rho d_p \|\boldsymbol{u} - \mathbf{v}_p\|/\eta$ is the particle Reynolds number and γ_p is the drag coefficient.

3.1.4 Summary

This section has presented the derivation of the VANS equations and their associated closure models. Let us recall the Navier-Stokes problem over the fluid domain Ω_f, Equation (3.1),

$$\begin{cases} \boldsymbol{\nabla} \cdot \boldsymbol{u} = 0, & \text{in } \Omega_f, \\ \partial_t(\rho \boldsymbol{u}) + \boldsymbol{\nabla} \cdot (\rho \boldsymbol{u} \otimes \boldsymbol{u}) = \boldsymbol{\nabla} \cdot \boldsymbol{\sigma} + \rho \boldsymbol{g}, & \text{in } \Omega_f, \\ \boldsymbol{u} = \boldsymbol{v}, & \text{on } \Gamma_s, \end{cases}$$

has been simplified into a volume-averaged problem over the total domain $\Omega = \Omega_f \cup \Omega_s$,

$$\begin{cases} \boldsymbol{\nabla} \cdot (\varepsilon \boldsymbol{u}) + \boldsymbol{\nabla} \cdot (\phi \boldsymbol{v}) = 0, \\ \partial_t (\rho \varepsilon \boldsymbol{u}) + \boldsymbol{\nabla} \cdot (\varepsilon \rho \boldsymbol{u} \otimes \boldsymbol{u}) = -\varepsilon \boldsymbol{\nabla} p + \boldsymbol{\nabla} \cdot (\varepsilon \boldsymbol{\tau}) - \phi \boldsymbol{f}_{\mathrm{d}} + \varepsilon \rho \boldsymbol{g}, \\ \\ \boldsymbol{f}_{\mathrm{d}} = \displaystyle\sum_p \gamma_p(\boldsymbol{u} - \mathbf{v}_p), \qquad \gamma_p = \varepsilon^{-2.8}\left(0.77\sqrt{\varepsilon \mathrm{Re}_p} + 5.88\right)^2 \frac{\eta}{d_p^2}, \end{cases} \tag{3.33}$$

where the filtered indicator $\bar{\boldsymbol{u}}$ has been omitted for clarity. The same will be true in the following sections.

The coupling between the fluid and solid phases is established through the fluid volume fraction ε and the solid volume fraction ϕ, as well as through

the fluid–grain interaction force $\phi \boldsymbol{f}$ and the averaged solid velocity $\phi \boldsymbol{v}$. The following sections present the discretisation of the Volume-Averaged Navier–Stokes (VANS) equations and their coupling with the Discrete Element Method (DEM) for the solid phase.

3.2 The Finite Element Method for Fluid–Grain Coupling

To solve the VANS equations (3.33), the Finite Element Method is used. The fluid fields, the fluid velocity and the pressure, are discretised over finite space using shape functions τ. The choice has been made to use the continuous Galerkin method with linear shape functions for both the velocity and pressure fields. Let τ_i denote the shape functions associated to the i–th node, the discretisation of the velocity and pressure are thus given by

$$\boldsymbol{u}(\boldsymbol{x}, t) \approx \boldsymbol{u}^h(\boldsymbol{x}, t) = \sum_{i=1}^{N} \boldsymbol{u}_i(t)\tau_i(\boldsymbol{x}(t)), \tag{3.34}$$

$$p(\boldsymbol{x}, t) \approx p^h(\boldsymbol{x}, t) = \sum_{i=1}^{N} p_i(t)\tau_i(\boldsymbol{x}(t)), \tag{3.35}$$

where $\boldsymbol{u}^h$ and p^h are the discrete velocity and pressure fields, respectively, N is the number of nodes in the mesh, and $\boldsymbol{u}_i$ and p_i are the nodal values of the velocity and pressure fields.

Equal-order interpolation for velocity and pressure does not satisfy the inf–sup (Ladyzhenskaya–Babuška–Brezzi) condition, which can result in spurious pressure oscillations, numerical instability, and non-physical solutions. To address this issue, a Pressure-Stabilising Petrov–Galerkin (PSPG) formulation is employed [86, 87, 88]. Without this stabilisation, the weak form of the governing equations does not correspond to a minimisation problem, and the resulting linear system is not positive definite, leading to oscillations in the pressure field.

Additionally, continuous Galerkin methods are known to perform poorly for convection-dominated or hyperbolic problems, where standard discretisations may exhibit numerical dispersion and instability. To mitigate these issues, a Streamline-Upwind Petrov–Galerkin (SUPG) method is adopted [89], which introduces directional stabilisation aligned with the flow. This enhances robustness and accuracy in the presence of strong advection.

The introduction of the PSPG term leads to a violation of the divergence-free condition on the mixture velocity. To address this issue, an additional penalty term is added to the momentum equation in the form of a Least-Squares Incompressibility Constraint (LSIC), which reduces divergence errors and improves mass conservation.

The discrete form of the volume-averaged equations is to find $(\boldsymbol{u}^h, p^h) \in (\mathcal{U}^h \times \mathcal{P}^h)$ such that for all test functions $(\hat{\boldsymbol{u}}, \hat{p}) \in (\hat{\mathcal{U}}^h \times \hat{\mathcal{P}}^h)$,

$$\begin{aligned} 0 = &\int_V \left(\overbrace{\boldsymbol{\nabla} \cdot (\varepsilon \boldsymbol{u}^h + \phi \boldsymbol{v}^h)}^{\triangleq R_p(\boldsymbol{u}^h, p^h)} \right) \hat{p}^h \, \mathrm{d}V \\ &+ \sum_e \xi_p \int_{V_e} \boldsymbol{R}_u(\boldsymbol{u}^h, p^h) \cdot \boldsymbol{\nabla} \hat{p}^h \, \mathrm{d}V, \end{aligned} \tag{3.36}$$

$$\begin{aligned} 0 = &\int_V \left(\overbrace{\partial_t(\varepsilon \rho \boldsymbol{u}^h) + \boldsymbol{\nabla} \cdot \left(\varepsilon \rho \boldsymbol{u}^h \otimes \boldsymbol{u}^h\right) + \boldsymbol{\nabla} p^h - \varepsilon \rho \boldsymbol{g} + \phi \boldsymbol{f}^h}^{\triangleq \boldsymbol{R}_u(\boldsymbol{u}^h, p^h)} \right) \cdot \hat{\boldsymbol{u}}^h \, \mathrm{d}V \\ &- \int_V \boldsymbol{\nabla} \cdot \left(\varepsilon \boldsymbol{\tau}^h\right) \cdot \hat{\boldsymbol{u}}^h \, \mathrm{d}V, \\ &- \sum_e \xi_s \int_{V_e} \boldsymbol{R}_u(\boldsymbol{u}^h, p^h) \cdot (\boldsymbol{u}^h \cdot \boldsymbol{\nabla} \hat{u}^h) \, \mathrm{d}V \\ &- \sum_e \xi_c \int_{V_e} \boldsymbol{R}_p(\boldsymbol{u}^h, p^h) \cdot (\boldsymbol{\nabla} \cdot \hat{u}^h) \, \mathrm{d}V \end{aligned} \tag{3.37}$$

where e denotes the element index, V_e is the volume of element e, $\boldsymbol{R}_u(\boldsymbol{u}^h, p^h)$ is the residual of the momentum equation, ξ_p is the PSPG stabilisation parameter, ξ_s is the SUPG stabilisation parameter and ξ_c is the LSIC stabilisation parameter defined as [90]

$$\xi_p = \xi_u = \left[\left(\frac{2}{\Delta t} \right)^2 + \left(\frac{\left\| \boldsymbol{u}^h \right\|}{h} \right)^2 + \left(\frac{4\eta}{\rho h^2} \right)^2 \right]^{-\frac{1}{2}}, \tag{3.38}$$

$$\xi_c = h \left\| \boldsymbol{u}^h \right\| \min \left(\frac{h \rho \left\| \boldsymbol{u}^h \right\|}{6\eta}, \frac{1}{2} \right). \tag{3.39}$$

where h is the characteristic element size and Δt is the time step. Note that the viscous term is excluded from the residual $\boldsymbol{R}_u$ since its contribution vanishes for linear shape functions. For clarity, the superscript h denoting discretised fields will be omitted for the rest of the text.

The following sections address the coupling between the fluid and solid phases and detail the time integration scheme used in the simulation framework.

3.2.1 Fluid-grains Spatial coupling

As grains are not resolved by the mesh, a coupling strategy is required to incorporate their influence into the Volume-Averaged Navier–Stokes (VANS) equations. The interaction between the grains and the fluid is captured by three terms: the porosity ε (or equivalently, the solid volume fraction $\phi = 1 - \varepsilon$), the solid flux $\nabla \cdot (\phi \boldsymbol{v}_p)$, and the fluid–grain interaction force $\phi \boldsymbol{f}^h$.

Porosity ε represents the fraction of fluid volume within the domain and is used to ensure volume conservation. The grain velocity $\phi \boldsymbol{v}$ is the averaged velocity of the grains in the local fluid domain and contributes to enforcing mixture incompressibility. Finally, the interaction force $\boldsymbol{f}$ accounts for the momentum exchange between the fluid and the grains, ensuring that Newton's third law is satisfied.

Since the fluid phase is discretised using the Finite Element Method, an L_2 projection is a natural choice for coupling the fluid and solid phases. This projection leads to the following discrete coupling equations:

$$\int_V \phi \quad \tau \, \mathrm{d}V = \sum_p \int_{V_p} \qquad \tau \, \mathrm{d}V_p, \tag{3.40}$$

$$\int_V \phi \boldsymbol{v} \cdot \nabla \tau \, \mathrm{d}V = \sum_p \int_{V_p} \mathbf{v}_p \cdot \nabla \tau \, \mathrm{d}V_p, \tag{3.41}$$

$$\int_V \phi \boldsymbol{f} \quad \tau \, \mathrm{d}V = \sum_p \int_{V_p} \qquad \mathbf{f}_p \, \tau \, \mathrm{d}V_p, \tag{3.42}$$

where V is the fluid domain, V_p is the volume of the p-th grain, and τ denotes the finite element test function. The L_2 projection can lead to overshoots and undershoots in the solid volume fraction field. To avoid such issues, the mass matrix is mass-lumped in Equation (3.40) [91],

$$\phi_i \int_V \tau_i \, \mathrm{d}V = \sum_p \int_{V_p} \tau \, \mathrm{d}V_p, \tag{3.43}$$

where ϕ_i is the mass lumped solid volume fraction at node i.

A key challenge in coupling unresolved grains with the fluid phase is accurately computing integrals over the grain volume V_p. Without proper care, instabilities may arise, primarily from the continuity equation (3.14), due to the rapid variation of porosity. This issue is further exacerbated by the fact that porosity is typically represented as a linear field, whereas the velocity divergence remains constant within each element, leading to inconsistencies. Moreover, as particles cross element boundaries, discontinuities in the pressure gradient can occur. For these reasons, it is usually advised that the particle diameter should be at least three times smaller than the mesh size in order to ensure numerical stability.

A comprehensive review of void fraction estimation techniques is provided in [92]. The most straightforward method is the *Particle Centroid Method* (PCM), where the integrand is evaluated at the centroid of each grain. For example, the compacity and force will computed as:

$$\int_V \phi\tau \,\mathrm{d}V \approx \sum_p V_p \tau(\boldsymbol{x}_p), \tag{3.44}$$

$$\int_V \phi \boldsymbol{f}^h \tau \,\mathrm{d}V \approx \sum_p V_p \mathbf{f}_p(\boldsymbol{x}_p)\tau(\boldsymbol{x}_p). \tag{3.45}$$

While simple to implement, PCM can yield inaccurate results, especially when grains span multiple elements.

A more accurate alternative is the *Satellite Point Method*, which models each grain as a set of sub-grains of equal volume and applies PCM to each one. While this improves accuracy, the method still inherits the fundamental limitations of PCM. Figure 3.4 illustrates the PCM strategy.

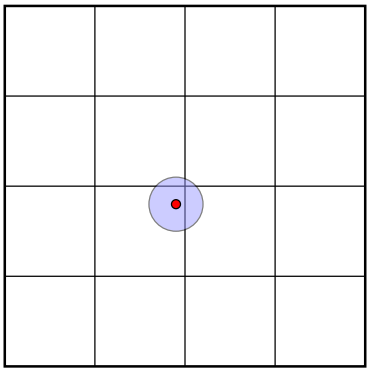

Figure 3.4: Particle Centroid Method (PCM) for estimating the solid volume fraction. The grain is represented as a single point, and the porosity is computed at the centroid of the grain.

To overcome these issues, Capecelatro et al. [49] proposed evaluating integrals at particle centroids and subsequently diffusing the results across the fluid mesh. While such smoothing enhances numerical stability, it introduces artificial diffusion that degrades accuracy in regions where sharp interfaces are critical. To address the limitations imposed by the particle–mesh size ratio and achieve semi-resolved simulations, Wang et al. [52, 93] proposed using an SPH-like kernel to distribute grain properties smoothly over the fluid mesh, effectively bridging the gap between unresolved and resolved scales. Figure 3.5 illustrates this strategy. More recently, Blais et al. [53] introduced a quadrature-based integration scheme that evaluates particle contributions using an SPH-like kernel directly at each fluid integration point. In this approach, the kernel

inherently provides smoothing, removing the need for an additional diffusion step.

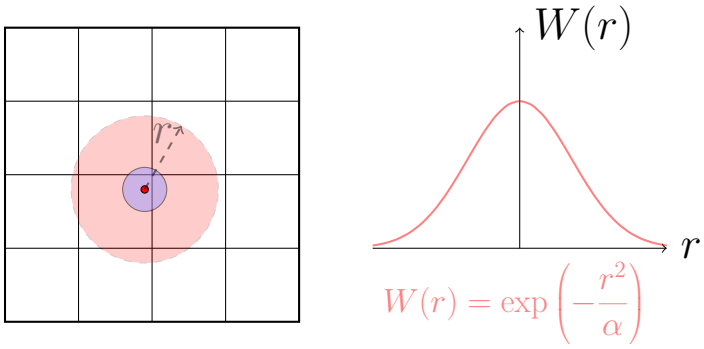

Figure 3.5: Gaussian Kernel-based method for estimating the solid volume fraction. The grain is distributed across the elements using a Gaussian kernel.

Previously, MigFlow was using the Particle Centroid Method (PCM) to compute the solid volume fraction with a mass-lumped approach, the fluid–grain interaction force was computed only at the grain centroid with a semi-implicit scheme and the continuity equation was used instead of the mixture volume conservation. This choice leads to instabilities in the pressure field in particle deposition simulations and a constraint on the mesh size. To smooth out these instabilities, an artificial pressure diffusion terms was introduced in the momentum equation, which is not physically justified and can lead to unphysical results. A predictor–correction time integration scheme was also implemented but only delay the instabilities without removing them. Those limitations have motivated the development of a new coupling strategy. To overcome the mesh size limitation, we employ an ad-hoc integration scheme to exactly integrate over the intersection between each grain and the underlying fluid elements. Stability is ensured using a semi-implicit time integration scheme in the mixture volume conservation equation (3.16).

Each grain is divided into sub-elements, which are defined by their intersection with the surrounding fluid mesh. The centroid of each sub-element is determined by iterating over the edges of the overlapping element. For each edge, a triangle is constructed using the edge and the grain's centre of mass. The exact intersection between this triangle and the circular grain is computed, and the centroid of the resulting shape, which comprises triangular and circular segments, is evaluated.

These centroids are then used to compute the integrals over each sub-element, yielding a more accurate and stable coupling strategy. Figure 3.6 illustrates this integration procedure.

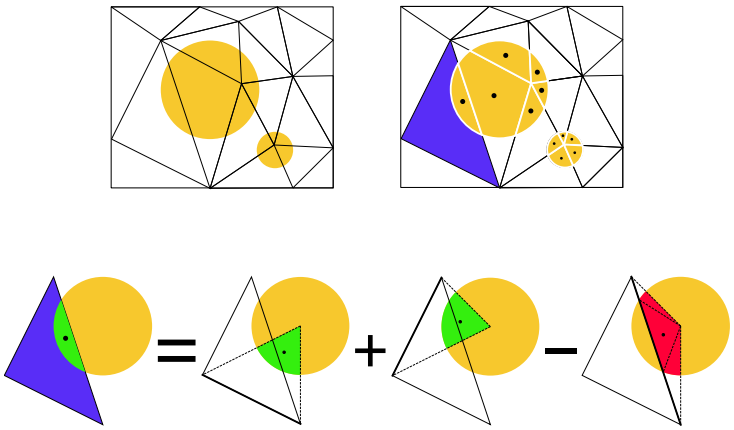

Figure 3.6: Disc integration rule over the fluid domain. The disc is divided into sub-elements defined by the overlap with each element of the mesh. The centroid of each sub-element is computed by iterating over the element edges. The black dot indicates the computed centroid.

As shown in Figure 3.7, this overlap-wise grain representation provides a natural framework for distributing grain properties across the fluid mesh. When a particle spans multiple elements, the interaction force is not concentrated at its centre of mass but is instead distributed over all intersected elements. This spatial distribution mitigates discontinuities in the fluid–grain interaction force as particles enter or exit elements. A key advantage of this approach is its ability to exactly integrate linear fields over the grain–element intersections. This ensures that the computed void fraction is both accurate and physically consistent, remaining positive and bounded by unity due to the use of mass lumping. Note that grains are assumed not to overlap which is only valid as the Non-Smooth Contact Dynamics (NSCD) method is employed.

Combined with a semi-implicit time integration scheme, this spatial representation enables a stable and accurate coupling between the fluid and solid phases across arbitrary mesh resolutions, without requiring any additional smoothing or diffusion procedures.

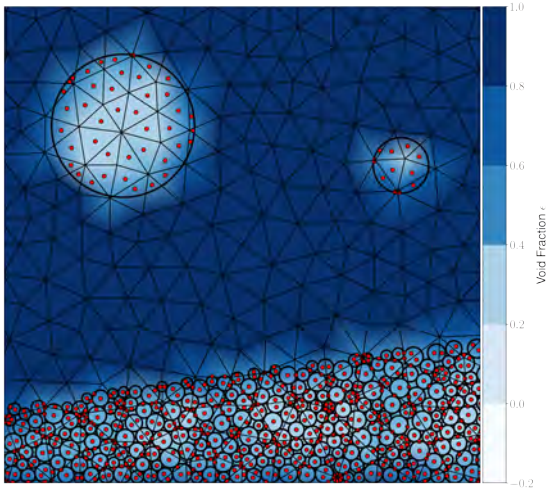

Figure 3.7: Illustration of the fluid-grains coupling. Grains are represented as a continuous field using an L_2 projection. The integral over the disc is approximated by the sum of the integrals over the elements containing the grain. The red dot represents the centroid of each overlapped sub-element. The void fraction is indicated by the colour map.

3.2.2 A semi-implicit temporal scheme

Since the fluid–grain interaction force acts as a source term in the momentum equation, its potentially large magnitude can strongly influence the stability of the numerical scheme. To ensure robustness, a semi-implicit scheme is adopted for computing the fluid–grain interaction force. For clarity, the grain index p is omitted in the following derivation.

The force is linearised, and an implicit prediction of the grain velocity at the integration point is made over the time step Δt, based on the grain dynamics described in Equation (2.5):

$$m\left(\mathbf{v}^{*}-\mathbf{v}^{n}\right)=m\boldsymbol{g}\Delta t+\mathbf{p}^{n}+V\Delta t\Bigg(\underbrace{-\nabla p^{n+1}+\gamma^{n}(\mathbf{u}^{n+1}-\mathbf{v}^{*})}_{\triangleq\mathbf{f}_{p}^{*}}\Bigg), \tag{3.46}$$

where superscript 'n' denotes explicit quantities, '$n+1$' denotes implicit quantities, and '$*$' denotes predicted values. The volume V corresponds to the particle volume. As contact forces are not yet been resolved, the contact impulse $\mathbf{p}^{n}$ from the previous time step is used.

Solving for the predicted grain velocity yields:

$$\mathbf{v}^* = \frac{1}{m+\gamma^n \Delta t}\Bigg(\underbrace{m\mathbf{v}^n + m\boldsymbol{g}\Delta t + \mathbf{p}^n - V\Delta t \nabla p^{n+1}}_{\triangleq m\mathbf{v}^{**}} + V\Delta t \gamma^n \mathbf{u}^{n+1} \Bigg), \quad (3.47)$$

$$= \frac{1}{m+\gamma^n \Delta t}\left(m\mathbf{v}^{**} + V\Delta t \gamma^n \mathbf{u}^{n+1} \right). \quad (3.48)$$

The predicted velocity $\mathbf{v}^*$ is then used to compute the drag force acting on the fluid, as defined in Equation (3.31), and to project the grain mass flux in the continuity equation, Equation (3.41). The resulting drag force density is given by:

$$\boldsymbol{f}_{\mathrm{d}}^* = \gamma^n \left(\boldsymbol{u}^{n+1} - \mathbf{v}^* \right), \quad (3.49)$$

$$= \frac{\gamma^n}{1+\gamma^n \frac{\Delta t}{m}} \left(\boldsymbol{u}^{n+1} - \mathbf{v}^{**} \right). \quad (3.50)$$

This formulation ensures numerical stability by effectively reducing the drag coefficient by the factor $(1+\gamma^n \Delta t/m)$. Positivity is also guaranteed, meaning the drag force always remains dissipative, as expected for such a coupling term. Note that the choice of the time step Δt is crucial, as it directly influences the drag coefficient γ^n and the accuracy of the simulations if it is driven by this force. It is worth recalling that only the drag force has been considered in this work, no rotation or lift forces have been included in the fluid–grain interaction force.

The time integration of the VANS equations is therefore governed by the following system:

$$\begin{cases} \boldsymbol{\nabla} \cdot \left(\varepsilon \boldsymbol{u}^{n+1} \right) + \boldsymbol{\nabla} \cdot \left(\phi \boldsymbol{v}^* \right) = 0, \\ \rho\varepsilon \dfrac{\boldsymbol{u}^{n+1} - \boldsymbol{u}^n}{\Delta t} + \rho\varepsilon \boldsymbol{u}^n \cdot \nabla \boldsymbol{u}^{n+1} \\ \qquad = -\varepsilon \nabla p^{n+1} + \boldsymbol{\nabla} \cdot \left(\varepsilon \boldsymbol{\tau}^{n+1} \right) - \phi \boldsymbol{f}_{\mathrm{d}}^* + \varepsilon \rho \boldsymbol{g}, \end{cases} \quad (3.51)$$

Note that the implicit advected velocity term is advected explicitly to keep the problem linear, whereas the viscous term is treated implicitly in order to enhance stability. The time integration scheme is of first order.

As the mesh resolution increases, situations may arise in which fluid elements are completely covered by larger grains, resuling in near-zero void fraction $\varepsilon \to 0$. In such cases, the fluid acceleration, stress, and gravitational terms vanish in the momentum equation, leaving only the drag term. Even though the drag force can become unphysically large, it will impose the no-slip condition on the fluid phase. To prevent excessive, unphysical drag forces in such situations, a minimal void fraction threshold of $\varepsilon_{\min} = 10^{-8}$ is enforced. In this

case, the problem becomes similar to Volume Penalization methods (VPM) [94, 95] or Brinkman penalisation methods [96], where the fluid is forced to follow the solid phase. As the predicted velocity $\mathbf{v}^*$ is expressed in terms of pressure gradient, a pressure equation remains and the problem stays well-posed even in the limit of $\varepsilon \to 0$.

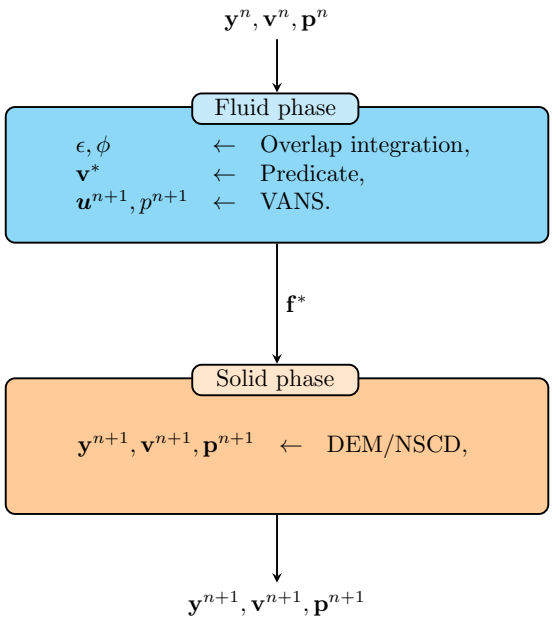

Figure 3.8: Semi-implicit coupling between the fluid and grain solvers.

The global coupling scheme is illustrated in Figure 3.8. The process begins with the computation of the solid and fluid volume fractions, based on the current particle positions, velocities, and contact impulses from the previous time step. Next, the semi-implicit prediction of the grain velocity is evaluated and used directly in the solution of the fluid governing equations. During this step, the fluid–grain interaction force is computed and transmitted to the grain solver. This force is applied explicitly and modifies the grain velocities. Subsequently, the Non-Smooth Contact Dynamics (NSCD) method is employed to resolve contacts and update the particle configuration, ensuring that there are no overlapping grains. The updated particle positions, velocities, and contact impulses are then stored for use in the next iteration.

A Model Comparison In order to compare the overlap-wise grain representation with the traditional Particle-Centroid Method (PCM), we simulate a simple sedimentation test under gravity. An initial deposit of monodisperse

grains is generated using a hexagonal packing arrangement. The grain radius is $r = 1.5$ mm, and the computational domain measures 0.4×0.6 m. The mesh resolution is coarser than the grain scale, with a mesh-to-grain diameter ratio of $h/d = 3$. The fluid is initially at rest, and the grains are released from the top of the domain. The fluid density is $\rho = 1000$ kg/m^3 with a dynamic viscosity of 0.001 Pa·s, while the particle density is $\rho_p = 1500$ kg/m^3 and gravity is set to $g = 9.81$ m/s^2. Figure 3.9 presents snapshots of the grain deposit and the fluid mesh at times $t = 0.0$ s, $t = 0.5$ s, and $t = 1.0$ s, for both models. In simulations using the PCM, an artificial pressure diffusion term must be introduced to stabilise the solution. This term effectively increases fluid compressibility, reducing its resistance to the motion of falling grains. As a result, a large void forms at the top of the domain as grains fall. In contrast, the overlap-wise grain representation provides a more accurate description of the fluid–grain interaction force. This improved coupling leads to a more stable and physically realistic simulation without requiring additional stabilisation. The mixture remains incompressible, and only the leading edge of the granular front moves, while the grains behind remain closely packed and stationary. It is worth recalling that the overlap-wise grain representation does not impact the computational cost of the simulation as the linear solver and the contact resolution are the main bottlenecks of the simulation. Still, in both cases, granular instabilities and finger formation are observed.

Spatial Convergence To evaluate the spatial convergence of the numerical model, we simulate the fall of two grain-based droplets interacting within a viscous fluid. The setup is inspired by the numerical experiment of [55].

Each droplet is modeled as a disc of radius 3.3 mm, uniformly composed of grains with radius 25 μm and density 2450 kg/m^3. The grains are distributed so that the droplet reaches a compacity of 0.2. Both droplets are initially at rest and released from the top, separated by a vertical distance of 10 mm. The surrounding fluid has a density $\rho = 1030$ kg/m^3 and a dynamic viscosity $\eta = 0.6$ Pa·s. Gravity is set to $g = 9.81$ m/s^2. To reduce computational cost far from the droplets, an adaptive mesh is employed.

During the fall, an overpressure develops at the front of each droplet, while a low-pressure region forms at the rear as the fluid is drawn in. As a result, the upper droplet descends faster than the lower one. When the droplets interact, they merge into a single, larger droplet. Because grains at the front experience stronger drag forces than those at the rear, they decelerate more strongly, which induces the formation of convection cells within the droplet. A trail of satellite grains is left behind as the merged droplet continues to fall, creating a tail. Snapshots at different mesh resolutions, from the finest to the coarsest, are shown in Figure 3.10.

The terminal velocity of the droplet is measured for each mesh resolution, computed as the average vertical velocity of the grains. Figure 3.11 shows

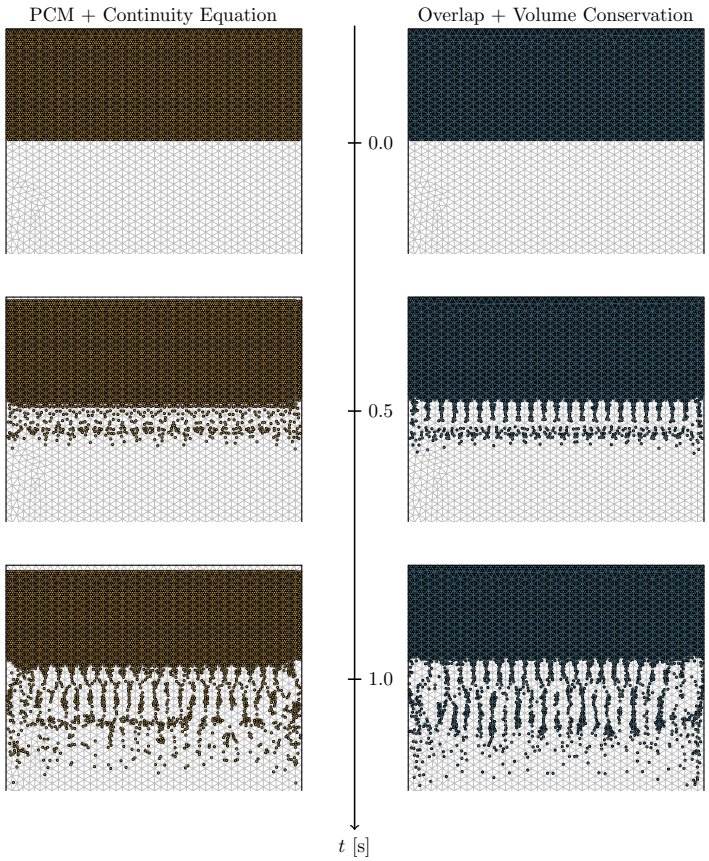

Figure 3.9: Snapshots of the sedimentation test. The left column shows results using the PCM model, while the right column uses the new overlap-wise grain representation. The fluid mesh is displayed in gray.

the convergence of the terminal velocity with mesh refinement. The results demonstrate convergence towards a stable value, with a rate of approximately $\mathcal{O}(h^{1.65})$. This confirms both the accuracy of the numerical model and its capability to capture the relevant physical phenomena at unresolved and semi-resolved scales. It is also worth to mention that the only artificial diffusion introduced in the model is the PSPG term.

3.2.3 A Two-Dimensional Approximation

The numerical model presented in this and subsequent chapters has been developed to simulate two-dimensional fluid–grain interactions, despite the in-

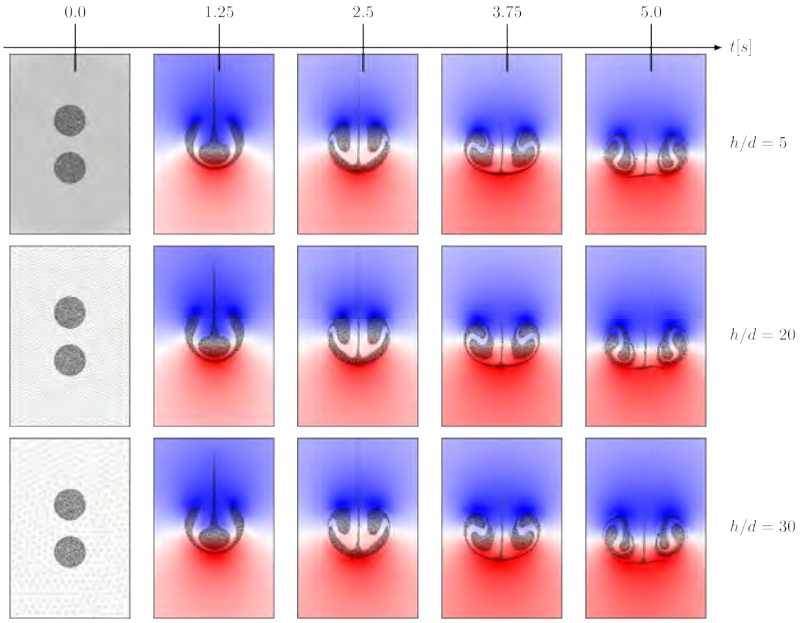

Figure 3.10: Snapshots of the fall of the grains droplet at different mesh resolutions. From top to bottom: the finest resolution, to the coarsest resolution. The colour field indicates the dynamic pressure.

herently three-dimensional nature of the underlying physics. While the model can be extended to three-dimensional cases, this would substantially increase the computational cost. Additionally, the implementation of the overlap decomposition method (see Section 3.2.1) currently supports only triangular elements and would need to be extended to tetrahedral elements for use in three-dimensional simulations.

When adopting a two-dimensional representation of a three-dimensional problem, it is assumed that all physical quantities are uniform along the out-of-plane direction. For example, spherical grains are modelled as infinite cylinders, the cross-section in the two-dimensional plane appears as discs. This simplification leads to an overestimation of the packing fraction, as it does not capture the ability of grains to settle on top of one another in the third dimension. Specifically, the random packing fraction for discs is approximately $\phi \approx 0.82$, compared to $\phi \approx 0.64$ for spheres. To correct for this discrepancy, the fluid solver assumes an effective grain diameter that is smaller than the actual diameter, ensuring that the simulated packing fraction is consistent with the three-dimensional case. From the perspective of grain dynamics, however, the original diameter is retained. Furthermore, grains are restricted to three de-

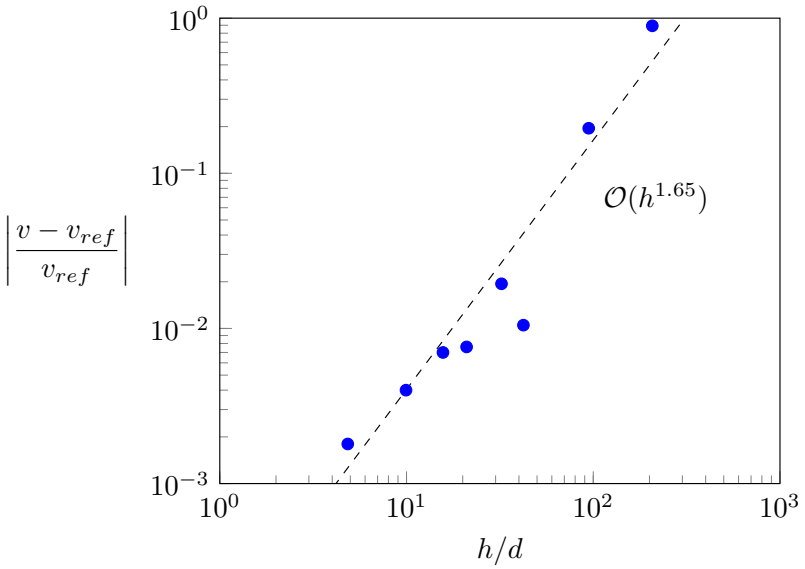

Figure 3.11: Convergence of the particles vertical velocity with respect to the mesh resolution.

grees of freedom, as opposed to six in a fully three-dimensional setting, which limits their mobility.

While the two-dimensional approximation offers significant computational efficiency, it inevitably results in a loss of accuracy compared to fully three-dimensional simulations. Consequently, although calibration can be performed to ensure that the two-dimensional model captures the essential physics of the problem, it is important to recognise that this approach does not provide quantitatively accurate results. This two-dimensional approximation will be used to simulate three-dimensional problems in Chapters 4–5.

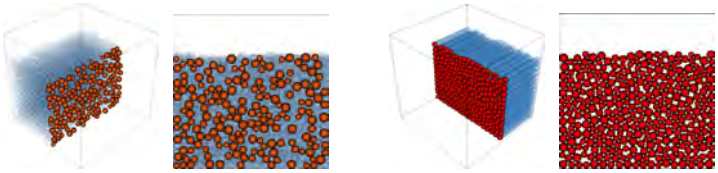

Sphere deposit. Cylinder deposit.

Figure 3.12: Comparison between a sphere deposit and a disc deposit. The left column shows the 3D sphere deposit, while the right column shows the 2D disc deposit.

3.3 One Model, Three Paradigms

In this section, we present four different applications to illustrate the versatility of the numerical model. Firstly, we present the simulation of a granular Rayleigh-Taylor instability at the edge between the unresolved and semi-resolved scale. Next, the fluidisation of a granular layer is simulated from unresolved to semi-resolved meshes. We show that the similar head pressure is obtained for the first movement and the total heave across all mesh sizes. Finally, to illustrate the accuracy in the resolved scale, we simulate the sedimentation of a 2D cylinder and the drafting–kissing–tumbling effect between two cylinders.

3.3.1 Granular Rayleigh-Taylor instability

When a dense granular packing is placed on top of a lighter fluid in a Hele-Shaw cell and released, the grains fall and form finger-like structures, a phenomenon known as the *granular Rayleigh–Taylor instability* [97]. As the grains descend, the fingers widen, and rising air bubbles begin to separate them. The classical Rayleigh–Taylor instability arises when a fluid is placed above a lighter one, leading to an instability at the interface [98]. As the heavier fluid falls, it initially forms a large finger that breaks up into smaller ones due to misalignment between the pressure and the density gradient at the interface, creating a chaotic pattern. In contrast, the granular Rayleigh–Taylor instability tends to limit the number of formed fingers which stabilise the structure size. New fingers emerge at the centre of rising bubbles once they reach a critical width, resulting in a characteristic pattern with a relatively stable structure size. Figure 3.13 illustrates the initial formation of fingers and the accompanying air bubbles. This setup is of particular interest to model the formation of bubble voids as it is the key mechanism in the evolution of fingers. Moreover, the significant density ratio between the grains and the fluid, exceeding a factor of 1000, combined with the incompressibility constraint of the fluid, makes this scenario a challenging test case for our numerical model.

The numerical setup follows the experimental and numerical work of Vinningland et al. [99]. The grains are modelled as discs with a diameter of $d = 230\,\mu$m and a density of $\rho_p = 1050\,\mathrm{kg/m^3}$. Friction is neglected in this case, and a slight polydispersity is introduced (polydispersity ratio $\lambda = 1.2$) to prevent crystallisation of the grains. The total number of grains is of 70000, and a uniform mesh with a mesh-to-grain diameter ratio of $h/d = 2$ is used, where h denotes the maximum edge length. The fluid is air, with a density of $\rho = 1.2\,\mathrm{kg/m^3}$ and a dynamic viscosity of $\eta = 1.82 \times 10^{-5}\,$Pa·s. The numerical domain is a rectangular box of height $H = 68\,$mm and width $W = 56\,$mm, smaller than the experimental Hele-Shaw cell, which measures $H = 141\,$mm in height and $W = 91\,$mm in width. The depth of the Hele-Shaw cell is 2.3 mm

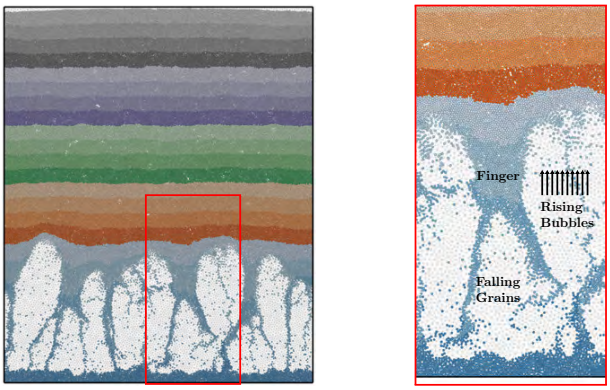

Figure 3.13: Rayleigh–Taylor instability at time $t = 0.1\,\mathrm{s}$. The fluid is initially at rest, and the grains are released from the top of the domain. As the grains fall, air bubbles rise and create finger-like structures.

which corresponds to ten times the grain diameter.

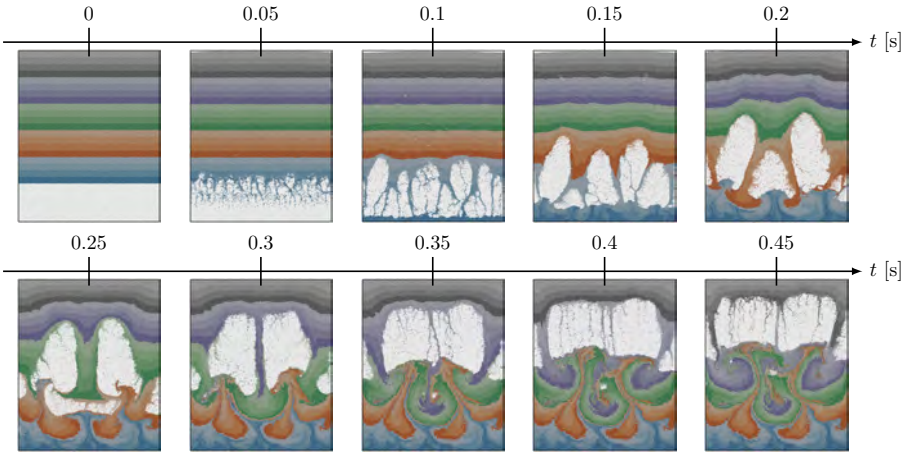

Figure 3.14: Snapshots of the Rayleigh–Taylor instability at times $t = \{0, 0.05, 0.1, \ldots, 0.45\}\,\mathrm{s}$. The colormap indicates the initial vertical coordinate of the grains.

Figure 3.14 shows snapshots of the evolution of the granular Rayleigh–Taylor instability over time. The colour map indicates the initial vertical coordinate of the grains, revealing how the granular structure deforms over time. Fingers form at the initial air–grain interface and grow as the grains fall. Air bubbles are trapped and rise between the fingers, progressively merging and

creating larger voids. The simulation runs for a total time of $t = 0.45\,\mathrm{s}$ with a time step of $\Delta t = 10^{-4}\,\mathrm{s}$. The computation took approximately four hours on a laptop equipped with an Intel Core i7 (10th generation) CPU and 16 GB of RAM. Notably, most of the computational time is spent in the contact solver, so increasing the fluid resolution has little impact on performance and is easily achievable. The simulation is performed using the new overlap-wise grain representation. The main physical phenomena are well-captured by the model. The following test cases will investigate the influence of mesh resolution on the macroscopic behaviour of the fluidised layer and the validity of the model at the resolved scale.

3.3.2 Fluidisation of a granular layer

To investigate the influence of mesh resolution on macroscopic behaviour, the experimental setup of Peng et al. [100] is numerically reproduced using different mesh sizes, illustrated at Figure 3.15. The finest resolution corresponds to a mesh-to-grain diameter ratio of $h/d = 0.5$, while the coarsest mesh has a ratio of $h/d = 8$, covering a range from semi-resolved to fully unresolved configurations. In this setup, a granular bed is subjected to a gradually increasing pressure at the bottom, inducing loosening of the soil. Figure 3.16 presents snapshots of the soil loosening process for the finest mesh case ($h/d = 0.5$). Two key quantities are measured: the differential head at the onset of grain movement and the total bed heave. The hydraulic head is defined as

$$\psi = y + \frac{p}{\rho g} + \frac{\|\boldsymbol{u}\|^2}{2g}, \tag{3.52}$$

where y is the vertical coordinate, p is the pressure, $\boldsymbol{u}$ is the fluid velocity, and g is the gravitational acceleration. The differential head is measured between the initial top and bottom of the granular layer.

The first movement is defined as the instant when grains begin to lift off, while total heave occurs when the entire bed is mobilised. Since these phenomena are not sharply defined physically, they are quantified based on grain motion. A grain is considered mobilised if it displaces more than its maximum diameter. The first movement is said to occur when at least 5% of the total grain mass is mobilised, and total heave is defined when this reaches 95%.

The granular bed consists of slightly polydisperse discs with a size span $\lambda = d_{\max}/d_{\min} = 1.2$, where the minimum diameter is set to $d_{\min} = 0.2$ mm. The particle density is $\rho_p = 2630\ \mathrm{kg/m^3}$, and the interparticle friction coefficient is 0.4. An initial deposit is generated by letting the particles settle under gravity within a rectangular domain.

The surrounding fluid is water, with a density of $\rho = 1000\ \mathrm{kg/m^3}$ and a dynamic viscosity of $\eta = 0.001\ \mathrm{Pa\,s}$. Solid, impermeable boundaries are imposed on the lateral walls. A back pressure of 103 kPa, consistent with

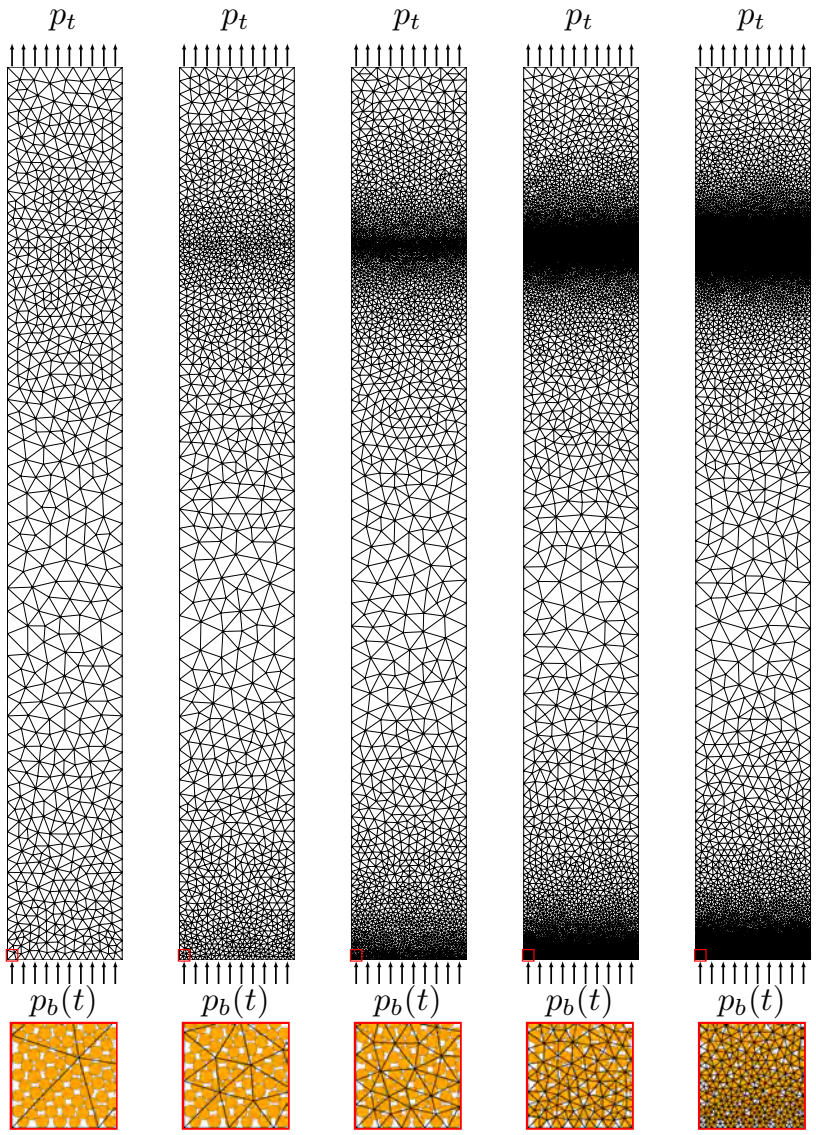

Figure 3.15: Meshes used for the simulation. The leftmost mesh refers to an unresolved case, $h/d = 8$, and the rightmost mesh refers to a semi-resolved case, $h/d = 0.5$.

the experimental conditions, is applied to the top boundary, while a linearly

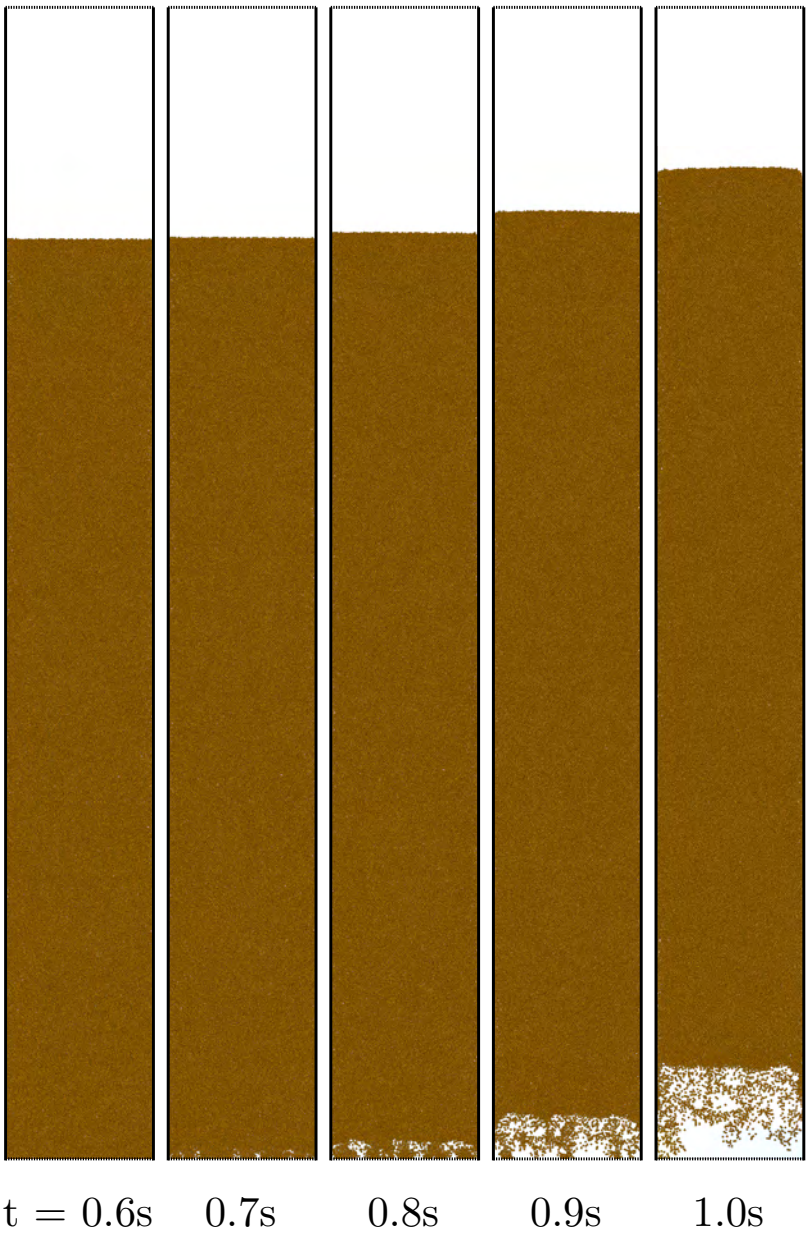

Figure 3.16: Snapshots of the soil loosening process for the finest mesh case ($h/d = 0.5$).

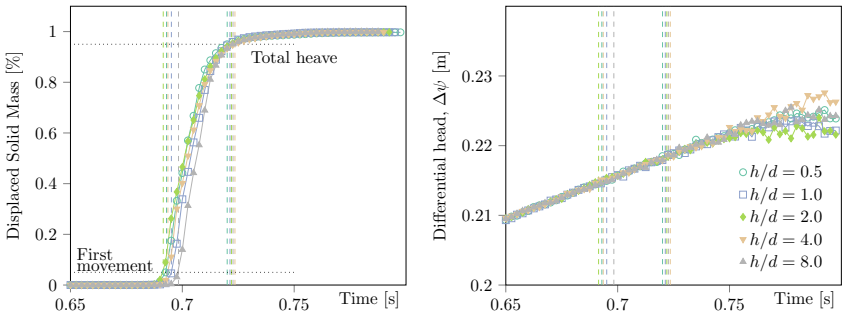

Figure 3.17: On the left, evolution of the solid mass fraction in motion for different mesh sizes. On the right, the differential head evolution for different mesh sizes.

increasing pressure is imposed on the bottom boundary such that

$$p_b(t) = p_0 + \rho g H \frac{t}{\Delta t}, \tag{3.53}$$

$$p_0 = p_t + \rho g H, \tag{3.54}$$

where p_b is the bottom pressure, p_0 is the initial bottom pressure, p_t is the top pressure, H is the height of the layer, and Δt is the time rate set to one second. As the bottom pressure increases, the differential head Δh increases and the particles start to move.

For each mesh considered, the instants at which the first movement and the total heave are detected are recorded. Figure 3.17 shows the evolution of the solid mass fraction in motion and the associated differential head. For each mesh size, the first movement is detected at $t \approx 0.69$s and the total heave is detected at $t \approx 0.72$s. The differential head for total heave is around 22 cm for all mesh sizes. This is a slight overestimation compared to the experimental data of 19 cm. This discrepancy can be attributed to the bi-dimensional nature of the simulation, as the geometrical constraints are more restrictive in a two-dimensional setup. Therefore, the pressure required to trigger a motion must be higher than in a three-dimensional setup. No significant difference is observed between the different mesh sizes, indicating that the model is robust and that the mesh size does not significantly affect the results as long as the mesh is sufficiently fine to resolve the macroscopic behaviour.

3.3.3 Sedimentation of a 2D cylinder

To validate the two-way fluid–solid coupling in the resolved case, we compare our results with the numerical data of Namkoong et al. [101], who investigated the motion of a rigid body falling in a viscous fluid.

Specifically, we consider the case of a two-dimensional rigid cylinder released from rest in a quiescent fluid under gravity. The cylinder has a diameter $D = 0.005\,\mathrm{m}$ and a density ratio $\rho_s/\rho_f = 1.01$, where ρ_s and $\rho_f = 996\,\mathrm{kg/m^3}$ are the densities of the solid and the fluid, respectively. The kinematic viscosity of the fluid is $\nu = 8 \times 10^{-7}\,\mathrm{m^2/s}$. The terminal velocity of the cylinder is expected to be $U_t = 2.501\mathrm{cm/s}$, corresponding to a terminal Reynolds number of approximately $\mathrm{Re} = 156$ [101]. The computational domain size is set to $[-0.02, 0.02] \times [-0.16, 0.16]\,\mathrm{m}$. The mesh size is described by the ratio $h/d = 15$, where h is the mesh size and d is the grain diameter. Figure 3.18 shows the mesh close to the cylinder at the initial conditions. Snapshots of the cylinder at different times with the vorticity field are shown in Figure 3.20.

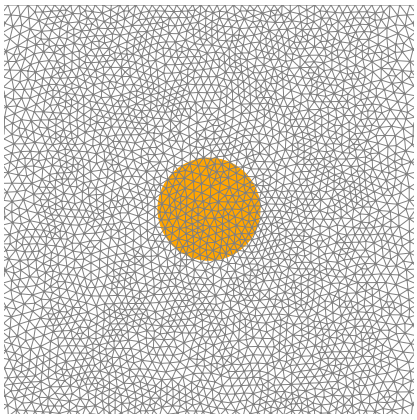

Figure 3.18: Mesh used for the simulation of a 2D cylinder falling in a fluid.

Figure 3.19 shows the time evolution of the normalised streamwise (u_{str}/U_t) and lateral (u_{lat}/U_t) velocity components of the falling cylinder, where U_t denotes the terminal velocity reported in the reference study [101]. The results obtained using the present method closely follow those of Namkoong et al., capturing the essential dynamics of the descent.

The streamwise velocity initially exceeds the terminal velocity, but is subsequently damped as vortex shedding becomes prominent. The lateral velocity component displays a similar oscillatory pattern, but with opposite signs. The direction of these oscillations depends on the initial conditions and numerical asymmetries, such as mesh-induced perturbations. Both the wavelength and frequency of these oscillations are consistent between the present simulation and the reference data.

Importantly, both the present simulation and the reference data exhibit the same oscillation frequency, suggesting that the two-way coupling between the fluid and solid phases has been accurately represented. These results confirm

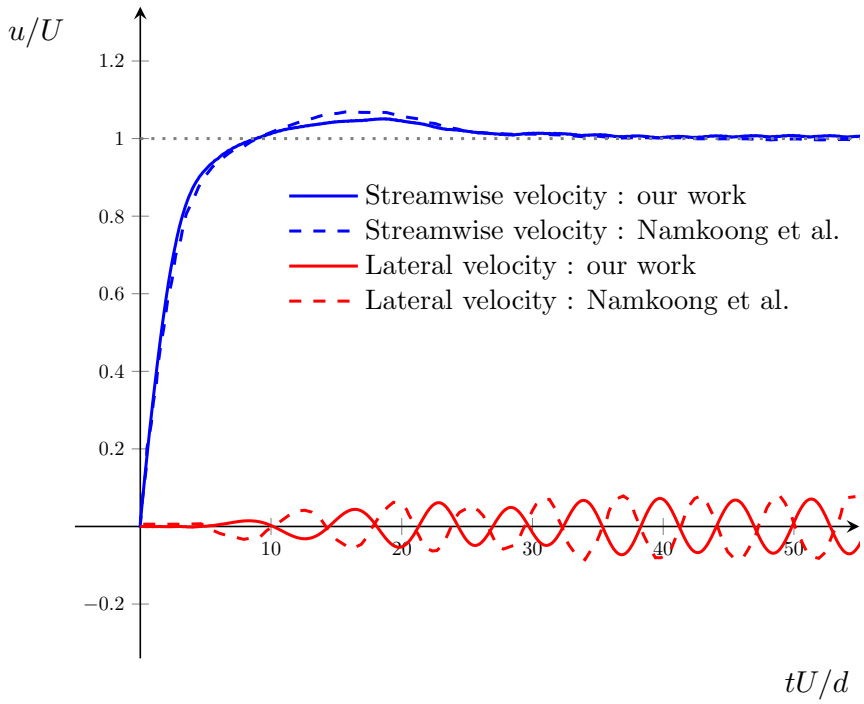

Figure 3.19: Velocity of a 2D cylinder falling in a fluid. The streamwise velocity is shown in blue and the lateral velocity in red. The solid lines are the results from the present model and the dashed lines are the results from Namkoong et al. [101].

that the implemented coupling scheme accurately captures the key physical features of the rigid-body descent in a viscous fluid.

3.3.4 Drafting-Kissing-Tumbling

The drafting–kissing–tumbling (DKT) phenomenon is a well-known behaviour observed during the sedimentation of two particles in a viscous fluid. This process consists of three distinct stages: *drafting*, *kissing*, and *tumbling*. During the drafting stage, the trailing particle enters the wake of the leading particle, experiencing a reduced drag force due to the lower pressure region in the wake. This causes the trailing particle to accelerate and approach the leading one. When the particles come into contact, the system enters the kissing stage, forming a transient elongated body aligned with the flow direction. This configuration is unstable and eventually results in the tumbling stage, where the pair rotates and separates. The DKT phenomenon has been widely investigated in the literature through numerical studies [102, 103, 104].

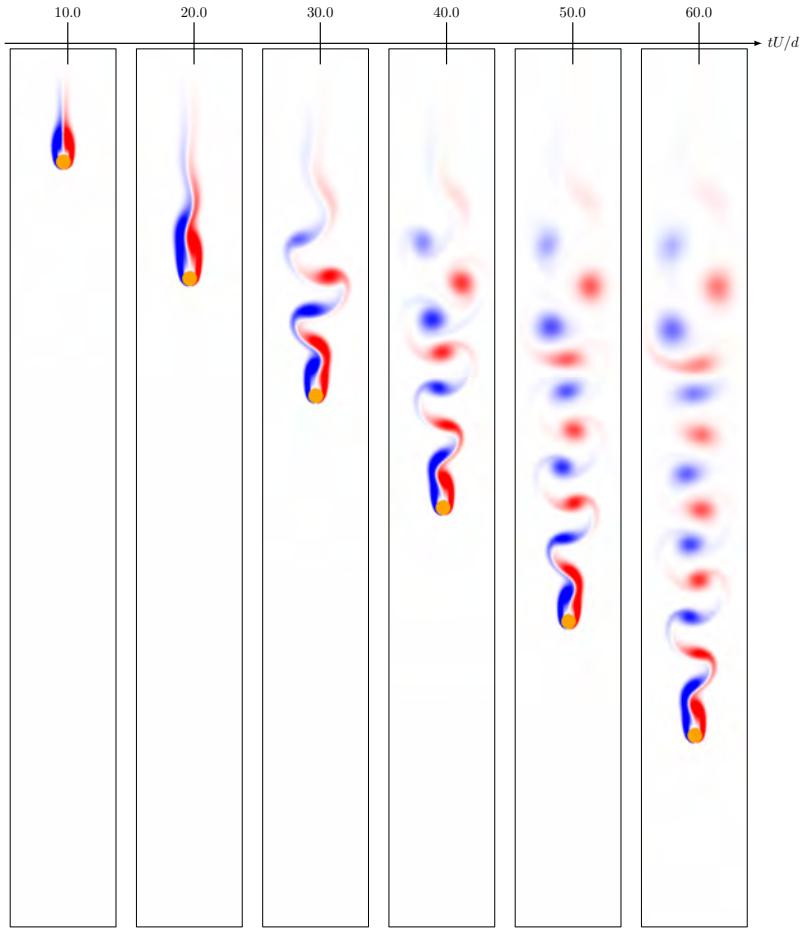

Figure 3.20: Snapshots of the cylinder at different times with the vorticity field.

In this work, we simulate the DKT behaviour of two rigid particles in a viscous fluid, following the reference study by Feng et al. [102]. Figure 3.21 shows the snapshots of the two particles at different times, along with the vorticity field. The first snapshot shows the two particles at rest and the mesh used for the simulation. The mesh size is set to a ratio of $h/d = 12.5$, where h is the mesh size and d is the particle diameter.

The computational domain is a rectangular channel of width $W = 2$ cm and height $H = 8$ cm. The fluid has a density of $\rho = 1$ g/cm^3 and dynamic viscosity $\eta = 0.01$ g/(cm·s). The particles have a density of $\rho_p = 1.01$ g/cm^3 and diameter $D = 0.2$ cm. Initially, both particles are placed on the channel

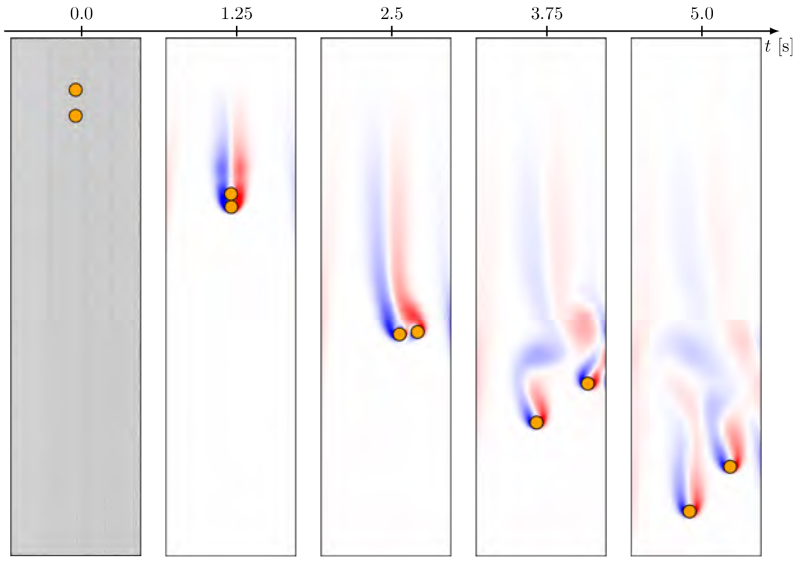

Figure 3.21: Snapshots of the cylinders at different times with the vorticity field.

centerline at vertical positions $y = 7.2$ cm and $y = 6.8$ cm, respectively. The fluid and particles are initially at rest at $t = 0$, and motion begins due to the gravitational force acting on the slightly denser particles.

The positions of the particles are tracked over time to analyse the evolution of the DKT phenomenon. Figure 3.22a displays the horizontal positions of the two particles as a function of time, while Figure 3.22b presents their vertical trajectories. To facilitate identification of the distinct stages of the DKT process, the relative positions of the particles are shown in Figure 3.23.

The horizontal separation D_x is defined as the difference between the horizontal coordinates of the particle centres, while the vertical separation D_y is the difference between their vertical positions. Additionally, the distance from the leading particle to the fluid surface is denoted as D_r, and is included for reference. Those plots collectively illustrate the progression from drafting to kissing and ultimately tumbling, characteristic of DKT behaviour.

The drafting–kissing–tumbling (DKT) behaviour is well captured by the present model, with the particles exhibiting a clear transition through the drafting, kissing, and tumbling stages. This demonstrates the model's capability to accurately resolve complex particle–fluid interactions at the microscale. However, this level of accuracy comes at the cost of increased computational demand, which is significantly higher compared to simulations using unresolved or semi-resolved approaches.

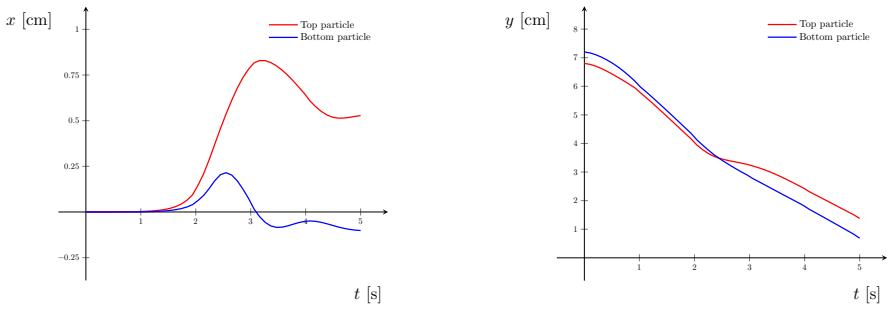

(a) (b)

Figure 3.22: Left (a): Evolution of the horizontal position of the particles over time. Right (b): Evolution of the vertical position of the particles over time. The red curve corresponds to the initially upper particle, while the blue curve represents the initially lower particle.

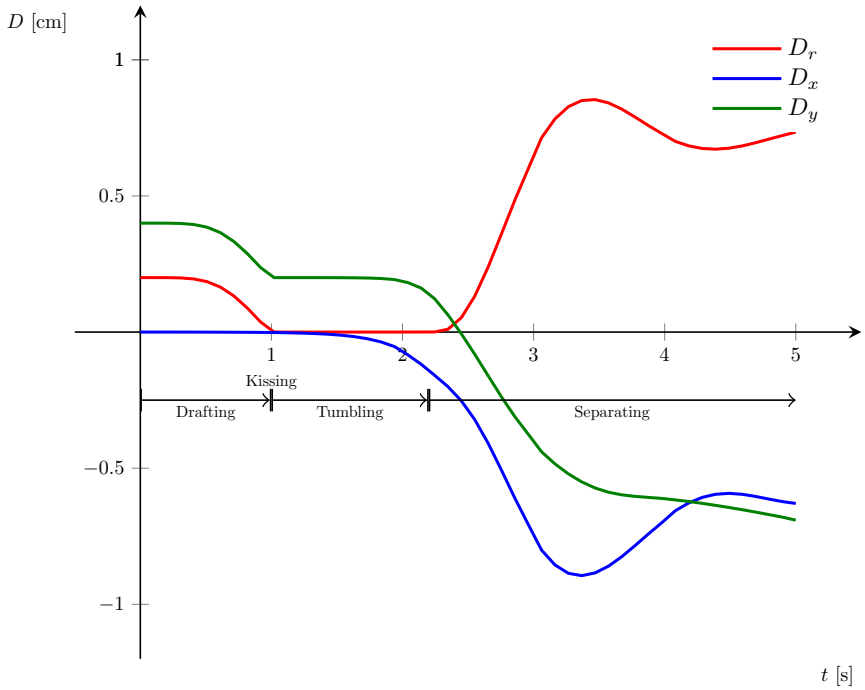

Figure 3.23: Evolution of the separation between the particles over time. The red curve corresponds to the surface-to-surface distance D_r, the blue curve represents the horizontal separation D_x, and the green curve shows the vertical separation D_y.

Conclusion

In this chapter, we present the final component of the simulation framework for fluid–grain interactions using a two-way coupling approach. The Volume-Averaged Navier–Stokes equations are coupled with a discrete representation of the grains. To improve accuracy and stability, a new spatial representation of the grains has been introduced. A semi-implicit time integration scheme is employed to ensure numerical stability even in cases where the grain size exceeds the mesh resolution.

This advancement opens the door to a wide range of applications, spanning unresolved, semi-resolved, and resolved discretisations. The new coupling approach has been validated against the previous PCM model, demonstrating improved numerical stability and accuracy in capturing fluid–grain interaction forces. Several numerical test cases illustrate the versatility of the framework, including simulations of a granular Rayleigh–Taylor instability, the fluidisation of a granular layer, the sedimentation of a 2D cylinder, and the drafting–kissing–tumbling dynamics between two cylinders. Still, it should be noted that the numerical scheme is still a first-order scheme.

Moreover, the improved coupling retrieves the flexibility of the finite element method, allowing simulations of complex geometries and flow conditions. This adaptability enables the framework to accommodate a broad spectrum of particle sizes and configurations, including challenging free-surface flows, as explored in Section 5.

CHAPTER 4

Modelling Heat Transfer in Particulate Flows

Modelling heat transfer in granular flows is crucial for optimising the performance and efficiency of systems such as fluidised bubbling beds [105], which are widely used in the chemical and energy industries. In these reactors, solid particles are suspended by an upward-flowing fluid, creating a highly dynamic environment in which heat exchange is governed by both conduction through particle contacts and convection via the interstitial fluid. A reliable thermal model is essential for designing, scaling up, and operating such particulate-based systems.

Emerging applications take advantage of the low thermal conductivity of granular materials to store excess energy. For example, in thermal energy storage systems, the granular bed is heated. When energy is needed, water can be injected through pipes embedded within the sand, extracting the stored heat in the form of steam.

On an industrial scale, circulating fluidised bed (CFB) boilers exploit the fluidisation mechanism. Heat is generated by combustion and efficiently transported through the bed by injecting fluid into the granular medium. Typically, two kinds of particles coexist: bed particles, e.g., sand or ash, and fuel particles, e.g., coal or biomass. Depending on the fluid injection velocity, various flow regimes are observed, including percolation, bubbling, turbulent fluidisation, fast fluidisation, and the pneumatic regime. Among these, the bubbling

and fast fluidisation regimes are most commonly employed in industrial applications [106]. In the bubbling regime, fluid is injected slightly above the minimum fluidisation velocity, leading to the formation of bubbles that transport particles in their wake. This results in a heterogeneous suspension, with a lower solid volume fraction near the bubbles and a denser packing elsewhere. In contrast, the fast fluidisation regime, achieved at higher velocities, involves particle recirculation throughout the bed, yielding a more uniform solid distribution. As the efficiency of heat and mass transfer is highly sensitive to the fluidisation regime, it is essential to accurately model heat transfer within the granular material to optimise reactor performance.

A recent experimental observation introduces an alternative droplet-driven fluidisation process [61]. When a droplet of water is released onto a hot granular bed, its behaviour depends on the bed temperature. Near the boiling point, the droplet collapses and spreads over the surface, transferring heat only to the uppermost grains over a short duration. At higher temperatures, the vapour expelled from the droplet is strong enough to suspend the droplet, preventing contact with the grains. This is the Leidenfrost effect [107, 108]. At intermediate temperatures, a hybrid regime emerges. The vapour flow beneath the droplet fluidises the granular bed locally, enabling the droplet to dig progressively into the material. In this regime, heat transfer is maximised, as the droplet interacts with deeper layers, and temperature gradients are sustained by grain recirculation.

Modelling the interaction between a liquid droplet and hot granular media presents significant challenges due to the complexity of thermal conduction across grain contacts, the nonlinear shape and behaviour of the droplet, and the phase change processes involved. Understanding both the Leidenfrost regime and the thermal response of the granular assembly requires accurate numerical methods.

In this study, we employ a Discrete Element Method (DEM) to model the solid phase and couple it with the fluid phase using volume-averaged equations [48]. The fluid mesh resolution can be adjusted to balance computational cost with accuracy. To enable coupling between the fluid and solid phases, closure relations are necessary to model interphase momentum and thermal exchange [55, 109]. Recent studies have applied such CFD-DEM approaches to investigate heat transfer in fluidised granular systems [110, 111]. While drag correlations in immersed granular flows are well established, heat transfer correlations remain an active area of research, with no unified framework currently available. Several models exist, including those by Ranz and Marshall [112], Kemp and Lyon [113], Wang et al. [93], and Li et al. [114], but further validation and comparison are needed to improve their predictive capability in dense granular flows.

In this chapter, we extend the multiscale model to include heat transfer mechanisms between the fluid and solid phases. The model incorporates both

conduction within the granular phase and convective heat transfer at the grain scale, with a convection term specifically accounting for thermal exchange between the fluid and individual grains. A heat transfer correlation valid for assemblies of spherical particles is employed and validated against experimental data [115, 116]. Additionally, the model is extended to study heat transfer during droplet–granular bed interactions, explicitly considering phase change due to vapourisation. We investigate the phenomenon of spontaneous droplet penetration into a two-dimensional granular bed, and identify the conditions under which digging occurs based on temperature and vapour generation. The content presented in this chapter is based on the following publication:

- **Henry, M.**, Coppin, N., Dorbolo, S., Legat, V., Lambrechts, J., (2025), *Multiscale FEM-DEM model for spontaneous droplet digging in a hot granular bed*. International Journal of Heat and Mass Transfer

Contents

4.1 Heat Transfer Mechanisms in Granular Flows

In this section, we focus on two primary mechanisms responsible for thermal transport in granular flows: contact conduction and convective heat transfer. Contact conduction occurs at points where particles come into direct contact, allowing heat to be transferred through their solid interfaces. This mode of transfer depends strongly on contact duration, material properties, and force chains within the granular assembly. Convective heat transfer, on the other hand, arises from the exchange of thermal energy between particles and the surrounding fluid, governed by flow dynamics and its local temperature. To simplify the modelling, we assume that the Biot number is low, implying that intra-particle temperature gradients are negligible and that each grain can be treated as thermally uniform. Moreover, radiative heat transfer is neglected, as the temperature ranges considered are moderate and do not significantly activate radiation mechanisms. Generation of heat due to kinetic energy dissipation is also neglected in this study. Such hypotheses are only valid as the convection and conduction are the main heat transfer mechanisms in the considered applications. The particle temperature evolution is thus described by

$$\rho c \frac{\mathrm{d}T_p}{\mathrm{d}t} = q^c + q \tag{4.1}$$

where c is the heat capacity, T the particle temperature, q^c is the heat density generated by conduction and q is the heat density generated by convection. For a comprehensive review of heat transfer in granular media, we refer to the work of [117]. Figure 4.1 illustrates conduction and convection mechanisms.

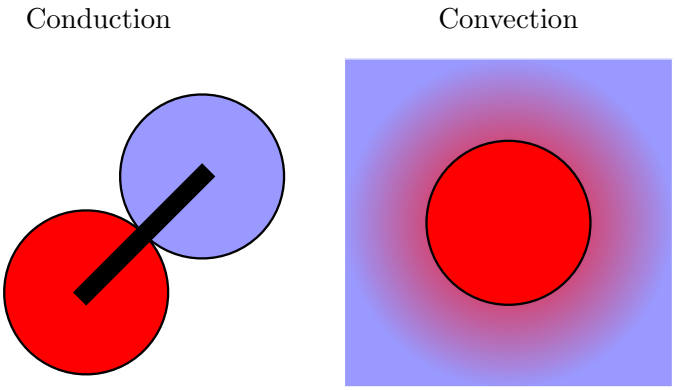

Figure 4.1: On the left, conduction occurs at the contact points between particles, while on the right, convection is driven by the fluid flow around the particles.

The following subsections present the theoretical foundations and modelling strategies for heat transfer in granular media. We begin by examining the fundamental mechanisms of conductive heat transfer at particle contacts, followed by an analysis of convective heat transfer driven by fluid–particle interactions. A volume-averaged framework is employed throughout to derive the governing heat transfer equations. To close the system, a constitutive relation for local fluid–particle heat exchange is introduced, based on the Colburn–Reynolds analogy.

4.1.1 Contact Conduction

Conduction between two particles originates from direct physical contact between their surfaces, through which thermal energy is transferred due to a temperature gradient. When two solid particles touch, heat flows through the microscopic contact area formed by surface roughness and deformation under load. The effectiveness of this heat transfer depends on the thermal conductivity of the grain material, the size and number of contact points, and the force pressing the particles together. Since real surfaces are rough, the actual contact area is much smaller than the apparent one, which can significantly limit conduction efficiency. As the non-smooth contact dynamics assume the contact area to be zero, an effective contact area for heat conduction is estimated based on the normal reaction force at the contact point assuming a Hertz contact model [118, 119]. Let us assume a contact between two grains i and j during a time step Δt. The associated impulse is denoted by $\mathbf{r}$ and the normal to the local basis is denoted by $\mathbf{n}$. The net contact conduction density acting on the grain i, denoted q_i^c and the contact conductance between two cylindrical grains i, j, denoted H_{ij} are obtained as [120, 12] :

$$q_i^c = \frac{1}{V_i} \sum_{j \in \mathcal{P}} H_{ij}(T_i - T_j), \qquad H_{ij} = 4k_s \left(\frac{r_n \; d^*}{2\pi L E^* \Delta t} \right)^{1/4} \tag{4.2}$$

where k_s is the harmonic mean of the solid heat conductivity, r_n is the normal contact impulse between the two grains i, j, L is the cylinder length, the effective Young's modulus E^*, the effective contact diameter d^* chosen as

$$\frac{1}{k_s} = 2\left(\frac{1}{k_i} + \frac{1}{k_j} \right), \qquad \frac{1}{E^*} = \frac{1-\nu_i^2}{E_i} + \frac{1-\nu_j^2}{E_j}, \qquad \frac{1}{d^*} = \frac{1}{d_i} + \frac{1}{d_j} \tag{4.3}$$

where ν_i is the Poisson's ratio associated with grain i. A boundary contact is assumed to behave like a particle with an infinite radius and an infinite Young's modulus. Figure 4.2 illustrates the heat transfer through the contact network of a granular assembly.

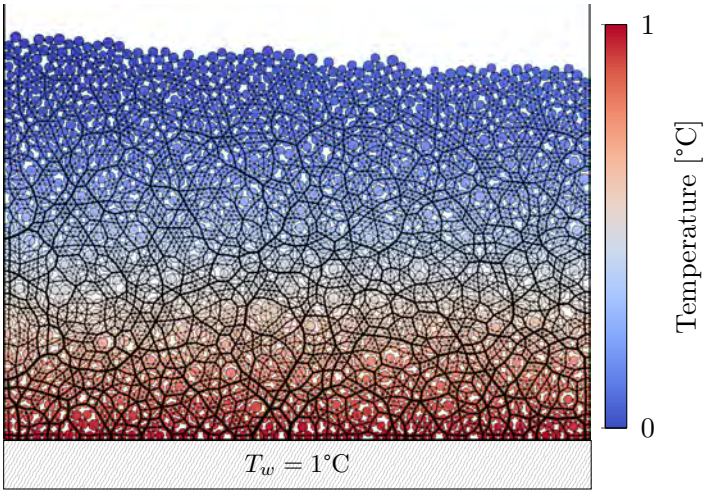

Figure 4.2: Heat transfer through the granular contact network. The lateral walls are adiabatic, while the bottom wall is maintained at a constant temperature. Grains are initially at a reference temperature of zero. Heat propagates through the particle contacts, leading to an increase in grain temperature over time.

4.1.2 Convection within a fluid

Convection occurs in granular flows when heat is exchanged at the interface between the particles and the surrounding fluid. This process is driven by temperature differences. As the fluid moves around and between the particles, it carries thermal energy away from hotter regions and transfers it to cooler ones. The rate of convective heat transfer depends on the relative velocity between the particles and the fluid, the fluid's thermal properties, and the surface area of the particles. This process is typically modelled using heat transfer coefficients, which can be estimated from empirical correlations such as the Colburn–Reynolds analogy.

In the context of multi-scale modelling, the fluid phase is not resolved at the particle scale. Therefore, the heat transfer at this scale can only be modelled through a constitutive law, as it is with momentum transfer through drag. To derive the heat transfer equation in its volume-averaged form, the same approach as for the momentum transfer is used [48, 121] under the Boussinesq's approximation, leading to the following conservation equations:

Volume & Momentum Conservation

$$\boldsymbol{\nabla} \cdot (\varepsilon \boldsymbol{u}) + \boldsymbol{\nabla} \cdot (\phi \boldsymbol{v}) = 0,$$
$$\partial_t (\rho \varepsilon \boldsymbol{u}) + \boldsymbol{\nabla} \cdot (\varepsilon \rho \boldsymbol{u} \otimes \boldsymbol{u}) = -\varepsilon \boldsymbol{\nabla} p + \boldsymbol{\nabla} \cdot (\varepsilon \boldsymbol{\tau}) - \phi \boldsymbol{f}_{\mathrm{d}} + \varepsilon \rho \boldsymbol{g}(1 - \beta(T - T_R)),$$

where β is the fluid thermal expansion coefficient, T is the fluid temperature, T_R is a reference temperature.

Heat Equation

$$\partial_t(\varepsilon\rho cT) + \boldsymbol{\nabla}\cdot(\varepsilon\rho c\boldsymbol{u}T) = -\boldsymbol{\nabla}\cdot\boldsymbol{q} - \phi q \tag{4.4}$$

where c is the heat capacity, $\boldsymbol{q}$ is the heat dissipative flux density and q is the heat transfer density between the fluid and the particles. The heat dissipative flux density is described by the modified Fourier's law,

$$\boldsymbol{q} = -\varepsilon k\boldsymbol{\nabla}T. \tag{4.5}$$

where k is the fluid thermal conductivity.

In order to close the system, a constitutive law for the heat transfer density q is required. The similarity between the momentum and heat transfer mechanisms is exploited to derive a correlation for the Nusselt number, which characterises the convective heat transfer. The drag force is modelled using the drag coefficient, which is a dimensionless number that quantifies its intensity. These dimensionless numbers are defined as

$$\mathrm{C_d} = \frac{f_\mathrm{d}}{\frac{1}{2}\rho\|\mathbf{v}-\boldsymbol{u}\|^2}\frac{V}{A}, \qquad \mathrm{Nu} = \frac{q\,d}{k(T-T_p)}\frac{V}{S}, \tag{4.6}$$

where V is the volume of the grain, A is its cross-sectional area, S is its surface area, d is its characteristic length usually the diameter of the sphere or disc, k is the fluid conductivity, T_p is the particle temperature and T is the fluid temperature. Momentum and heat transfer occur in their respective boundary layers. The ratio of thicknesses of the momentum and thermal boundary layers is described by the Prandtl number Pr. The thickness of the boundary layer is described by the Reynolds number Re. These two dimensionless numbers are defined as

$$\mathrm{Re} = \frac{\rho d\|\mathbf{v}-\boldsymbol{u}\|}{\eta}, \qquad \mathrm{Pr} = \frac{c_p\eta}{k}. \tag{4.7}$$

where η is the dynamic viscosity of the fluid, c_p its heat capacity and ρ its density. In the boundary layer, both mechanisms are driven by the same dissipation process. In turbulent flows, both heat and momentum transfer are carried by the same eddies. This observation leads to the concept of the Reynolds–Colburn analogy, which states that the Nusselt number is proportional to the drag coefficient,

$$\mathrm{Nu} \propto \mathrm{C_f}\,\mathrm{Re}\,\mathrm{Pr}^{\alpha}. \tag{4.8}$$

where $\mathrm{C_f}$ is the skin friction coefficient, which accounts solely for viscous stress, while the drag coefficient encompasses both viscous stress and pressure contributions. This analogy does not strictly hold across all flow regimes, since the thermal boundary layer also depends on the momentum boundary layer. However, it offers a useful starting point for adjusting heat transfer correlations based on momentum transfer correlations. By relating the drag coefficient to the skin friction coefficient, Duan & Duan [122] proposed a correlation for the Nusselt number of a single sphere,

$$\mathrm{Nu} \approx f(\mathrm{Re})\frac{\mathrm{C_d}\,\mathrm{Re}}{12}\mathrm{Pr}^{\alpha}, \qquad f(\mathrm{Re}) = \frac{\mathrm{Re}+\delta}{0.11\,\mathrm{Re}^{1.4}+\mathrm{Re}+\delta}. \tag{4.9}$$

Discrepancies in the analogy are modeled by the function $f(\mathrm{Re})$, with the Prandtl exponent set to $\alpha = 0.4$. The δ value within $f(\mathrm{Re})$ is adjusted from the one proposed by Duan & Duan, reducing it from $\delta = 5000$ to $\delta = 500$ for better alignment with experimental data at intermediate Reynolds numbers. To extend this correlation to an assembly of spheres, the influence of neighbouring particles must be considered. The methodology used to extend the drag force to an assembly is also applied to forced convection. The drag force on a sphere within an assembly is obtained by multiplying the drag force for a single sphere by the voidage function $g(\varepsilon, \mathrm{Re})$ and using the superficial Reynolds number instead of the Reynolds number. In this work, the voidage function proposed by [24] and [123] is used,

$$g(\varepsilon, \mathrm{Re}) = \varepsilon^{-1.8 + \exp\left[-\frac{(1.5-\log \mathrm{Re})^2}{2}\right]}, \tag{4.10}$$

and the drag coefficient correlation is the one proposed by [23]. It results in the following drag coefficient and Nusselt correlations for a sphere within an assembly

$$\mathrm{C_d} \approx g(\varepsilon, \mathrm{Re})\left(0.63 + \frac{4.8}{\sqrt{\varepsilon\,\mathrm{Re}}}\right)^2, \tag{4.11}$$

$$\mathrm{Nu} \approx g(\varepsilon, \mathrm{Re})\ f(\varepsilon\,\mathrm{Re})\ \left(0.18\sqrt{\varepsilon\,\mathrm{Re}} + 1.39\right)^2\ \mathrm{Pr}^{0.4}. \tag{4.12}$$

The proposed Nusselt correlation is compared with a collection of experimental data from the literature [115] in Figure 4.3. The experiment measures

heat transfer through a heated packed bed of spheres. In this dense regime the correlation is found to be in good agreement with the experimental data.

The density of heat transfer due to convection from the fluid to the particle is then obtained using Equation (4.12) as

$$q = \frac{1}{V}\frac{k\mathrm{Nu}}{d}S(T - T_p). \tag{4.13}$$

This expression can then be used to compute the convective heat transfer density q for each particle in the assembly in Equation (4.1). To apply it over the mesh, the same approach as for the drag force is used Equation(3.42), also with a semi-implicit scheme.

Two applications are presented in the following sections to illustrate the heat transfer mechanisms in granular flows. First is the heat transfer in a fluidised bed, where the heat transfer is driven by the fluid flow around the particles. Cold air is injected at the bottom of a hot granular bed with a velocity above the minimum fluidisation velocity. It results in a fluidised bubbling regime, where the heat transfer is dominated by the convective heat transfer. The second application is the spontaneous digging of a water droplet in a granular medium. A water droplet is placed on a hot granular bed, and the local vapourisation tends to locally fluidise the granular medium. The generated vapour also increases the cohesiveness of the granular medium, which affects the granular mobility and enables the formation of deep chimneys.

4.2 Fluidised Bubbling bed

In this section, the model is validated in the context of a fluidised bed based on the experiment proposed by Patil [116]. The bubbling regime is obtained by the injection of air at a sufficiently high velocity at the bottom of the container. The heat transfer between the particles and the fluid is driven by the bubble dynamics and the exchange at its boundary. Once a bubble rises through the particles bed, it drags particles along its path, reducing the local solid fraction. This motion allows the air to invade the bed and cool the particles. To validate the heat transfer model in this transient regime, an equivalent two-dimensional model is proposed and validated against the experimental data.

Two-dimensional simulations are performed based on a pseudo-2D bubbling fluidised bed. Figure 4.4 illustrates the geometry of the problem. The granular bed consists of hot spherical glass beads immersed in air initially at rest. Side walls at constant temperature $\hat{T}_w$ cool down the bed. At the bottom, a porous plate enables fluidisation by the injection of air at a prescribed flow velocity $\hat{\boldsymbol{u}} = (0, -\hat{v}, 0)$. The injected air forms bubbles that rise through the bed, ejecting particles along the way. A nozzle blocks the flow in the centre

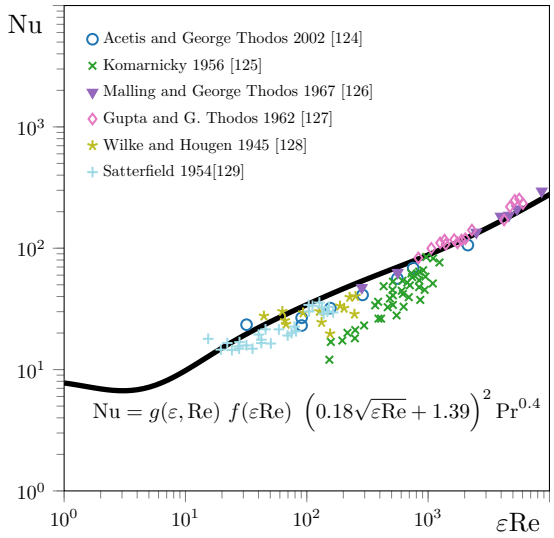

Figure 4.3: Nusselt number correlation of a sphere in a dense assembly. The black curve refers to the proposed correlation in equation (4.12) with a fluid volume fraction of $\varepsilon = 0.45$. The markers refers to experimental data collected by [115].

of the bottom plate. To avoid cristallisation, the diameter of the beads is uniformly distributed between $0.8d$ and d. Table 4.1 describes the physical and the geometry parameters used for the simulations.

Fluid properties		
ρ	kg/m^3	1.204
η	kg/(m s)	2×10^{-5}
c	J/(kg K)	1010
k	J/(s m K)	0.025
β	K^{-1}	0.003

Grain properties		
ρ	kg/m^3	2500
c	J/(kg K)	840
k	J/(s m K)	1.4
E	kg m/s	6×10^{-10}
ν	\	0.22
μ	\	0.3

Geometry properties		
h	cm	25
w	cm	8
p	cm	1.5
l	cm	1.2
d	mm	1

Boundary parameters		
$\hat{v}$	m/s	1.2, 1.54 and 1.71
$\hat{T}$	K	290
$\hat{T}_w$	K	290

Table 4.1: Parameters used for the fluidisation of a heated packed bed.

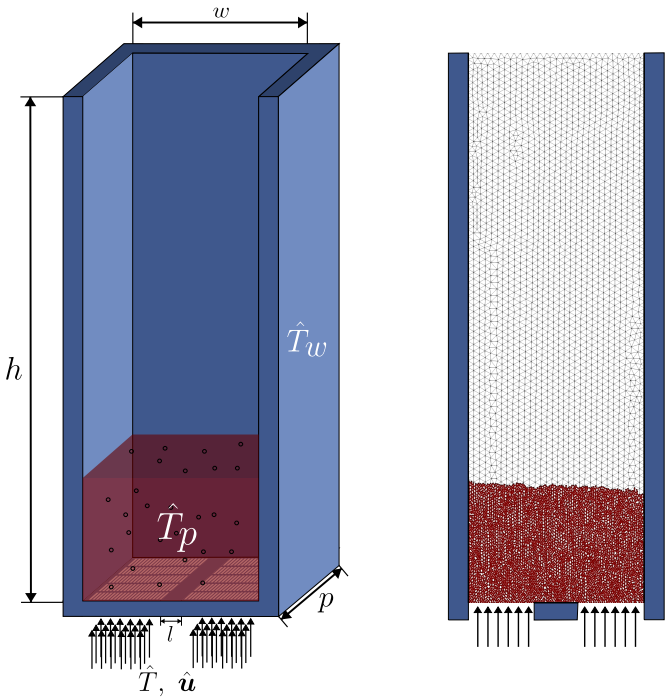

Figure 4.4: On the left, schematic of the pseudo-2d bubbling fluidised bed setup. On the right, two-dimensional numerical representation of the problem. Air at a lower temperature than the grains is injected through the bottom porous plate to fluidise the granular bed.

4.2.1 Numerical considerations

Due to the multi-scale nature of the model, the boundary layer is not fully resolved close to the wall. The heat transfer associated with these conditions is assumed to follow a Newton's law $q_w = \frac{h_w}{h}\left(\hat{T}_w - T\right)$ and its convection coefficient is set to be equivalent to the one used in the reference experiment by Patil [116], $h_w = 350$ [W m^{-2} K^{-1}]. The simulation is performed on a two-dimensional domain instead of a three-dimensional Hele-Shaw cell. Since the viscous effects damping the fluid flow and the forced convection in the vicinity of the front and rear walls are not captured, a volumetric drag force and a volumetric heat transfer model these longitudinal effects,

$$\boldsymbol{f}_l = -\gamma \boldsymbol{u}, \qquad q_l = \lambda(\hat{T}_w - T). \tag{4.14}$$

These two coefficients must be calibrated to reproduce experimental data. As suggested in [56], the drag coefficient is estimated by considering a Hagen-Poiseuille flow. The drag coefficient is assumed to be $\gamma = 12\mu/p^2$. Its value in these experiments is set to $\gamma \approx 1.067$ [kg m^{-3}s^{-1}]. The heat transfer coefficient is estimated by comparing the averaged particle temperature with the experimental data for an inflow velocity of $\hat{v} = 1.54$ [m/s] and the mass bed of $m = 75$ [g]. The estimated heat transfer coefficient is found to be $\lambda \approx 4\ 10^4$ [W m^{-3} K^{-1}]. All these parameters have been calibrated with a static friction coefficient between two particles as $\mu_s = 0.3$ and a coefficient of $\mu_s = 0.5$ between a particle and the wall. As long as the friction coefficient is non-zero, its impact on the dynamics of the bed is expected to be limited. Describing the beads as discs rather than spheres tends to underestimate their mobility, as seen in Section 3.2.3. In order to reproduce the same packing fraction and a similar mobility as in the three-dimensional case, the grains are assumed to be porous to reach the jamming packing fraction of a sphere packing. The jamming packing fraction of a disc packing is $\phi_{\max} = 0.9069$ while the jamming packing fraction of a sphere packing is $\phi_{\max} = 0.7405$. The boundary conditions at the walls, inflow and outflow are summarised in the following table, either a Dirichlet or a Neumann condition is applied.

Inflow	Outflow	Lateral Wall	Longitudinal Wall
$\boldsymbol{u} = \hat{\boldsymbol{u}}$	$\boldsymbol{f} = \boldsymbol{n} \cdot (\boldsymbol{\sigma} - \varepsilon\rho\boldsymbol{u}\boldsymbol{u})$	$\boldsymbol{u} = \boldsymbol{0}$	$\boldsymbol{f} = \boldsymbol{f}_l$
$T = \hat{T}$	$q = \boldsymbol{n} \cdot (-\boldsymbol{q} - \rho c \boldsymbol{u} T)$	$q = q_w$	$q = q_l$

4.2.2 Dynamics

Figure 4.5 shows the numerical results of the bed fluidisation by the air injection. As the bubbles rise through the granular bed, they drag particles with them. Due to the symmetry of the problem, a central aisle is naturally generated along which the particles are not dragged because of to the closed nozzle. The cooled particles accumulate at the bottom of the bed and are transported away by the convective cells created by the bubbles. Figure 4.7 illustrates this behaviour. Two symmetrical vortices can be seen in the wake of the bubbles. In these vortices, the particle velocity is upwards in the centre of the domain and downwards at the wall. As pointed out by Yang [130], the preferred path of the bubbles is along the centre of their region, resulting in a higher solid fraction at the edge of the domain.

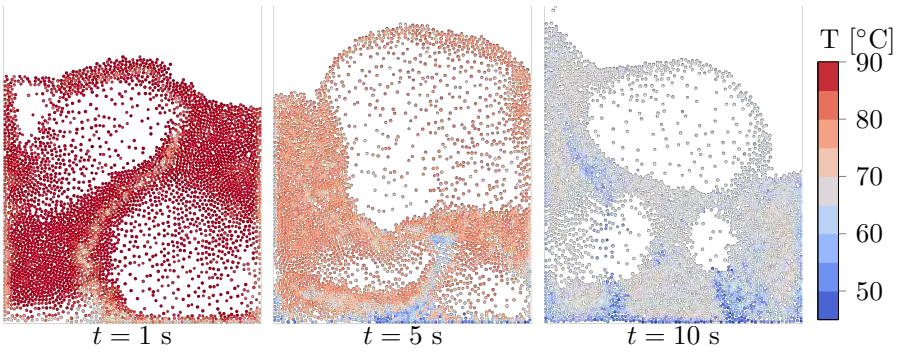

Figure 4.5: Snapshots of the particle dynamics at different time for $\bar{v} = 1.71$ [m/s] with a bed mass of $m = 75$ [g]. Particle temperature is represented by the color map.

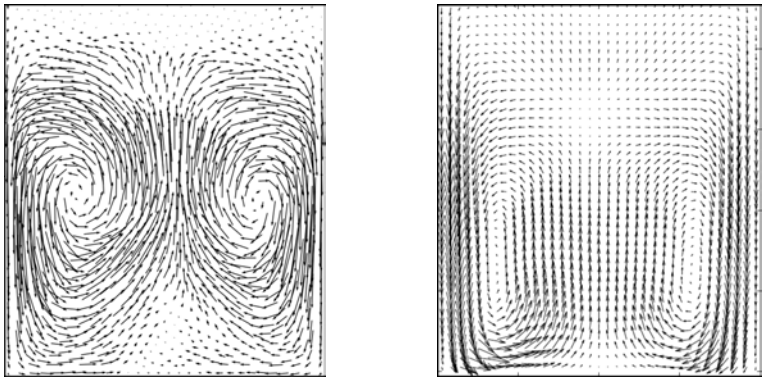

Numerical results Experimental results

Figure 4.6: Time-averaged particle velocity over a time of 5 seconds starting at a time of 5 [s].

4.2.3 Heat transfer

As the air flows through the bed, the particles are cooled down. The heat transfer between the particles and the fluid is controlled by the bubble dynamics and the exchange with the boundary. Increasing the inflow velocity increases the heat transfer between the particles and the fluid. Firstly, bubbles are more easily formed which favours particle motion. This movement reduces the local solid fraction allowing air to invade and cool the particles. Secondly, a higher inflow velocity increases the heat transfer coefficient. Figure 4.8 shows good agreement between the experimental and numerical results of the averaged particle temperature. The fluxes through the front and rear walls are calibrated on the set of measurements with a mass of $m = 75$ [g] and an inflow velocity of

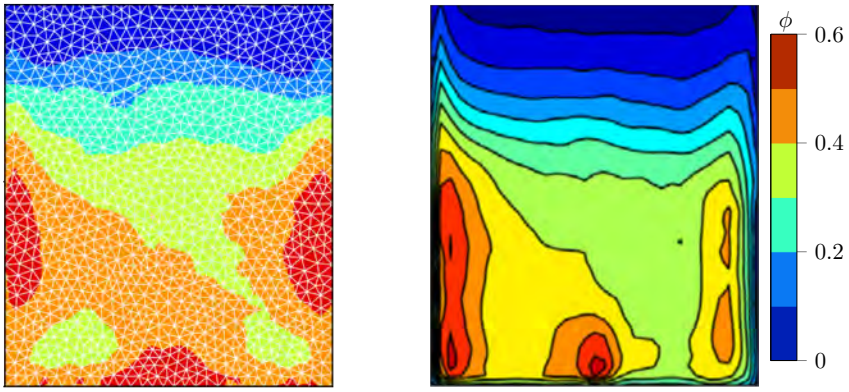

Figure 4.7: Time-averaged solid packing fraction over a time of 5 seconds starting at a time of 5 [s].

$\hat{v} = 1.54$ [m/s] and validated on others inflow velocities. The numerical model proposed on the basis of Equation (4.12) is able to reproduce qualitatively and quantitatively the heat transfer between the particles and the fluid. Based on this representation of a bubbling fluidised bed, local fluidisation is expected to be well represented.

4.3 Spontaneous digging of a water droplet

When a droplet falls into a hot granular bed, it is able to penetrate the granular medium spontaneously. This phenomenon was first documented by Lin [61] in a quasi-two-dimensional experiment and in a three-dimensional granular bed. In the latter case, the observations are limited to the grain ejection and to the final stage when the droplet is stopped. Once the droplet has stopped, a cohesive spherical structure can be extracted from the granular bed. In the quasi-two-dimensional experiment, the droplet motion and the fluidisation of the granular bed are observed through an Hele-Shaw cell. This cell is in fact quasi two-dimensional regarding the droplet motion, the grains being smaller than the droplet can still move in the depth direction. The numerical experiment presented in this work assumes a two-dimensional domain to mimic the experimental setup. However, the constraint in the third direction does not allow a quantitative comparison with the physical experiment. The main phenomena are still present and are investigated in this study.

Different regimes have been observed depending on the droplet's ability to fluidise the granular medium. In the first regime, vapourisation is not sufficient to create a layer of vapour at the interface between the droplet and the

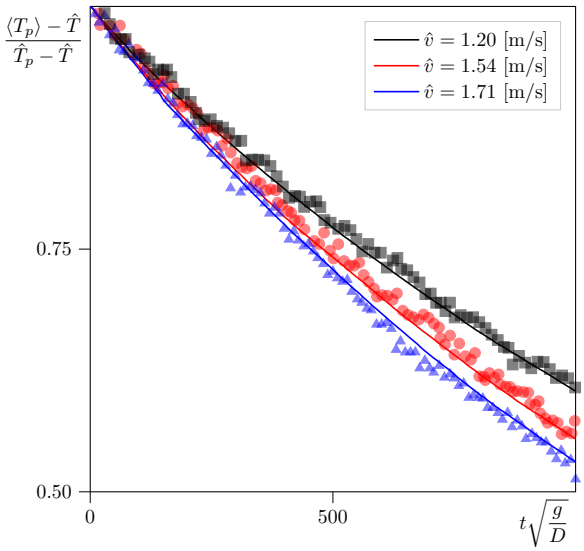

Figure 4.8: Mean particle temperature evolution. Experimental values, indicated by markers, have been extracted from [116]. Simulation results are shown by a continuous line for each set of data corresponding to different inflow velocity, respectively, 1.20, 1.54 and 1.71 [m/s].

granular medium. The droplet crashes into the granular medium, and a small cavity may form but does not deepen. In the second regime, a layer of vapour is created between the droplet and the granular medium. The droplet fluidises the surrounding particles. The grains are ejected into the resulting vertical chimney, and the droplet goes downwards before the granular medium reorganises. The droplet then takes the place of the ejected grains and continues to dig. In that regime, the local fluidisation tends to favour heat transfer with grains. The main result is that the droplet stops at different depths according to the temperature of the granular material. The maximum depth is found for a temperature between the starting digging temperature and the temperature for which the droplet remains at the surface. In the third regime, at high temperature, the droplet stops digging and is close to the surface. In the following, the droplet dynamics is studied in the second regime, named the digging regime, and to understand the stop of the droplet at high temperatures.

The numerical simulations aim to reproduce the non linear behaviour of the digging depth as a function of the temperature and to measure the ability of the droplet to cool down the granular material. The numerical experiment is based on the same material properties as the physical experiment, these properties are summarised in Table 4.2. Figure 4.9 illustrates the experimental setup and the numerical domain. The mesh size close to the droplet is refined to capture

the droplet motion and the fluidisation of the granular medium. Further away from the droplet, the mesh size is increased to reduce the computational cost.

The first section describes the model used to track the digging droplet in vapourisation. As the numerical model lives in a two-dimensional domain, the numerical considerations employed to mimic the experiment are then presented. In the following section, the droplet is followed for different granular bed temperatures to highlight the different regimes. The heat exchange governing the digging is then investigated in this regime at an initial temperature of 400° C, as seen in Figure 4.10. Finally, similarities and differences between the experiment and the numerical results are provided.

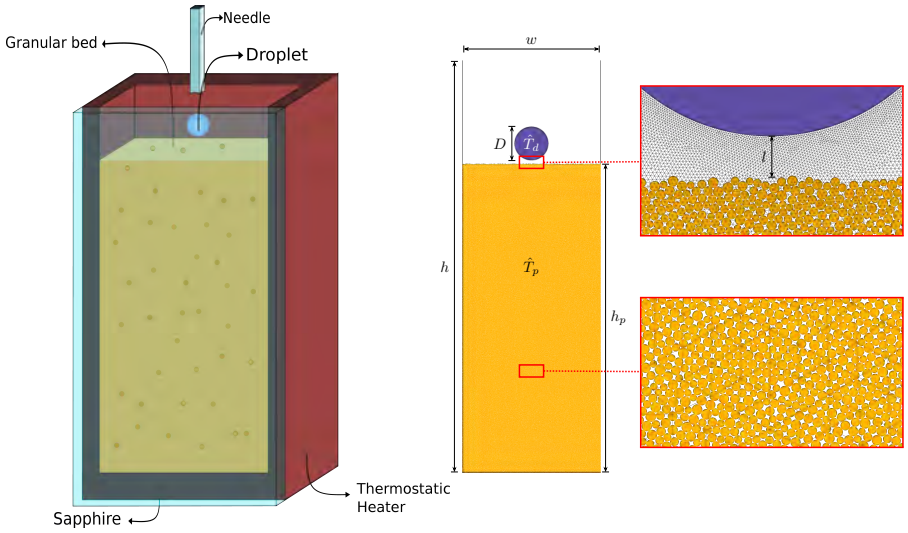

Figure 4.9: On the left, schematic of the experiment. On the right, its numerical representation. The mesh close to the droplet is refined and the mesh further away is larger than the particle size.

4.3.1 Droplet representation

As the droplet falls through the granular bed, it begins to absorb grains. The particles and the surrounding fluid contribute to the dynamics of the droplet and to its vapourisation. As long as enough energy is provided to the droplet, the expelled vapour fluidises the granular medium and allows the droplet to continue digging. During the digging, the droplet shape remains circular. Once the heat flux is not sufficient, the droplet stops and progressively fills with grains. The maximal depth is thus reached and a spherical cohesive structure can be extracted from the granular bed.

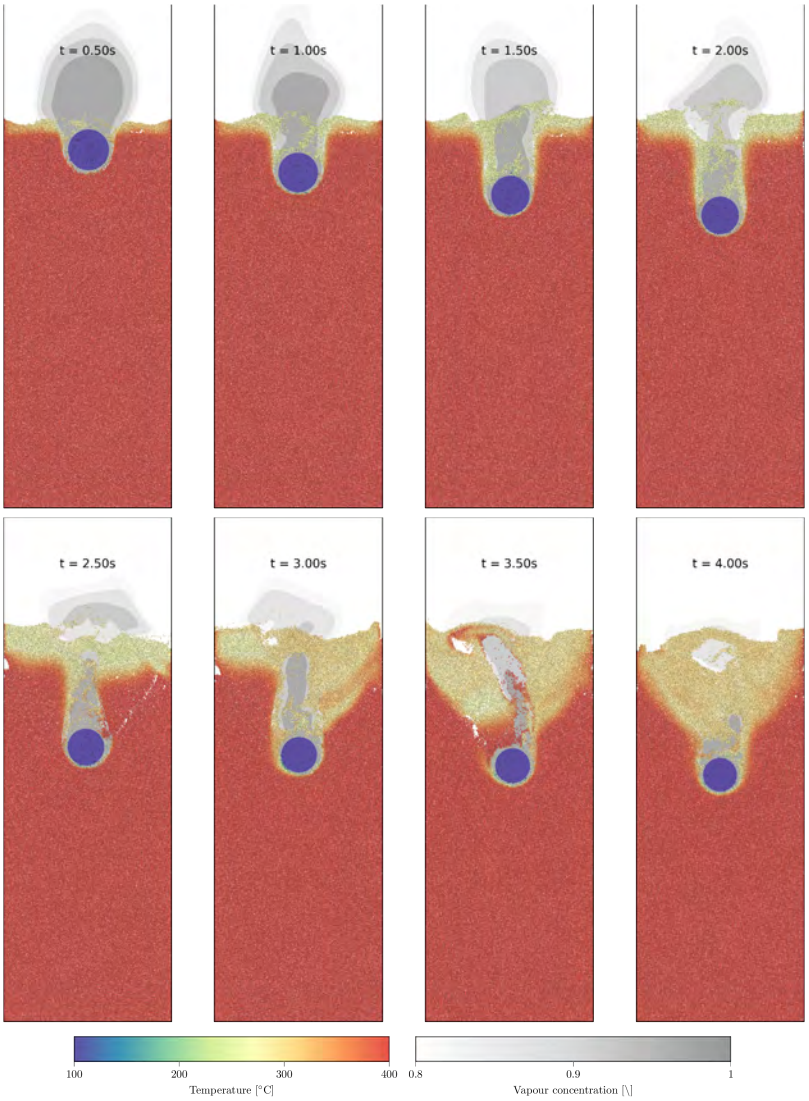

Figure 4.10: Snapshots of the droplet penetrating the granular bed at 400° C. The vapour field is indicated by shades of grey. The temperature of the grains is shown in red. The grains are ejected into the chimney as the droplet falls. The fluidisation of the grains allows the droplet to continue falling.

Following the averaged description of the surrounding fluid, the droplet is modelled as a mixture of the liquid phase and particles. The shape of a

Fluid properties		
ρ	kg/m^3	1.204
η	kg/(m s)	2 10^{-5}
c	J/(kg K)	1040
k	J/(s m K)	0.026
β	K^{-1}	3 10^{-3}
D_v	m^2/s	2 10^{-5}
ρ_v	kg/m^3	1.204

Grain properties		
ρ	kg/m^3	3200
c	J/(kg K)	290
k	J/(s m K)	234
E	kg m/s	10^{11}
ν	\	0.35
μ	\	0.3

Geometry properties		
w	mm	10
h	mm	30
h_p	mm	22.5
l	mm	1.5
D	mm	2.5
d	μm	55

Numerical parameters		
Δt	s	5 10^{-4}
F_c^0	kg m s^{-2}	7.5 10^{-4}
ψ^0	\	0.9

Table 4.2: Properties associated to the spontaneous digging experiment.

droplet is determined by the balance between buoyancy and surface tension, as well as the balance between inertial and viscous forces. These two balances are modelled respectively by the Eötvös number Eo and the Reynolds number Re_D. In the experiment, these numbers are given by

$$\mathrm{Eo} = \frac{\Delta\rho g D^2}{\sigma} \approx 1, \quad \mathrm{Re}_D = \frac{\rho D U}{\eta} \approx 10.$$

For these parameters, the droplet shape is close to spherical, as was observed experimentally by Lin [61]. This is also supported by the Grace diagram [131] which shows that a falling droplet shape is mainly spherical in this regime. Therefore, it is assumed that the shape of the droplet remains spherical during the digging process. The volume of the droplet V is given by the volume occupied by the liquid phase V_f and the absorbed particles V_p. The heat flux at the interface is entirely used to vaporise the water. The mass ratio $\dot{m}$ is then given by the latent heat of vapourisation $\mathcal{L}$ and the net heat flux. This heat flux is the sum of the transfer between the droplet and the surrounding air, Q_f and the transfer from the particles immersed in the droplet Q_p. The droplet dynamics is derived from the Volume-Averaged Navier-Stokes equations, Equation (3.33), integrated over the droplet volume. The stress tensor is computed using the solution in the fluid phase since the inside of the droplet is not solved. The droplet is then fully described by the following equations,

$$V = V_f + V_p \tag{4.15}$$
$$\mathcal{L}\dot{m} = Q_f + Q_p \tag{4.16}$$
$$m\frac{\mathrm{d}\boldsymbol{u}_d}{\mathrm{d}t} = \boldsymbol{F}_f + \boldsymbol{F}_p + m\boldsymbol{g}, \tag{4.17}$$

where $\boldsymbol{F}_f$ is the force applied by the fluid on the particles and $\boldsymbol{F}_p$ is the force applied by the particles on the fluid. It is worth noting that the resulting surface tension over the boundary is null as the droplet remains circular. Figure 4.11 illustrates the heat, mass and momentum transfer over the droplet.

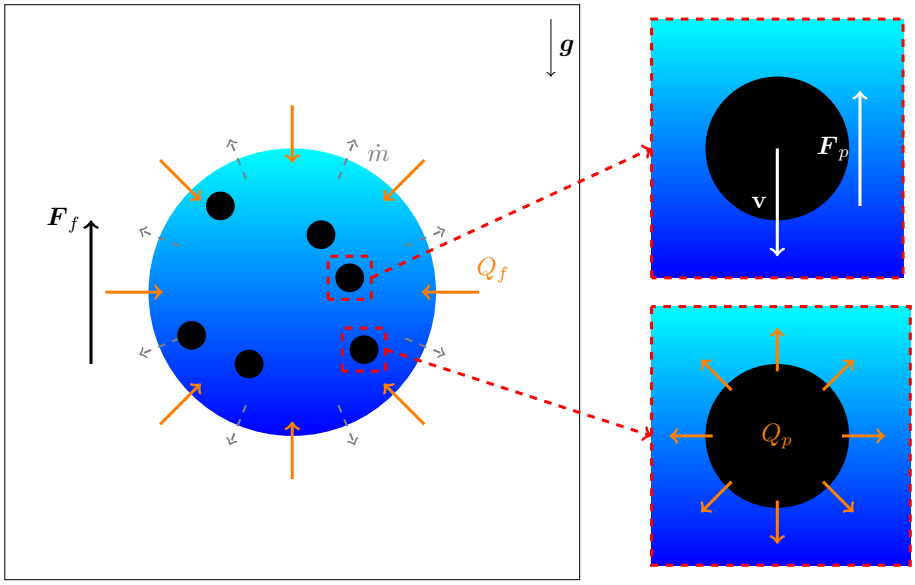

Figure 4.11: Droplet representation. The motion of the droplet is balanced by its weight $m\boldsymbol{g}$, the force exerted by the particles $\boldsymbol{F_p}$ and the force exerted by the surrounding fluid $\boldsymbol{F_f}$. Due to the temperature gradient, the droplet is subject to a heat flux Q_f from the surrounding fluid and a heat flux Q_p from the particles. The net heat transfer is used to vaporise the droplet.

4.3.2 Numerical considerations

To represent the initial conditions of the experiment, the granular bed is represented as an assembly of discs. A space-filling algorithm is used to minimise voids between particles [132]. As solid packing fraction controls the fluidisation of a granular bed, particles are assumed to be porous to maintain a volume fraction similar to the physical experiment measured at $\phi \approx 0.4$.

In order to limit the granular medium's ability to reorganise itself, cohesion is added between the grains. The vapour field ψ acts as an indicator of the fluidisation of the granular medium. A contact is considered cohesive if it persists for several time steps and it is not located in a fluidised region [133]:

$$F_c = \begin{cases} F_c^0 & \text{if } \psi < \psi^0, \\ 0 & \text{otherwise} \end{cases} \tag{4.18}$$

where ψ is the vapour concentration at the contact point and ψ^0 the vapour threshold. This is equivalent to assuming negligeable the cohesive force in the capillary regime and a constant force in the funicular and pendular regimes.

The vapour field is described by the advection-diffusion equation;

$$\partial_t(\varepsilon\rho_v\psi) + \boldsymbol{\nabla}\cdot(\varepsilon\rho_v\boldsymbol{u}\psi) = \boldsymbol{\nabla}\cdot(\varepsilon D_v\boldsymbol{\nabla}\psi) \tag{4.19}$$

where ρ_v is the vapour density and D_v is the vapour diffusion coefficient. The cohesive force is modelled as a contact force between the grains, which is integrated into the non-smooth contact dynamics.

Since the walls are used to heat the granular medium, they are assumed to maintain a constant temperature $\hat{T}_p$, which corresponds to the initial temperature of the grains. The high temperature of the granular bed rapidly heats the droplet to its vapourisation temperature $\hat{T}_d = 100$ °C . This transient heating process is considered instantaneous, after which the droplet is assumed to be at its vapourisation temperature. The produced vapour generates a flow from the droplet to the surrounding fluid in the radial direction, denoted $\hat{\boldsymbol{r}}$. At the top of the domain, an outflow boundary condition is applied. The boundary conditions applied to the fluid conservation equations and the vapour field can be summarised as,

Outflow	Wall	Droplet
$\boldsymbol{f} = \boldsymbol{n}\cdot(\boldsymbol{\sigma} - \varepsilon\rho\boldsymbol{u}\boldsymbol{u})$	$\boldsymbol{u} = \boldsymbol{0}$	$\boldsymbol{u} = \boldsymbol{u}_d + \frac{\dot{m}}{\rho_v S}\hat{\boldsymbol{r}}$
$q = \boldsymbol{n}\cdot(-\boldsymbol{q} - \rho c\boldsymbol{u}T)$	$T = \hat{T}_p$	$T = \hat{T}_d$
$\psi = \boldsymbol{n}\cdot(\varepsilon D_v\boldsymbol{\nabla}\psi - \varepsilon\rho_v\boldsymbol{u}\psi)$	$\psi = 0$	$\psi = 1$

These boundary conditions are used to mimic the experimental setup. Depending on the heating device and on the border mass, the characteristic time to heat the granular assembly at the requested temperature is much longer that the digging process, which lasts about one minute. The temperature of the granular material changes at the vicinity of the droplet. However, since the droplets are far from the border, except in the depth direction, the wall temperature can be considered as constant. The front and rear walls are made of sapphire and aluminium, respectively. Three facts can be evidenced to claim for constant temperature walls: first, the droplet digs, that means that the

droplet moves and does not cool down the wall at the same place. Secondly, the walls are made of high thermal conductivity materials compared to the granular material. Thirdly, the mass of the walls are large compared to the droplet. We can consider the walls to be thermal reservoirs.

The numerical scheme is summarised in Figure 4.12. At each time step, the local fluid volume fraction over the domain is computed. To couple the fluid conservation equations with particles, a semi-implicit scheme is used [59]. The heat equation is solved to compute the temperature field based on Equation (4.4) using the Nusselt correlation, Equation (4.12). The mass rate is computed based on the heat flux at the droplet interface using Equation (4.16). It provides the boundary condition to close the fluid model at the droplet interface. Volume and momentum conservation are solved using Equation (3.33) with the momentum transfer between the fluid and the particles, Equation 4.11. The force from the fluid and the particles are exerted on the droplet to compute its motion, based on Equation (4.17). The droplet volume is updated based on the mass rate and the particles entering and leaving the droplet, Equation (4.15). To track the droplet motion and its radial expansion, the mesh is deformed so that it remains conformed to the droplet boundary and maintains good mesh quality. A node will be moved by the following expression:

$$\boldsymbol{x}_{new} = \begin{cases} \boldsymbol{x} - \left(1 - \frac{\|\boldsymbol{x}-\boldsymbol{x}_d\|-r_d}{L}\right)\boldsymbol{u}_d\Delta t, & \text{if } \|\boldsymbol{x}-\boldsymbol{x}_d\| < r_d + L \\ \boldsymbol{x}, & \text{otherwise} \end{cases} \tag{4.20}$$

where $\boldsymbol{x}$ is the node position, $\boldsymbol{x}_d$ is the droplet position, r_d is the droplet radius, L is the maximal from where a node can move, its value has been set to $L = 1.5r_d$, and $\boldsymbol{u}_d$ is the droplet velocity. The node velocity is taken into account in the material derivative in the conservation equations using the Arbitrary Lagrangian-Eulerian (ALE) framework,

$$\frac{\mathrm{d}\bullet}{\mathrm{d}t} = \frac{\partial\bullet}{\partial t} + (\boldsymbol{u} - \boldsymbol{u}_m)\cdot\boldsymbol{\nabla}\bullet \tag{4.21}$$

where $\boldsymbol{u}$ is the fluid velocity, $\boldsymbol{u_m}$ is the mesh velocity. The mesh velocity is integrated explicitly in the time integration scheme, which leads to a non-conservative ALE method. To avoid mesh distortion, the domain is remeshed every 25 time steps, equivalent to every 0.0125 seconds. GMSH was used as the mesh generator. At this rate, remeshing has no impact on the computational cost which is dominated by the contact dynamics and the linear system resolution. Once the domain has been remeshed, all the fluid degree of freedom are interpolated from the previous mesh to the new one.

4.3.3 One droplet, three regimes

As briefly detailed above, when the droplet falls into the granular medium, three regimes are obtained depending on the initial temperature of the granular bed.

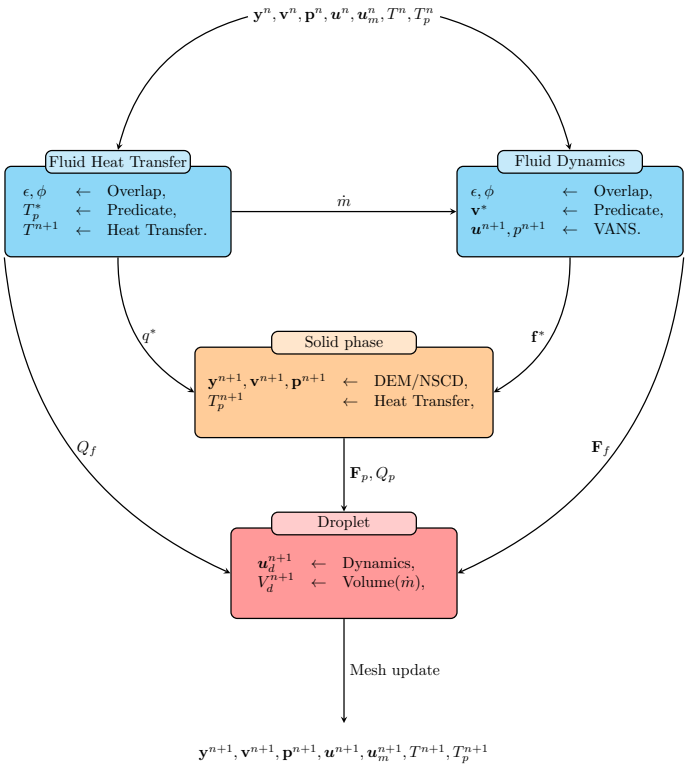

Figure 4.12: Numerical procedure.

These three regimes are characterised by the ability of the droplet to fluidise the granular medium: (i) at low temperatures, the droplet cannot fluidise on a long time, (ii) at intermediate temperatures, the droplet digs, and (iii) at high temperatures, the droplet remains at the top layers of the granular bed.

Figure 4.13 illustrates the final depth reached by the droplet for different temperatures ranging from 300 to 600 °C. Three regimes are observed. In the first regime, for temperatures below 350°C, the droplet crashes into the granular medium without being able to fluidise its surrounding environment. The depth of the droplet is then limited to the depth of the initial cavity, and the droplet does not hollow out. Consequently, the droplet vaporises at the surface of the granular bed without ejecting any grains. On the other hand, at the highest temperatures, one expects a large and violent ejection of grains since the production of vapour increases with the temperature of the bed. However, we observe that below the droplet, the grains are ejected but because the vapour gap is large, they reorganise below the droplet before the droplet can take their place. The intermediate regime is observed for temperatures

between 350 and 500°C. In this regime, vapour ejection is sufficient to locally fluidise the granular medium without stopping the droplet from falling. Indeed, the grains below the droplet do not have time to reorganise before the droplet takes their place.

Regarding the change of temperature produced by the passage of the droplet, in Figure 4.13. The colour of the grains is related to their temperature (see colour bar). The area cooled down by the droplet can therefore be observed. Remarkably, even if the droplet does not dig deep, the temperature is modified on a range equivalent to at least one droplet diameter, see $T = 500$°C for example.

The droplet depth evolution, namely the depth h reached by the droplet normalised by its diameter as a function of dimensionless time, is shown in Figure 4.14 and this, for four initial temperatures of the bed. Dimensionless time is defined as the free fall time for the droplet to travel its radius. We observe the same behaviour during the first second. The droplet manages to penetrate the first layers of grains with the same apparent speed. Then, according to the temperature, the droplet speed decreases before it stops at a maximum depth that depends on the temperature considered. Note the peculiar behaviours at 500 and 600°C for which the droplet bounces back upwards. This is due to the reorganisation of the grains below the droplet. The vapour gap is large enough to allow the vapour to escape without entraining grains. The grains move and reorganise provoking the local collapse of the chimney. The droplet then goes up. On the other hand, when the droplet digs, it can reach depths 10 times its initial radius. The maximum depth is reached at a temperature of 400 °C.

Figure 4.15 illustrates the evolution of the dimensionless falling velocity with respect to dimensionless time for the same four temperatures of Figure 4.14. As observed on the trajectories, the initial speeds are of the same order of magnitude whatever the temperature of the granular bed. The speed of fall decreases as a function of time as the impact of vapourisation becomes more and more important as the droplet loses mass. The third regime is characterised by temperatures above 500 °C. In this case, the droplet is considerably slowed down by the ejection of steam, even though the grains are highly fluidised. The droplet starts to bounce onto the granular bed and rises back to the surface.

The dependence of the speed with the temperature is not monotonous. If we measure the speed at $t = 2$ s, the speed increases with the temperature until $T = 400$°C before decreasing. The speed in the first and third regime is roughly zero as the droplet cannot dig. The maximal speed and depth is found for the intermediate temperature, namely when $T = 400$°C.

Comparing the simulations to the experiments, we can see that the major features are fully reproduced by the simulations: (i) The three regimes are found, two non-digging and one digging regime, (ii) The depth is found to increase with time before stopping at a given depth that depends on the temperature, (iii) the digging speed is maximum at an intermediate temperature,

and (iv) the reached depths depend on the temperature and a maximum of the digging depth is found when T=400 °C. This is what is observed in the quasi-2D experiments. The bounce back of the droplet is however not observed in the experiments. Another difference with the experiments is that the droplet takes some time to cross the interface before showing the constant digging speed regimes. This difference with the simulations is attributed to the large thermal gradients that are found along the first layers of grains in the experiments. This is due to radiation and heat exchange with the atmosphere that decrease the temperature of the first layers compared to the bulk. This explains why the numerical simulations produces different results, as the temperature of the grains is more homogeneous. Consequently, the droplet experiences some difficulties to cross the interface in the experiments.

In the experiments, as soon as the droplet is at a depth larger than its diameter, the droplet digs with a constant speed. This is less pronounced in the numerical simulations. Indeed, the difference is probably due to the fact that the simulations are pure 2D and to the fact that experiments are quasi-2D. The ejection of the grains is not eased by the 2D constraints since the grains organise along very compact configurations. Finally, we cannot reject the influence of the border in the experimental set-up: the front side is made of sapphire and the rear side of copper. This friction is consequently not captured in the model.

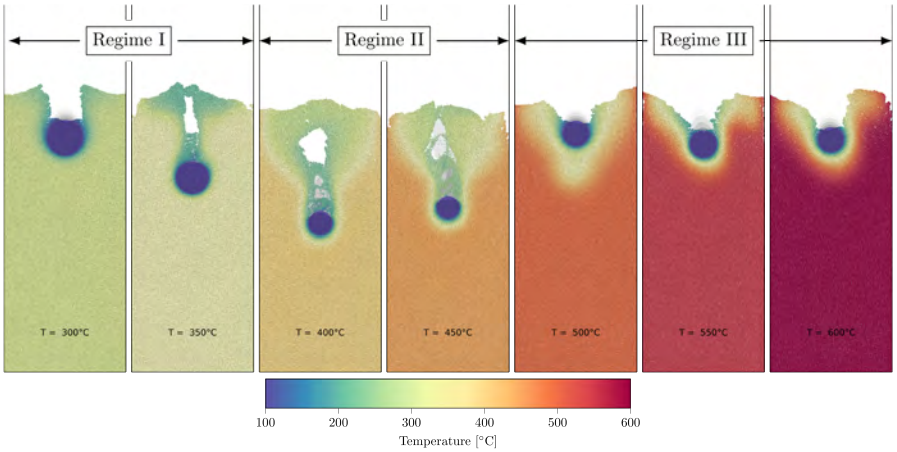

Figure 4.13: Final depth reached by the droplet at differents initial temperature of the granular bed.

As suggested by Figure 4.13, fluidisation of the granular medium promotes heat transfer between the droplet and the granular medium. This increase can be seen in the average temperature of granular bed over time, which can

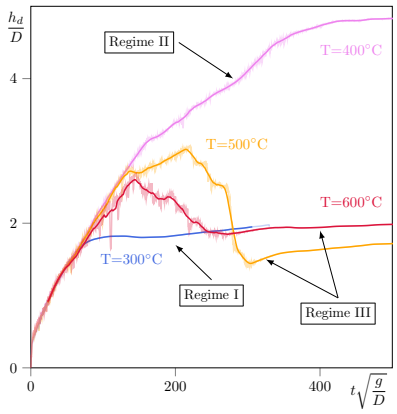

Figure 4.14: Droplet depth evolution

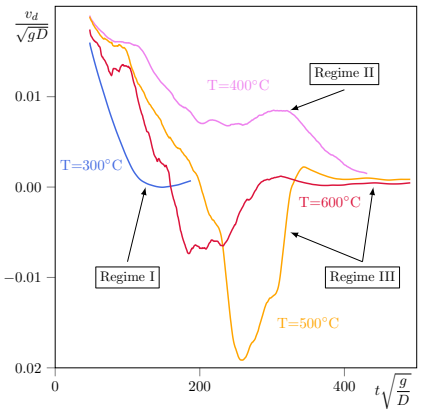

Figure 4.15: Droplet velocity evolution

be observed in Figure 4.16. The temperature was normalised in order to be compared with the four considered starting temperatures. At 400°C, the temperature decrease is the most efficient because the droplet goes the deepest interacting with more grains. Generally speaking, at intermediate temperatures, the droplet motion is characterised by a prolonged period of fluidisation, which increases the cooling of the grains. In addition, ejecting grains into the chimney cools grains that are initially deeper and still hot. The third regime does not follow this behaviour. Indeed, the reorganisation of the granular medium before the droplet falls leads to weaker interaction between the droplet and the granular medium because the temperature differences are smaller. The heat transfer is localised at the first layers of the granular material, the heat being conveyed to the droplet via the contact network between the grains. In all regimes, a screening effect is observed as the droplet becomes saturated with grains. Heat is then transferred less effectively between the droplet and the granular medium. This effect is particularly visible in Figure 4.17 indicating an estimate of the instant lifetime of the droplet over time.

The instant lifetime is calculated as $m(t)/\dot{m}(t)$ and reported in Figure 4.17. This quantity enables the effective heat transfer to be tracked as a function of time. In the initial stages of the fall, the grains passing through the droplet are rapidly ejected into the chimney, so they do not produce any screening effect. The lifetime is then of the order of ten seconds. Subsequently, as the droplet becomes saturated with grains and the medium containing the droplet is then described as a wet medium, the heat is transferred less effectively. The lifetime increases sharply, reaching up to several minutes. The heat transfer is observed to be maximum at $T = 400$ °C which is coherent with the previous observations. As soon as the droplet sits and does not move, the heat transfer decreases and a plateau is observed. Heat transfer can then only proceed along

the contact network and through exchange with the gas. This contrasts with a moving droplet whose environment has a larger temperature.

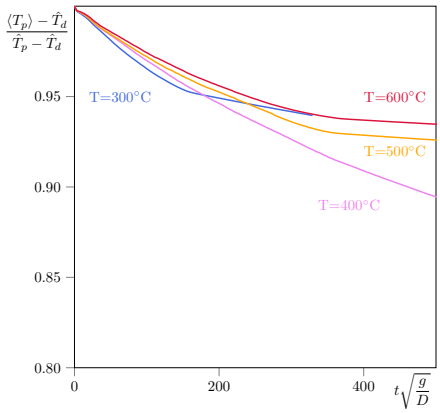

Figure 4.16: Mean particle temperature evolution.

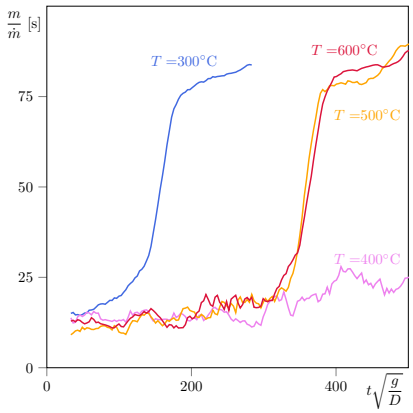

Figure 4.17: Droplet instantaneous lifetime.

4.3.4 Spontaneous digging at 400 °C

Since transfer is maximal at a temperature of 400 °C, the droplet was carefully monitored at this temperature. Figure 4.10 shows the droplet penetration into the granular bed at different snapshots for a granular bed temperature of 400° C at 8 different times (see Legend). The chimney starts building already after the first seconds. The cone of cooling is clearly visible at $t = 3$ s and even some bubbles of vapour can be seen.

As the droplet interacts with the granular medium, a thick layer of vapour is produced. The droplet is strongly slowed down by the force of the steam and this ejection allows the grains to be fluidised around the droplet. Finally, the grains are ejected in the wake of the droplet, and the droplet is able to take the place of the ejected grains and continues to dig. The different forces acting on the droplet can be isolated and measured as a function of time. The weight mg, the fluid-particule force F_f, the particle-fluid force F_p, and the resulting force F_{net} are presented as a function of time in Figure 4.18. In parallel, one can also follow the evolution of the heat exchange Q_p, Q_f and Q_{net} in Figure 4.19. The forces have been scaled by the initial weight of the droplet and the heat fluxes by the initial conductive flux at the droplet interface.

Once the droplet has fully penetrated the granular medium, the average forces applied by the vapour and the grains balance the weight of the droplet. The droplet then reaches its terminal velocity. Particles ejected in the wake of the fall form a chimney which is maintained by the fluidisation of the grains.

As the droplet falls, the particles ejected into the chimney fall back down and pass through the droplet, cooling the granular medium. This reduces heat flow in close proximity to the droplet as seen in Figure 4.19. Fluidisation of the granular medium is then reduced. Once fluidisation stops, the droplet absorbs the grains through its front. The droplet is then slowed down by the captured grains, and the thrust force of the vapour is insufficient to keep the droplet levitating. Digging stops and the droplet comes to rest.

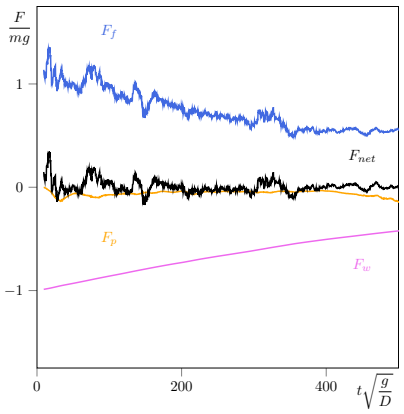

Figure 4.18: Force contribution evolution to the droplet motion.

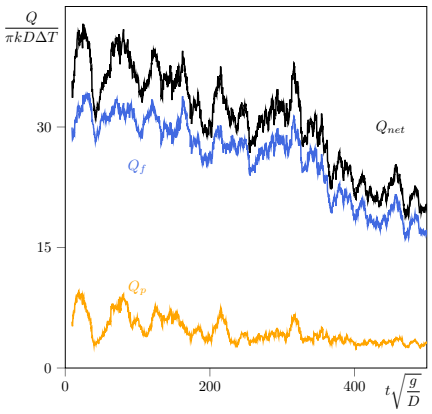

Figure 4.19: Heat transfer evolution over the droplet.

As the droplet falls, it cools only the grains in its wake. The deeper the droplet, the longer the chimney and the grains within it are cooled. The temperature under the droplet changes only slightly during the fall. Figure 4.20 shows the vertical average particle temperature profile. The grains in the chimney are cooled by the droplet without reaching the vapourisation temperature. As the droplet gathers grains in itself, they reach vapourisation temperature. Then, they are ejected into the chimney where their temperature increases. The resulting temperatures reach half their initial temperature. This effect can be seen in Figure 4.21 which shows the horizontal average particle temperature profile at a specific height.

Conclusion

This section presents an extension to the multiphysics model to include heat transfer. To this end, the volume-averaged energy conservation equation has been derived and applied to the study of fluidised bubbling beds and the spontaneous digging of a water droplet. A constitutive law has been proposed, Equation (4.12), to model the heat transfer between the fluid and the particles based on the Colburn-Reynolds analogy and the Di Felice voidage func-

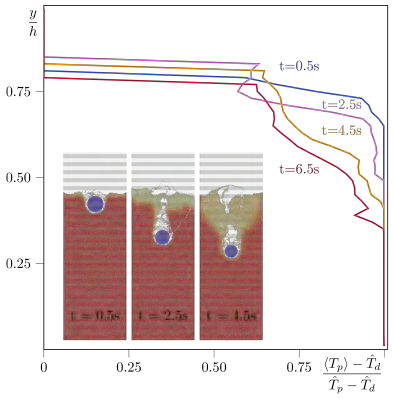

Figure 4.20: Vertical particle temperature profile at different snapshots. The alternating greys cells indicates the cell decomposition on which the averaging process is performed.

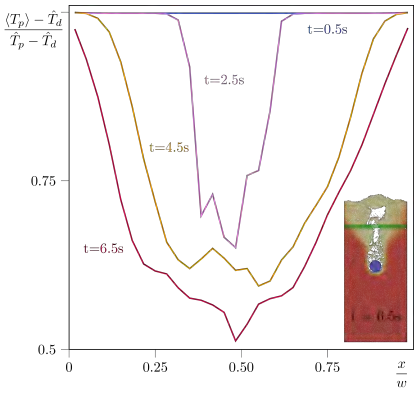

Figure 4.21: Horizontal particle temperature profile in a given cell highlighted in green.

tion. This correlation has been validated against experimental measurements of heated granular beds taken from the literature [115]. The implementation of the model was then successfully validated on the study of a bubbling fluidised granular bed by reproducing Patil's experiment [116].

The two-dimensional model was then applied to the study of the spontaneous digging of a droplet of water in a hot granular bed. Depending on the temperature, the vapourisation of the droplet causes the granular bed to fluidise locally and dig into the granular bed. The absorption of grains within the droplet is achieved by representing the droplet as a mixture of water and grains. Three digging regimes were observed as expected from the experiment. The first regime is characterised by no digging, the vapourisation of the water is not sufficient to fluidise the granular bed and the water droplet remains on the surface. The second regime, obtained at intermediate temperatures, is characterised by deeper digging. The water vapourisation is sufficient to fluidise the granular bed while allowing the droplet to fall. The droplet takes the place of the grains and penetrates into the granular bed. At high temperatures, the third regime is reached, whereby the droplet returns to the surface. Vapourisation slows the droplet's fall, allowing the granular bed to reorganise around the droplet, preventing it from sinking. The model greatly simplifies the experiment as the local fluidisation of a granular bed is controlled by the cohesion of the grains. This parameter has a significant effect as it limits the mobility of the grains, which can favour digging by preventing the grains from reorganising around the droplet. However, the numerical model reproduces the main trends of the experiment, namely digging, local fluidisation and chimney

formation.

Vapourisation of the droplet is the main source of heat transfer in the system and enables a local fluidisation in the wake of the fall. When the grains are absorbed by the droplet, a screening effect is observed which reduces the heat transfer. However, the heat contributed by the retained grains does not account for the majority of the heat exchanged with the fluid. The fluid remains hot through the granular bed. Evaporation reduces the surface area of the droplet, thereby reducing vapourisation. When the vapourisation is insufficient to eject the grains towards the chimney, the droplet ceases to fall. It then fills up with grains at the front and stops. The droplet becomes saturated and can no longer transfer heat to the outside. Its lifetime then increases considerably.

CHAPTER 5

PFEM-DEM for Fluid-Granular flows with Free Surface

Fluid mechanics problems involving free surfaces and granular materials are complex, multi-physics phenomena that require a deep understanding of both fluid dynamics and granular interactions. Such flows are highly relevant to civil engineering, geophysical processes, and numerous industrial applications.

A particularly illustrative example is that of landslides. These natural events can have catastrophic consequences, so improving our ability to understand their dynamics and predict their impact is crucial for risk mitigation. Landslides typically occur when soils on steep slopes become unstable. In some cases, the collapsing soil impacts a water body, generating large impulse waves, known as landslide tsunamis [134]. In other cases, known as submarine landslides, the soil detaches entirely underwater, again producing significant surface waves. Accurately simulating wave generation and predicting its propagation remains a major scientific and engineering challenge [135].

These phenomena involve two primary interfaces: the solid–fluid interface between the moving soil and the water, and the fluid–air interface at the water surface. Figure 5.1 illustrates these two interfaces in a typical landslide scenario.

Simulating such systems requires numerical solvers capable of handling both physical and geometric non-linearities. The former arises from the strongly nonlinear interaction laws between the fluid and granular phases, which we address using a volume-averaged formulation (see Chapter 3). The latter

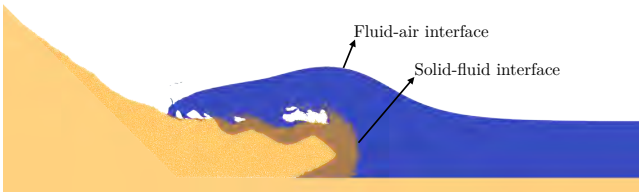

Figure 5.1: Two main interfaces increase the complexity of the problem: the free surface between the fluid and the air, and the solid–fluid interface between soil and water.

arises from the large deformations and topological changes that occur at the free surfaces and solid–fluid boundaries. These moving interfaces are central to accurately modelling landslide-generated waves.

To model the fluid–air interface, various strategies have been proposed. Multiphase formulations, such as Volume of Fluid (VOF) [136] and Level-Set methods [137], simulate both fluids simultaneously. However, this can be computationally expensive, since the lighter air phase often requires finer time steps due to its faster dynamics, despite having little influence on the overall flow. Moreover, the smoothing effects inherent in these methods can result in inaccurate tracking of sharp interfaces or significant topological changes. An alternative approach is to simulate only the heavier fluid, and treat the fluid–air interface as a free surface with a kinematic condition of zero normal flux. This simplifies the domain and allows larger time steps, but introduces challenges in tracking the moving interface and handling topological transitions such as merging or fragmentation. Recent methods such as [138] have even managed to capture air pockets in enclosed flows without explicitly solving for the air phase. Lagrangian approaches are particularly well-suited to this class of problems, as they naturally follow material deformation. These methods can be either meshless, as in Smoothed Particle Hydrodynamics (SPH) [139], the Material Point Method (MPM) [140], and the Lattice Boltzmann Method (LBM) [141], or mesh-based, such as Arbitrary Lagrangian-Eulerian (ALE) [42]. Mesh-based Lagrangian methods benefit from a strong theoretical foundation, particularly via finite element formulations. However, they can struggle with large deformations and topological changes. With recent advances in mesh generation techniques[142], however, this step should no longer be considered a bottleneck to the entire simulation process.

In this work, we employ the Particle Finite Element Method (PFEM) [43], which is a Lagrangian mesh-based method that is particularly well-suited to problems with evolving free surfaces. The PFEM solves the equations of motion using finite elements and then displaces the mesh nodes (i.e. the particles) based on the computed velocity or displacement field. To prevent distortion of the mesh, it is rebuilt at every time step, with only the particle positions

retained and the domain re-triangulated. The free surface boundary is then tracked through the use of an indicator function that defines the shape of the domain.

Our objective is to simulate the interaction between granular flows and free surfaces, which requires the sharp and accurate tracking of the fluid–air and fluid–solid interfaces under large deformation. Several modelling strategies have been explored in the literature. For example, Eulerian–Lagrangian methods such as FEM–DEM couplings with multiphase flow formulations have been proposed [143]. In these methods, the fluid is handled on an Eulerian mesh using a conservative level-set method for free surfaces and an immersed boundary method for granular particles. While these methods are highly accurate, they are often expensive and struggle with strong topological changes.

Fully Lagrangian–Lagrangian approaches have also been developed. The Moving Particle Semi-implicit (MPS) method for fluids coupled with DEM [144], or SPH–DEM formulations [145], avoids mesh generation entirely. However, these approaches require a high ratio of fluid particles around each solid particle, which can be problematic during impact events when particles transition from air to fluid.

In [146], a two-phase continuum PFEM formulation was proposed to simulate the 1963 Vajont rockslide and tsunami. Both the water and the landslide materials are modelled using PFEM, but with different constitutive laws: a Newtonian fluid model is used for water and a viscoplastic frictional model is used for the landslide.

Building on these approaches, Franci et al. [62] proposed a PFEM–DEM one-way coupling for particle-laden flows, neglecting the back effect of the particles on the fluid. Although their methodology is similar to ours, it does not account for two-way coupling, which becomes essential when the granular phase significantly alters the fluid motion.

In this chapter, we propose a coupled PFEM–DEM approach for modelling granular free-surface flows with two-way coupling and adaptive refinement near topological changes. The governing equations and coupling strategy were introduced in Chapter 3. Here, we provide details of the PFEM numerical scheme for the fluid, its integration into the existing DEM framework, and the treatment of interface dynamics. The model has been validated against numerical and physical benchmarks [63], including the 1958 Lituya Bay landslide and tsunami [64]. This chapter builds upon the following publication:

- Leyssens, T., **Henry, M.**, Lambrechts, J., Legat, V., Remacle, J.-F., (2025),
  A Coupled PFEM-DEM Model for Fluid-Granular Flows with Free-Surface Dynamics Applied to Landslides. Journal of Computational Physics

Contents

5.1 Numerical scheme

To track the fluid domain, the Particle Finite Element Method (PFEM) is presented within the CFD-DEM procedure. The numerical scheme is detailed in this section. An overview of the algorithm is illustrated in Figure 5.2. First and foremost, both the fluid and solid phases are represented by two separate sets of particles. To lighten the vocabulary, we will use the word *grains* to refer to the solid particles and *particles* for the fluid particles in the following. The iterative numerical procedure can be divided into three main steps:

Geometry detection involves defining the fluid domain and its boundaries. The boundary of the fluid domain is detected based on a geometric criterion. These boundaries are then coloured in order to assign to the proper boundary conditions in the resolution step. Additionally, a mesh adaptation is performed to ensure that the elements inside the fluid domain respect the given size field.

Resolution is to solve the equations of motion for both phases. The fluid phase is solved using the VANS equations in the Lagrangian formulation with the Finite Element Method. Contact dynamics is then used to determine the grains velocities at the end of the time step, based on the forces applied to them.

Advection consists of updating the positions of the particles and grains based on their velocities.

5.1.1 Geometry detection

In order to capture highly deforming flow, the particle finite element method seeks to track the geometric evolution. This is achieved using the Delaunay triangulation followed by a filtering of the elements based on a geometric criterion. The boundaries are then detected and coloured to be assigned to the proper boundary conditions. The free surface interface is captured sharply, and the method can handle topological changes. This step is purely geometric and does not involve any physical quantities.

α-shape

The fluid domain is represented by a set of particles S. The aim is to identify the boundary associated with this point cloud. This concept is not unique, here the α-shape algorithm [147] is used to detect the boundaries. The α-shape is closely linked to the Delaunay triangulation of the point cloud. Indeed, the α-complex of S is the set of triangles of the Delaunay triangulation whose

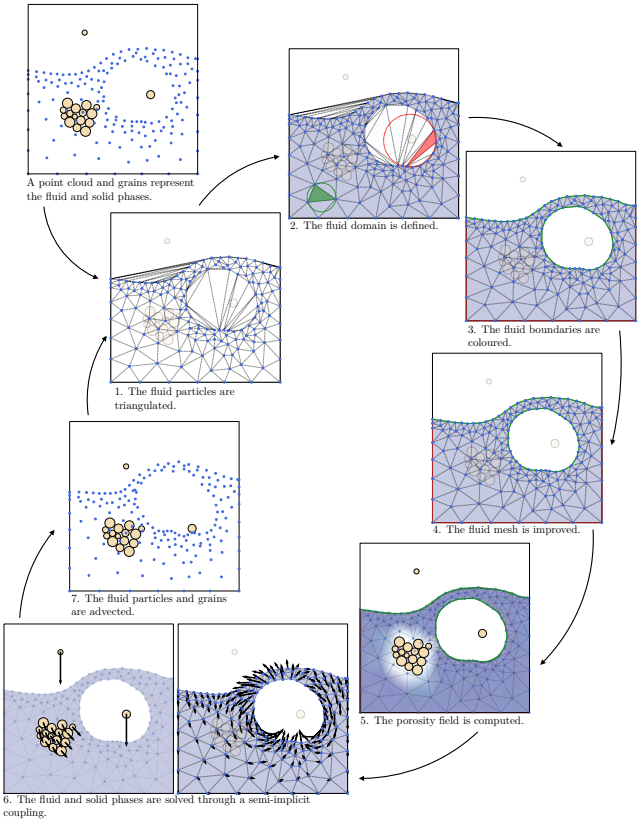

Figure 5.2: A schematic of the algorithm.

circumradii are smaller than a given length. The circumradius of the element R_e must satisfy the following criterion:

$$R_e < \alpha \cdot h(\mathbf{x}). \tag{5.1}$$

where, $h(\mathbf{x})$ is a mesh size field that defines how acceptable circumradii are distributed over the domain. The α-shape of S is the boundary of the α-complex. To capture this boundary, the Delaunay triangulation is first computed and then the circumradii of each element are checked. Any element with a circumradius larger than a given length is removed, as can be seen in Figure 5.2: point 2. The remaining elements form the α-complex, and its boundary is the α-shape of S.

One may wonder why to use the α-shape algorithm instead of the convex hull. By definition, the convex hull is always convex and is therefore not suitable for representing complex boundaries. For example, a simple breaking wave is

not convex, so the convex hull would generate a very poor representation of the free surface.

Boundary colouring

As the domain is highly deformed, boundaries must be detected in order to fulfil the expected boundary conditions imposed by the physical problem such as the no-slip or free-slip conditions on the walls. Boundaries are coloured according to their type. However, the distinction between different boundaries such as walls, moving bodies and free-surfaces is not automatic. Therefore, the boundary edges must be coloured according to which boundary wall they belong. In Figure 5.2: point 3, fluid boundaries belonging to the wall are coloured in red, and free-surfaces in green. Walls are not explicitly meshed are only recognised geometrically by the fluid. An octree data structure is used to enable quick searches and easy computational distances between particles and walls. Once a particle crosses the wall, its velocity is corrected to project it onto the wall. If a boundary edge is sufficiently close to a wall, it is considered to be part of the wall and the boundary conditions are applied. Figure 5.3 illustrates the need to colour complex boundaries.

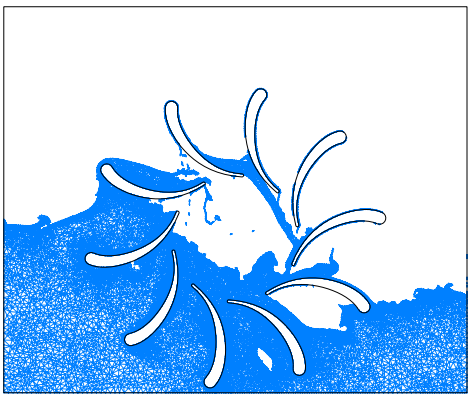

Figure 5.3: Snapshot of a wheel spinning in a flow. The geometry is detected through the α-shape. Colours are associated to each type of boundary conditions, *i.e.* no-slip, free slip, free surface.

Mesh adaptation

The particles are advected by the flow, and the mesh deforms. This can result in poor-quality elements and an inaccurate representation of the free surface since the α-shape criterion depends on the particle distribution and the size

field $h(\mathbf{x})$ which may not be respected. To ensure that the element size is respected, a mesh adaptation is performed. Figure 5.2: point 4, illustrates the mesh adaptation.

In [138], an adaptive mesh refinement technique was proposed for the PFEM to address this challenge based on Chew's constrained Delaunay technique [148]. The size field $h(\mathbf{x})$ is chosen to be highly refined near the free surface and coarser further away from these boundaries. As the mesh is refined close to the free surface, topological changes are captured accurately. This method maintains high-quality elements at all times and ensures a smooth, continuous representation of the free surface. On the other hand, regions far from the free surface become coarser, thereby reducing the computational cost. The solution is interpolated on the newly inserted nodes. Although this can lead to diffusion of the solution, the method has been shown to maintain its accuracy and efficiency.

5.1.2 Resolution

The next step is to solve the governing equations for both phases. The mesh and the boundary conditions are provided by the previous step allowing the conservation equations to be solved. Since the advection is performed by particle displacement, the fluid phase is solved using a Lagrangian formulation,

$$\begin{cases} \boldsymbol{\nabla} \cdot (\varepsilon \boldsymbol{u}) + \boldsymbol{\nabla} \cdot (\phi \boldsymbol{v}) = 0, \\ \rho \varepsilon \partial_t \boldsymbol{u} = -\varepsilon \boldsymbol{\nabla} p + \boldsymbol{\nabla} \cdot (\varepsilon \boldsymbol{\tau}) - \phi \boldsymbol{f}_{\mathrm{d}} + \varepsilon \rho \boldsymbol{g}, \end{cases} \tag{5.2}$$

where ε is the porosity, $\boldsymbol{u}$ the fluid velocity, $\boldsymbol{v}$ the velocity of the solid phase, $\boldsymbol{\sigma}$ the stress tensor, ϕ the volume fraction of the solid phase, $\boldsymbol{f}_{\mathrm{d}}$ the drag force density and $\boldsymbol{g}$ the gravity vector.

Further information on the numerical scheme and the fluid-solid coupling can be found in Chapter 3. Figure 5.2: point 5, illustrates the solid representation in the fluid phase. Figure 5.2: point 6, shows the solution after the resolution step for both the grains and the particles.

5.1.3 Advection

The final step of the algorithm consists in moving particles and grains based on their respective velocities. A second-order scheme is used for the fluid phase and a first-order implicit Euler method is used for the grains. The second-order choice improves the conservation properties near the interfaces as shown by [149].

$$\boldsymbol{x}^{n+1} = \boldsymbol{x}^n + \boldsymbol{u}^{n+1}\Delta t + \frac{\boldsymbol{u}^{n+1} - \boldsymbol{u}^n}{\Delta t}\Delta t^2 \tag{5.3}$$

$$\mathbf{y}^{n+1} = \mathbf{y}^n + \mathbf{v}^{n+1}\Delta t, \tag{5.4}$$

where $\boldsymbol{x}$ and $\mathbf{y}$ are the positions of the fluid and solid particles respectively, $\boldsymbol{u}$ and $\mathbf{v}$ are their respective velocities, and Δt is the time step.

For the fluid phase, an additional step is required to account for solid boundaries. Since the fluid boundaries are defined at the beginning of each time step, it is essential to ensure that the boundary conditions are applied accurately, despite the explicit nature of the position update. In many PFEM approaches for fluid simulations [150, 151], solid boundary particles are fixed to the walls, and define the solid walls to which the boundary conditions are then applied. The approach adopted here allows slip-boundary conditions to be applied straightforwardly along solid walls by considering only fluid particles and representing the walls only geometrically. For particles that are already on a wall at the beginning of the time step, slip boundary conditions can be applied without any difficulty through the finite element formulations. For fluid particles that cross a solid wall during a time step due to the explicit update, Equation (5.3), the velocities of these particles are corrected to project them onto the boundary, as illustrated in Figure 5.4.

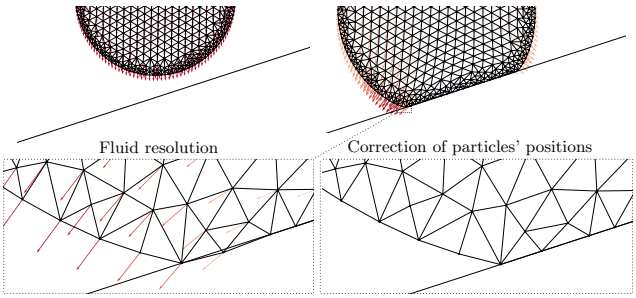

Figure 5.4: The position of the particles that cross a wall during the advection step is corrected by projecting them on the wall.

Both the fluid and the solid phases are treated using an implicit scheme to integrate the velocity over time, therefore no stability conditions arise. In order to ensure an accurate advection of the fluid material points, the fluid time step is chosen as $\Delta t_f = \mathcal{O}\left(\frac{h_{\min}}{\|u_{\max}\|}\right)$. The solid time step is governed by the contact solver which is based on the Non-Smooth Contact Dynamics method. This involves finding the contact impulse iteratively, such that there is no overlap at the end of the time step, without the need for stiffness-based

penalty parameters. At each time step, a contact detection is first performed, then the contact impulse is computed and finally the solid phase is updated. To limit the number of potential contacts in the detection step, the solid time step is chosen as $\Delta t_s = \mathcal{O}\left(\frac{d_{\min}}{\|v_{\max}\|}\right)$. The potential mismatch between the fluid and solid time steps is handled using a sub-stepping strategy for the solid phase. In practice, sub-stepping is only required during the initial stages of the simulation, when the mesh elements are large and the fluid motion is slow. The maximum number of sub-steps observed in the simulations presented in this work is five.

5.2 Granular collapse

The collapse of a granular column into a water basin is investigated to validate the PFEM-DEM method. A dry granular column of height H_0 and width L_0 is placed on a plateform above a water basin at height h_0. Initially held by a gate, the column is released and collapsed under its own weight. This causes a wave to propagate across the surface of the water in the basin. The potential energy stored in the granular column is converted into kinetic energy in the grains and the water. The impact generates a wave that propagates in the direction of the grains. Depending on the impact velocity, the wave can be of different types, ranging from a transient bore wave to a nonlinear transition wave. The aim is to capture these regimes and compare the results with the experimental data from [63].

As the experiments are driven by gravitational effects, the Froude number is chosen as a dimensionless number to characterise the flow. It is defined as the ratio of the characteristic velocity of the grains to the square root of the product of the gravitational acceleration and the initial height of the column.

$$\mathrm{Fr} = \frac{v}{\sqrt{gh}} \tag{5.5}$$

where v is the characteristic velocity of the grains, computed as the equivalent velocity if the grains were accelerating in free fall over a distance corresponding to half of the initial height of the column. This can also be interpreted as the square root of the ratio of the kinetic energy and the potential energy of the system. The characteristic length and velocity used to define the Froude number can then also be used to define dimensionless times and lengths. The wave regime is also characterised by the Froude number because the wave dynamics are driven by the impact of grains on the water bed. However, as suggested in [152], a more appropriate characteristic velocity than the equivalent free-fall velocity, is the maximum horizontal velocity v_f of the granular front.

$$\mathrm{Fr}_f = \frac{v_f}{\sqrt{gh_0}}$$

The main driving force of the wave is the horizontal push of the grains, and not their vertical drop as the columns collapses. The denominator is the characteristic velocity of a bore wave, with h_0 the initial depth of the water basin. The work of [63] has allowed them to distinguish the three regimes based on the front Froude number Fr_f:

- $\mathrm{Fr}_f \lesssim 0.35$: Nonlinear transition wave
- $0.35 \lesssim \mathrm{Fr}_f \lesssim 0.87$: Solitary non-breaking wave
- $0.87 \lesssim \mathrm{Fr}_f$: Transient bore wave

5.2.1 Simulation strategy

Three two-dimensional numerical experiments have been carried out, each corresponding to one of the three regimes. The parameters were chosen to match the experimental setup described in [63]. However, since the grains only move in two dimensions, the impact velocity is higher than in the experiments leading to a higher Froude number. While it would be possible to adjust the friction coefficient to align with the experimental results, the primary objective is to capture the wave regime rather than the precise wave amplitude. Each experiment corresponds to one of the three regimes, correctly capturing the wave dynamics. Table 5.1 presents the numerical Froude numbers for the different cases, compared to the experiment front Froude number from [63].

Experiment	Fr_f (PFEM-DEM)	Fr_f (exp., Sarlin et al.)
1	0.27	0.19
2	0.83	0.65
3	1.93	1.39

Table 5.1: Froude numbers based on the maximum horizontal velocity of the grain column for the different cases, compared with the experimental data.

Initially, the grains are at rest and are held by a gate. The gate can be lifted upwards at a velocity of 1 m/s, releasing the grains into the water bed. The grains have a diameter of 5mm, a density of 2500kg/m^3, and a polydispersity coefficient of 1.2. The friction between grains is modelled by a Coulomb friction law with a coefficient of 0.9. The two-dimensional nature of the simulation imposes grains to be discs instead of spheres. To compensate for this, the void fraction is tuned to match the one of the spheres, as described in 3.2.3. Nevertheless, fluidisation effects are not well captured by this approach. However, these effects are not the main focus of the study, and the model is still able to capture the main dynamics of the flow. The fluid is water with a density 1000kg/m^3 and a viscosity 0.001Pa.s. Free-slip boundary conditions are

imposed on the solid walls, and a free surface condition with surface tension is considered at the water–air interface, with a surface tension coefficient of 0.072N/m. The boundary conditions are summarised as,

$$\begin{cases} \boldsymbol{u} \cdot \boldsymbol{n} = 0, \\ \boldsymbol{t} - (\boldsymbol{t} \cdot \boldsymbol{n})\boldsymbol{n} = \boldsymbol{0}, \end{cases}$$

where $\boldsymbol{n}$ is the outward-facing normal and $\boldsymbol{t} = \boldsymbol{\sigma} \cdot \boldsymbol{n}$ is the Cauchy stress vector. In other words, a zero-velocity condition is imposed in the normal direction, and no stresses are applied in the tangential direction. A free surface is considered at the water–air interface:

$$\boldsymbol{t} = p_0 \boldsymbol{n} - \kappa \gamma \boldsymbol{n},$$

where p_0 is an external atmospheric pressure, κ is the curvature at the free surface, and γ is the surface tension coefficient.

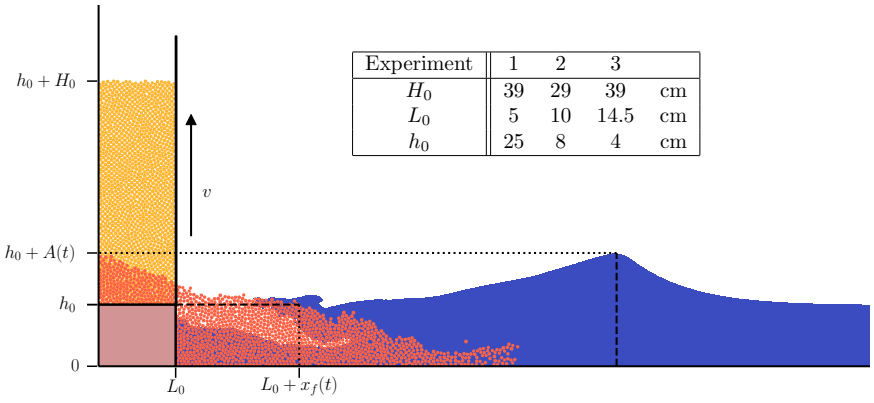

Experiment	1	2	3	
H_0	39	29	39	cm
L_0	5	10	14.5	cm
h_0	25	8	4	cm

Figure 5.5: Granular column collapse test case setup.

5.2.2 One impact, Multiple waves

Three experiments were conducted to capture the three different regimes of the wave formed by the grains impacting on the bassin. Figure 5.5 shows the initial setup of the three experiments, along with the main dimensional parameters. The wave dynamics are captured and compared to the experimental results from [63] for each experiment. The granular front is also tracked, as this is the driving mechanism that generates the wave. In this case, it is defined as the position of the furthest grain at a height of $y = h_0$.

Non linear transition wave

In the first case, the parameters are chosen so that a small front Froude number is expected. The basin is deep and the granular column is thin. This results in only a small amount of the potential energy transferred to the water. The main wave has a low amplitude, resulting in non-negligible dispersive wave trains. This behaviour is said to produce a nonlinear transition wave. As more grains fall into the basin, more perturbations are formed and maintained. The granular front is tracked and compared to the experimental results. As can be seen in Figure 5.6, the granular front reaches a zero value meaning the grains are either fully immersed or still on the initial platform. An initial main wave is generated by the collapse, followed by minor dispersive wave trains. The amplitude of the main wave is small and it does not break. On the other hand, close to the platform, nonlinear effects are visible as the grains continue to fall, resulting in chaotic motion of the grains and the water.

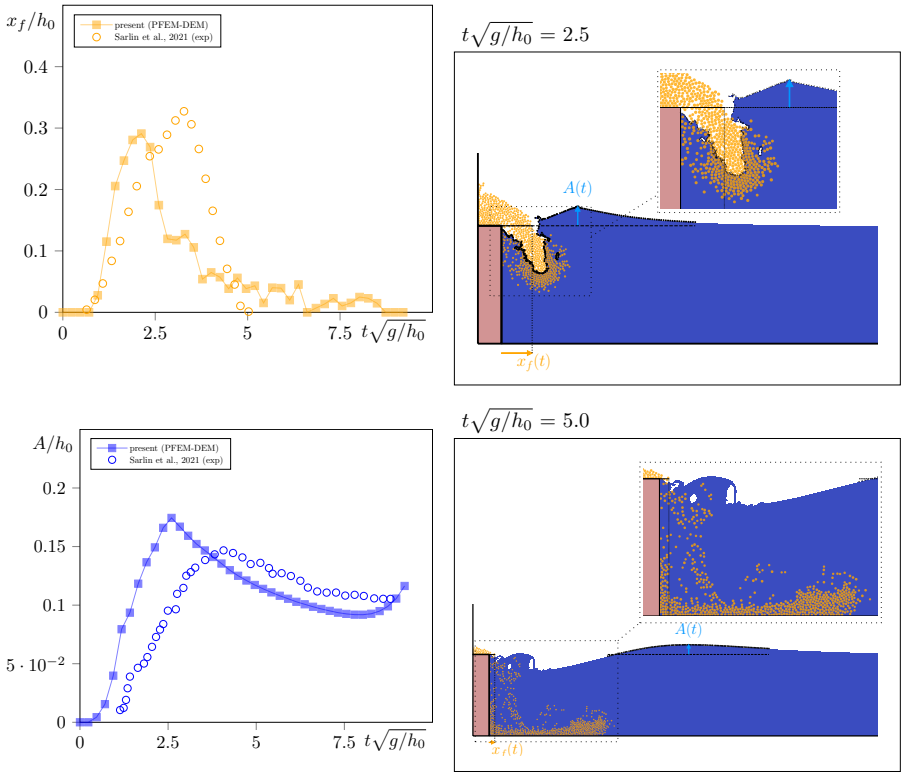

Figure 5.6: Granular collapse: case 1. Non linear transition wave is generated at low front Froude number.

Solitary non-breaking wave

In the second case, the Froude number is increased in order to produce a solitary, non-breaking wave. The wave generated by the grains has a higher amplitude. To reach this regime, the depth is first decreased and then the shape of the column is changed so that it is thicker than in the previous case. Upon impact, a solitary wave is generated and propagates. Figure 5.7 shows the snapshots of the flow at different times during the second experiment as well as the evolution of the wave amplitude and the position of the granular front. The wave amplitude remains close to a constant value until the wave rolls over itself and breaks. The granular front also increases until it reaches a plateau value. As the grains do not expel all the water, they become submerged in the fluid.

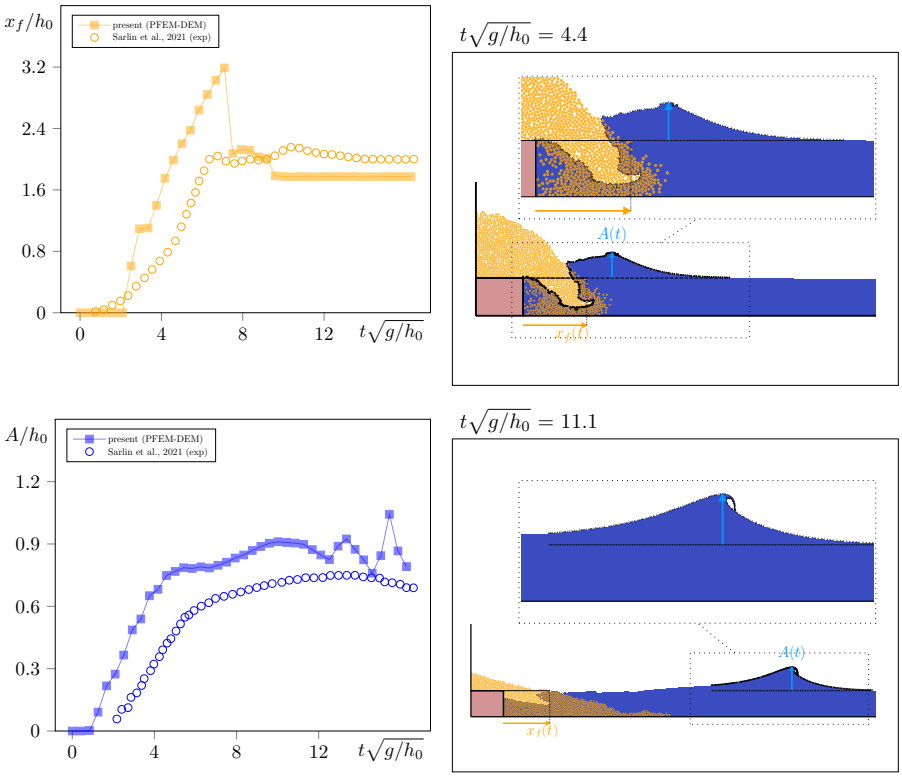

Figure 5.7: Granular collapse: case 2. Solitary wave is observed at intermediate front Froude number.

Transient bore wave

In the last conducted experiment, the front Froude number is increased in order to generate a bore wave. For a large transfer of energy from the grains to the water, the free surface deforms into a shape resembling a step function. This behaviour is characteristic of a bore wave. Figure 5.8 shows snapshots of the flow at different times during the third experiment. Initially, the generated wave has a high amplitude and a bore wave forms. As the wave propagates, it rolls over itself and breaks into a chaotic motion. The grains expel such a significant amount of water such that some of the grains remain dry. The granular front increases during the fall, reaching a maximum value. As the granular deposit is stable, the front maintains its maximum value. Two internal friction angles can be observed in the grains, one for the dry grains, and one for the submerged grains.

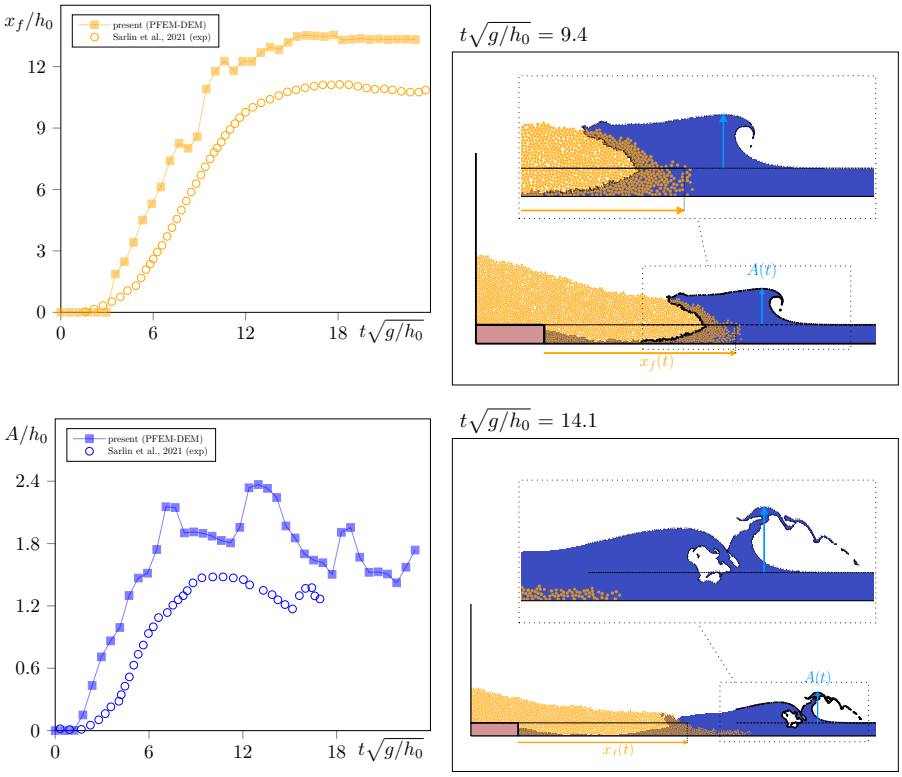

Figure 5.8: Granular collapse: case 3. A high front Froude Number, the collapse generates a transient bore wave.

5.2.3 Discussion

Qualitatively, the three regimes are accurately captured by the numerical simulations. However, disparities are observed in the granular front position, but this can be attributed to the uncertainty in the measurement of the granular front position. To estimate the granular front, the furthest grain at a height of $y = h_0$ is chosen, as shown in Figure 5.5. The aim is to compute the maximum horizontal velocity of the grains at the free surface, responsible for generating the impulse wave, this measurement is the most relevant option. However, this approach does not produce consistent results when the grains are fully submerged in the fluid, because the granular front is no longer visible. If one is only interested in computing the maximum position reached by the grains inside the flow, a more robust alternative would be to take the runout distance of the avalanche. This is defined as the position of the farthest grain still connected to the contact network [60]. While the order of magnitude of the wave amplitude is captured well, the amplitude is slightly overestimated. This can be attributed to grains having a higher velocity in the numerical simulations, since they are not subject to the same friction as in the physical experiments. While the three regimes are correctly captured qualitatively and respect the bounds, there are some discrepancies with the obtained Froude numbers. These differences can be explained by various factors: three-dimensional effects, the parametrisation of the grains' friction and the method used to measure the granular front position and velocity. The obtained values for Fr_f from the numerical setups are presented in table 5.1. While the results do not exactly match those of the experiments, the regimes are still correctly detected within the bounds proposed by [63].

5.3 A Tsunami at Lituya bay

To investigate the robustness and accuracy of the proposed model, a realistic case, the Lituya Bay landslide and tsunami, is studied. On 10 July 1958, an earthquake along the Fairweather fault triggered a massive landslide above Lituya Bay in Alaska. The loose rock slid downhill and hit the waters of Lituya Bay, creating a 60 metres wave that reached heights of over 500 metres on the opposite shore. The tsunami resulted in human casualties. As mountains become increasingly unstable due to climate change, such events are expected to become more frequent. Understanding and predicting the impact of such events is crucial for risk mitigation. The numerical method presented here is a suitable tool for simulating and analysing such phenomena, providing a detailed description of both the grain dynamics and the wave motion. To quantitatively compare the results with those of the real event, the numerical results are compared with the experimental results of [64]. In their study, a 1:675 scale experiment of the Lituya Bay landslide and tsunami was carried

out in order to better quantify the event.

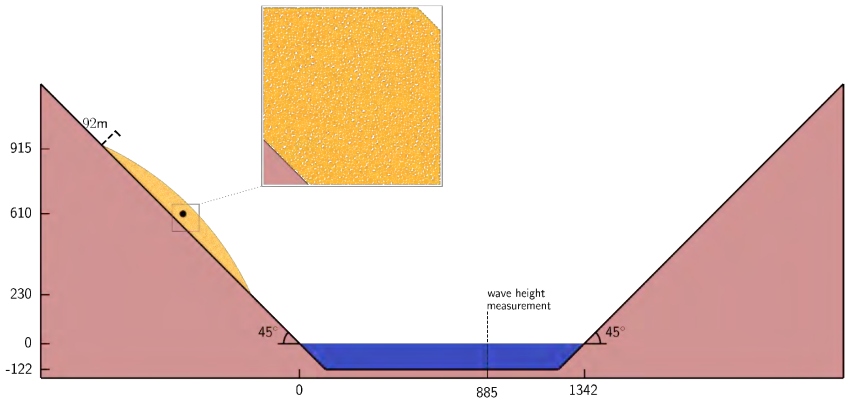

Figure 5.9: Lituya bay landslide and tsunami setup.

5.3.1 Numerical strategy

The bay is modelled as a two-dimensional domain, with the rocks represented by a set of discrete grains and the water by a continuous fluid. The experimental setup is based on the scale model of [64], with a scale of 1 to 675. Figure 5.9 shows the setup. According to the estimated amount of rock that was torn from the hill, a mass of grains 970 m long and 92 m thick, is positioned 230 m above the water level. This gives a total mass per unit thickness of 98.5×10^3 t/m. The grains have a density of 2.64 t/m^3, and a polydispersity ratio of 3 which allows the bulk to be more compact. The average grain radius is set to 1.35 m, in order to match the 2 mm radius used in [64]. A space-filling algorithm, as described in 3, is used to generate the initial grains configuration. This results in a total of 27960 grains. The friction coefficient between the grains and with the walls is set to $\mu = 0.93$, which corresponds to an effective internal friction angle of 43°. The simulated water bed is a cross-section of the Gilbert Inlet in the Lituya Bay, with a depth of 122 m and a total length of 1342 m. Both shores rise at an angle of 45°.

The Froude number is the relevant dimensionless number to relate the impact of the grains to the potential energy stored in the water bed. Taking the mean velocity v_g of the grains upon impact with the water as estimated at 110 m/s in [64], and the water depth of the bay as 122 m, the resulting front Froude number is equal to

$$\mathrm{Fr} = \frac{v_g}{\sqrt{gh}} = 3.18.$$

5.3.2 Tsunami Wave propagation

When the sliding rocks reach the water, they transfer a large amount of kinetic energy to it. This results in a wave that propagates across the bay. Figure 5.10 shows snapshots of the wave propagation at different times. According to the wave analysis of [63] and the front Froude number, the wave is expected to resemble a bore wave. This is confirmed by the numerical results as seen in the snapshots.

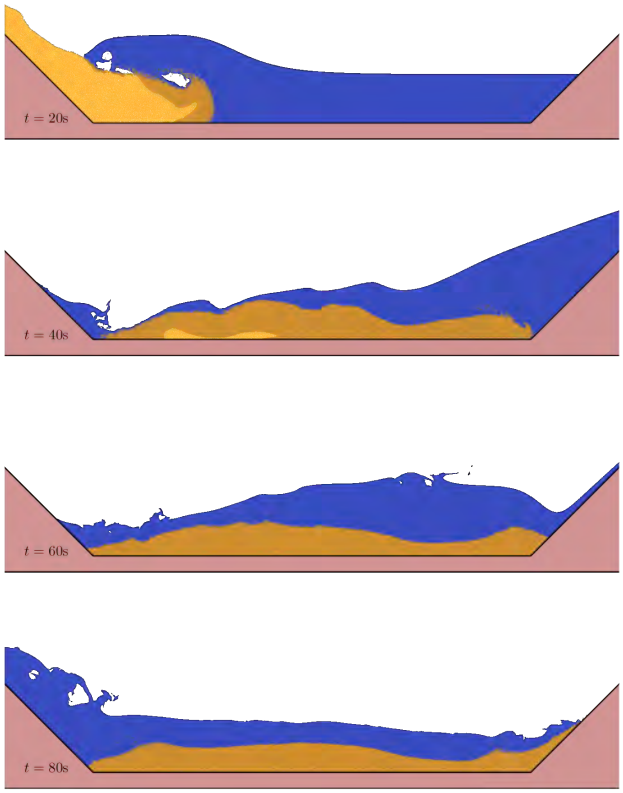

Figure 5.10: Snapshots of the Lituya bay landslide and the wave generated by the fallen rocks at time 20, 40, 60 and 80s.

The wave does not have enough time to break as it crosses the bay and hits the opposite shore. The maximal height reached by the wave is tracked in Figure 5.11. On the opposite shore, a thin layer of water remains attached to the shore up to a height of 750m. This value is an overestimation as it assumes

that the water slides freely along the boundary. However, the results show that at a height of 500m, the water still has enough inertia to cause damage, as was observed in the Lituya Bay event. When the wave impacts the shore, it also reflects, leading to a sloshing phenomenon. This can be seen as when a second wave with less amplitude hits the shore. Rocks are transported throughout the whole domain and settle across the entire bay. The largest hills form close to the initial impact zone and close to the opposite shore.

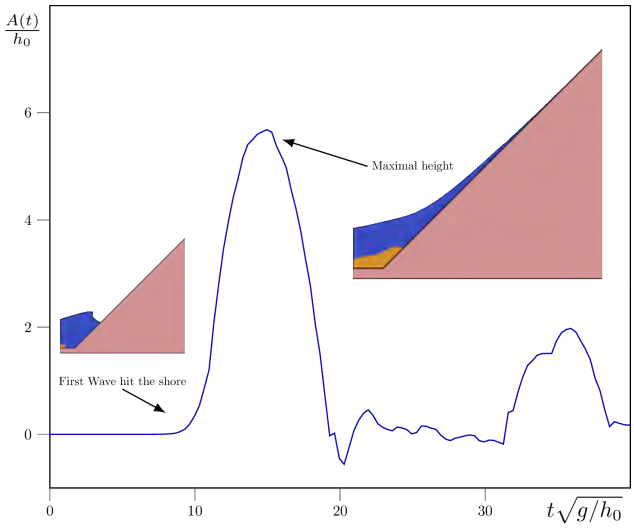

Figure 5.11: Evolution of the wave amplitude on the opposite shore. Dimensionless height is defined by the initial depth h_0 and the gravitational accelerating is used to define a dimensionless time.

Once the wave has fallen back onto the opposite shore, reflective waves are generated. Figure 5.12 compares the wave amplitude at a position of 885m from the initial shore to the experimental data from [64]. The Lagrangian formulation accurately captures the main trends in the wave dynamics. Dimensionless height and time are computed using the initial water depth h_0 as the reference height and the gravitational acceleration g.

Conclusion

A new coupling has been developed for studying immersed granular flows with free surfaces undergoing large deformations. The granular phase is modelled using the Discrete Element Method (DEM), while the fluid is treated using a Lagrangian formulation based on the Particle Finite Element Method (PFEM).

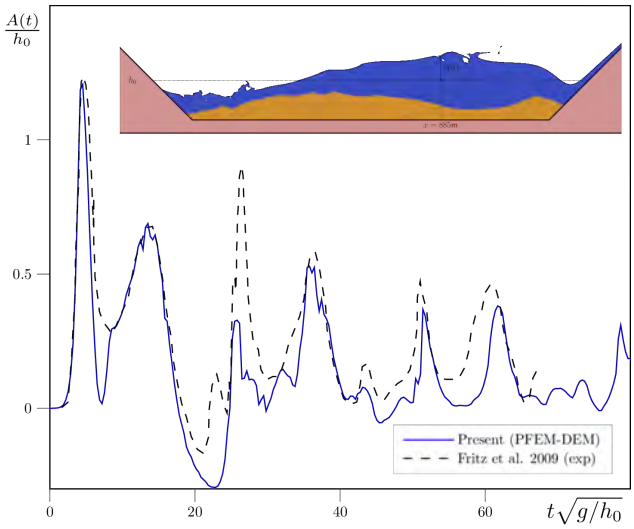

Figure 5.12: Wave height evolution at $x = 885$m. Numerical results, the continuous blue line, is compared to the experimental results from [64], dotted black curve. The dimensionless height and time are computed using the initial bathymetry h_0 as the reference height and g the gravitational acceleration.

This work focuses on presenting the PFEM–DEM coupling strategy and demonstrating its applicability to complex free-surface granular flows.

To validate the model and highlight its capabilities, two key test cases are considered: the collapse of a granular column [63] and the Lituya Bay landslide [64]. In both cases, the interaction between the granular material and the fluid generates free surface waves. Accurate tracking of the evolving interface and wave dynamics is enabled by the Lagrangian treatment of the fluid phase.

A crucial feature of the CFD–DEM solver is its robustness with respect to mesh resolution; the mesh does not need to be tied to grain size. This enables the straightforward integration of the PFEM strategy, which would otherwise require maintaining a coarse mesh near the grains and could compromise the accuracy of the free-surface representation. Refinement of the mesh near the fluid–air interface is essential for accurately capturing wave formation and propagation, as it provides high spatial resolution where it is most needed.

The granular collapse is used as a benchmark to validate wave generation. The wave regime is characterised using the front Froude number, and three physical experiments are reproduced using the numerical model. In all cases, the observed wave patterns align with theoretical expectations, thus confirming the model's predictive capability.

The Lituya Bay landslide and tsunami are then simulated to demonstrate

the model's potential for addressing large-scale natural hazards. Despite the phenomenon's complexity, a quasi-2D simulation using the proposed PFEM–DEM model successfully captures its key features. The simulated wave dynamics show strong agreement with available experimental data, including the extreme run-up height of around 500 metres, which is consistent with historical observations [64].

The results demonstrate the potential of PFEM–DEM coupling method for studying immersed granular flows involving significant deformations and complex fluid–solid interactions. The model is both accurate and robust, even when restricted to two-dimensional simulations. This restriction is purely a matter of computational cost, and the approach can be fully extended to three dimensions. However, one notable limitation of the current implementation is the absence of mass conservation. The advection scheme used to move the Lagrangian particles does not strictly preserve volume. Furthermore, the mesh generation process may also introduce additional volume errors. Addressing this limitation would be a natural extension of the present work, enabling high-fidelity simulations with improved conservation properties.

CHAPTER 6

Conclusion

Granular flows are ubiquitous in both natural and industrial processes. From avalanches and landslides to pharmaceutical manufacturing and energy storage systems, the behaviour of granular materials plays a central role in the dynamics of many physical systems. Their complex rheology, which combines solid-like, liquid-like, and gas-like behaviours, presents significant challenges for both experimental investigation and numerical simulation. Granular flows span a wide range of regimes, from dilute particle suspensions to dense, friction-dominated packings. Depending on the flow regime and application, different modelling strategies have been developed. Continuum approaches, often based on empirical constitutive laws, are well-suited for large-scale geophysical flows but struggle with phenomena at the grain scale [11]. On the other hand, discrete methods such as the Discrete Element Method (DEM) [36, 73] allow for detailed tracking of individual particles and their interactions but become computationally expensive for large systems.

Hybrid approaches attempt to bridge the gap between scale and fidelity, leveraging the strengths of both continuum and discrete descriptions [48, 13]. Coupling these models with fluid phases adds a further layer of complexity, particularly when the interaction between the granular material and the fluid plays a critical role in the system's evolution. The choice of a numerical method often depends on the resolution desired, computational constraints, and the physics of interest. Fully resolved simulations can capture intricate fluid–particle interactions but are limited to small systems due to computational costs. Unresolved

models offer greater scalability but require careful treatment of the coupling between phases to preserve accuracy and stability. In this work, we propose a semi-resolved, non-conformal coupling strategy between a finite element representation of the fluid and a discrete element model for the granular phase. The fluid is captured using the Volume-Averaged Navier–Stokes equations solved on a mesh that does not conform to the particle boundaries. This non-conformal approach reduces the computational complexity while allowing for sufficient resolution of the flow features of interest. The grains, modelled as discrete entities, interact with the fluid through a carefully designed coupling mechanism that accounts for the momentum exchange between the phases. The spatial representation of the particles is handled using overlap-based techniques, enabling for a smoother and more physically consistent interaction with the fluid field, even when the mesh is finer than the particle scale. This framework enables the simulation of a broad class of problems—from unresolved, continuum-scale flows to semi-resolved configurations where particle-scale effects are partially captured. It provides a flexible and scalable alternative to fully resolved methods, while ensuring physical accuracy and numerical stability. Our approach is also well suited for applications involving large deformations, free surfaces, and complex geometries by decoupling the mesh resolution from the particle size, we unlock the possibility to simulate large systems while still capturing essential micro-scale effects.

Numerical experiments presented in this work, such as Rayleigh–Taylor instabilities, the digging of a water droplet demonstrate the robustness and versatility of the proposed method. Moreover, our coupling strategy is compatible with advanced Lagrangian solvers such as the Particle Finite Element Method (PFEM), allowing us to explore phenomena such as landslide-induced wave generation. In conclusion, granular flows remain a rich and challenging field of study with wide-ranging applications. Our contribution lies in the development of a computationally efficient and physically accurate framework that uses a non-conformal fluid representation coupled with discrete grains to explore complex fluid–solid interactions. This approach paves the way for scalable and adaptable simulations across a wide spectrum of granular flow problems.

Contents

6.1 My Contributions

This thesis is the result of a long journey that began at UCLouvain, in collaboration with the LMGC laboratory in Montpellier. When I first started, I believed that all PhD projects naturally sit at the edge of current knowledge – but the more I learned, the more I realised how vast the unknown truly is. It all started with a simple question: *How can we model the motion of a grain when its size becomes comparable to the fluid discretisation?*. One question led to another, and I soon found myself immersed in the world of granular flows. Along the way, I explored the complexities of non-smooth dynamics, the challenges of numerical methods, and the elegance of mathematical modelling. From studying heat transfer in suspensions, to water intrusion in a hot granular bed, and eventually to landslide simulations, I had the chance to explore a wide range of topics and applications. I was fortunate to work within an institute that values collaboration and interdisciplinary research, which gave me the opportunity to explore different approaches and perspectives. On more than one occasion, the answer to a question came while investigating something entirely different. Here, I will summarise the main findings of my work and highlight the key contributions made during this journey.

The first step in my journey was to extend the model to be able to **reach arbitrary mesh size**. I had to learn about the physics of granular materials, the challenges involved in simulating them, and the limitations of existing models. For computational convenience, a non-conformal approach known as the Volume-Averaged Navier–Stokes (VANS) equations had previously been chosen [48]. This approach captures the essential physics of granular flows while avoiding the complexity of fully resolved simulations. However, the implementation breaks down when the grain size becomes large compared to the fluid discretisation, which is a major limitation for highly polydisperse systems or for capturing complex geometries. Additionally, instability issues arise from large oscillations in the continuity equation, due to the chosen numerical scheme. These issues were not inherent to the model itself, but from its discretisation. The challenge was to find a way to overcome them. Using a novel overlap-wise grain representation combined with a semi-implicit time integration scheme, we were able to solve this problem. The improved model was validated across a wide range of test cases: from unresolved simulations of granular Rayleigh-Taylor instability [97] to resolved simulations of a single cylinder sedimentation in fluid [101].

In the second phase of the work, **heat transfer in suspensions** was investigated. The goal was to gain an understanding of the digging process observed in experiments by [61], where water droplet forms a cavity into a hot granular bed. To achieve this, we first needed to understand the physics of heat transfer in granular suspensions and how to incorporate this into a volume-averaged framework. We proposed a new correlation to model forced convection in an

assembly of grains immersed in fluid, which was validated against experimental data and a benchmark testcase from the literature [116]. Next came the challenge of modelling water bubble intrusion into a hot granular bed surrounded by air. As water evaporates, vapor forms, wets particles, and creates local interaction forces. This effect was modelled and incorporated into a Non-Smooth Contact Dynamics (NSCD) framework. The motion of the bubble itself was modelled using an Arbitrary Lagrangian–Eulerian (ALE) approach, allowing us to capture its deformation and movement. Our two-dimensional simulations were able to reproduce the three main phases of the digging process observed experimentally. However, the model overestimated the temperature required to initiate digging. We have proposed two hypotheses to explain this discrepancy: (1) the reduced grain mobility in two dimensions, and (2) the simplified bubble shape used in the simulations.

The final part of this thesis aimed to overcome the domain deformation limitation and model **immersed granular flows with free surfaces**. We turned to the Particle Finite Element Method (PFEM), which enables mesh adaptivity and domain deformation [43, 62]. Unlike the VANS equations, the PFEM does not require any invasive changes to be made to the fluid solver; only the advection term needs to be removed, as it is inherently accounted for by mesh motion. Both fluid and solid phases are treated in a Lagrangian fashion, allowing us to naturally capture free surfaces, bubble motion, and large deformations. Moreover, since the fluid model is now stable regardless of mesh size, mesh refinement can be used freely, without introducing numerical instabilities. To validate the model, we simulated several test cases, including a dam break (not shown in the thesis), granular collapse [63], and the tsunami wave generated by the landslide in Lituya Bay [64]. All simulations reproduced the experiments both qualitatively and quantitatively. This further demonstrated the versatility and robustness of the model. However, the model still lacks mass conservation due to the advection scheme used to move the Lagrangian particles and the remeshing process.

This marks the end of the journey. I hope that this work inspires future research into granular flows, contributing to a better understanding of the complex phenomena that govern them. The versatility of the models developed here, and the wide range of applications explored, highlight their potential for future investigations. In the next section, I'll outline some of the paths that could be explored going forward.

6.2 Final Words, Future Paths

This work, like previous ones, opens up several avenues for future research. So far, the fluid model coupling presented in this thesis has only been limited to two-dimensional simulations of cylindrical grains. There are two main reasons

for this choice: (1) the computational cost of three-dimensional simulations, and (2) the difficulty to compute overlap centroids.

The first extension would be to extend the **model to three dimensions**. Once the third dimension is considered, the number of degrees of freedom increases significantly as the number of mesh nodes increases and an additional degree of freedom for each node is added. However, when considering fluidisation experiments, the third dimension should not be neglected since it restricts the grains motion to be in the same plane. Taking the third dimension into account would allow to capture the full dynamics of the system. With the improvement of linear solver and GPU computing, the computational cost of these simulations is becoming less of a concern. A second reason is the challenge of computing overlap centroids. While computing the centroid of the overlap between a disc and a triangle can be achieved at a low computational cost, to do the same for a sphere and a tetrahedron is much more complex. To achieve this, the overlap volume should be divided into simpler shapes such as cone or wedges. The geometric decomposition proposed by Strobl et al. [153] seems to be a good candidate for this task. This would allow to compute the centroid of the overlap volume and to compute the forces acting on the grains using the same approach as in two-dimensional simulations.

A second extension would be to extend the model to include model **grains as polygons or polyhedra**. This would allow to simulate more complex grain shapes or to avoid the use of an exact sphere representation. Two steps are required to achieve this: (1) the implementation of the contact dynamics for polygons/polyhedra, and (2) the implementation of the overlap-wise model for polygons/polyhedra. The contacts dynamics have already been implemented for polygons and polyhedra in the NSCD framework in different sofwares such as *LMGC* and is only a matter of time before they are implemented in the current MigFlow code. The implementation of the overlap of polygons and polyhedra over a mesh can be achieved using the Weiler-Atherton clip algorithm [154]. A first step has already been achieved as shown in Figure 6.1, where a polygonal representation of a non-spherical grain is shown. Additionally, the absence of rotation in the fluid–grain coupling currently limits the model to non-rotating grains which may not accurately represent all physical scenarios. Taking into account these effects would require appropriate constitutive laws and numerical methods to handle the additional complexity.

A third path for future research is investigating **bubbles into granular flows**. The Particle Finite Element Method is well suited to this task, as it enables the motion of bubbles to be captured at a reasonable computational cost and has already been validated for this purpose [138]. Some questions remain open such as the impact of grains on the bubble surface tension. The goal would be either to simulate magma intrusion at fine scale with crystal rocks modelled as grains, gas bubbles using the PFEM approach and the fluid modeled using the VANS equations or the formation of pockmarks resulting

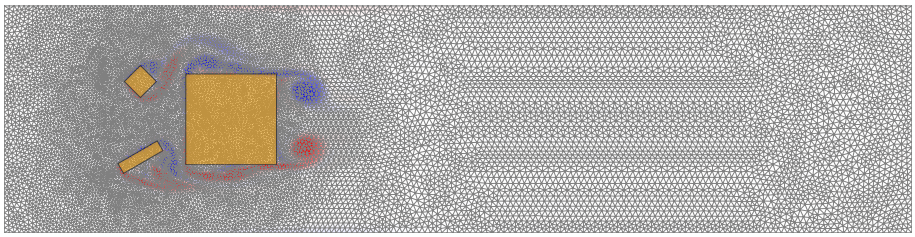

Figure 6.1: Example of a polygonal representation for a non-spherical grain. Vorticity is visualized in colour, with the underlying mesh shown in gray.

from gas seepage through the sedimentary layer[155].

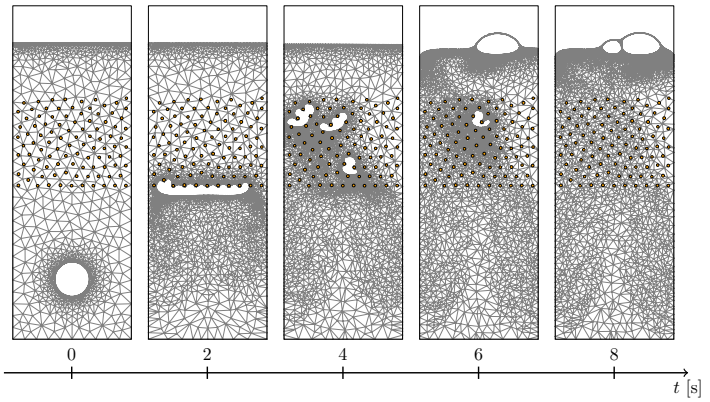

Figure 6.2: Air bubble reaching the surface of a water bassin with fixed grains.

Finally, a fourth path would be to investigate the **convergence** of the scheme. As pointed out in Chapter 3, the Volume-Averaged Navier-Stokes equations are similar to other resolved non-conform Penalization method. One of these methods has caught our attention, the CUT-FEM, as its convergence has been studied in details [156, 157]. The discretised form of the equations is similar to the one used in the VANS equations at the differences that some jump terms are missing in the VANS equations. Those terms are responsible for the convergence of the scheme. We have already started investigating the convergence of the heat equation using an overlap-wise representation of the grains with the CUT-FEM discretisation and were able to obtain the expected convergence rate on a test case. Figure 6.3 shows the convergence of the heat equation using the CUT-FEM discretisation, based on unfitted Nitsche's method, compared to conformal Nitsche's method, both with linear shape functions. The $\mathcal{H}^0$ norm is computed over the physical domain, not the computational one,

and a slope of 2 is observed. For the $\mathcal{H}_1$ norm, a slope of 1 is observed.

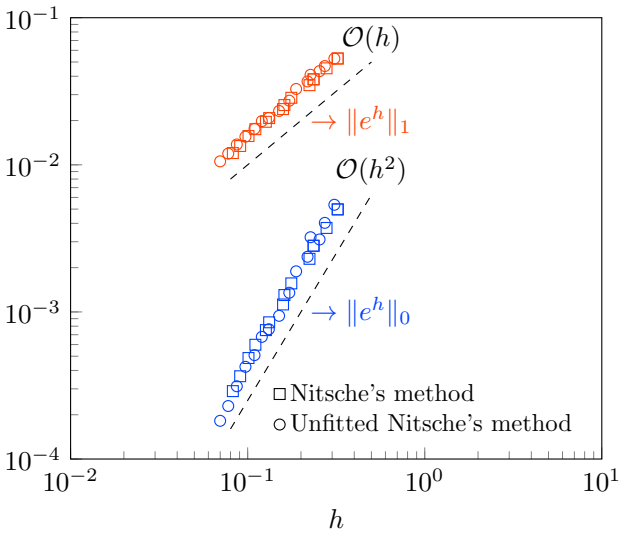

Figure 6.3: Convergence of the heat equation using the CUT-FEM discretisation.

The next step is to implement the Navier-Stokes equations resolution within the CUT-FEM framework, validate the constitutive law and check the convergence of the scheme. The goal would be to show an equivalence between the Volume-Averaged Navier-Stokes equations and the CUT-FEM discretisation of the Navier-Stokes equations. If successful, the convergence rate towards the Navier-Stokes equations from the VANS equations would be naturally shown.

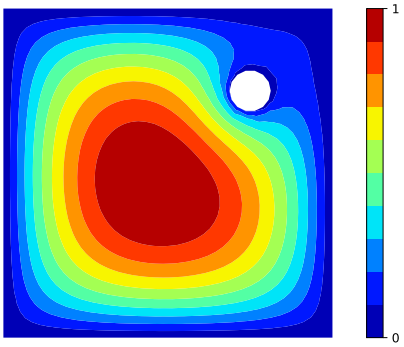

(a) Convergence of the heat equation using a conform discretisation.

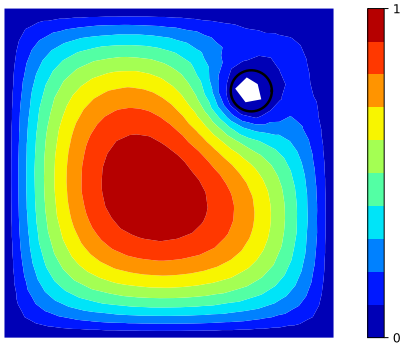

(b) Convergence of the heat equations using the CUT-FEM representation.

Bibliography

[1] Jan K Marzinek, Roland G Huber, and Peter J Bond. "Multiscale modelling and simulation of viruses". In: *Current opinion in structural biology* 61 (2020), pp. 146–152. DOI: 10.1016/j.sbi.2019.12.019.

[2] Johannes Voß and Raphael Wittkowski. "On the shape-dependent propulsion of nano and microparticles by traveling ultrasound waves". In: *Nanoscale Advances* 2.9 (2020), pp. 3890–3899. DOI: 10.1039/D0NA00099J.

[3] Yiwu Zong and Kun Zhao. "Manipulation of self-assembled structures by shape-designed polygonal colloids in 2D". In: *Current Opinion in Solid State and Materials Science* 26.6 (2022), p. 101022.

[4] Xi Luo et al. "A review of analytical methods and models used in atmospheric microplastic research". In: *Science of the Total Environment* 828 (2022), p. 154487.

[5] Jonathan B Freund. "Numerical simulation of flowing blood cells". In: *Annual review of fluid mechanics* 46.1 (2014), pp. 67–95.

[6] Guilhem Mollon and Jidong Zhao. "Generating realistic 3D sand particles using Fourier descriptors". In: *Granular Matter* 15 (2013), pp. 95–108.

[7] Guillaume Piton et al. "Debris flows, boulders and constrictions: a simple framework for modeling jamming, and its consequences on outflow". In: *Journal of Geophysical Research: Earth Surface* 127.5 (2022).

[8] Thomas Rackow et al. "A simulation of small to giant A ntarctic iceberg evolution: Differential impact on climatology estimates". In: *Journal of Geophysical Research: Oceans* 122.4 (2017), pp. 3170–3190.

[9] Fabio Ferrari, Michèle Lavagna, and Emmanuel Blazquez. "A parallel-GPU code for asteroid aggregation problems with angular particles". In: *Monthly Notices of the Royal Astronomical Society* 492.1 (2020), pp. 749–761.

[10] Yoël Forterre and Olivier Pouliquen. "Physics of particulate flows: From sand avalanche to active suspensions in plants". In: *Comptes Rendus. Physique* 19.5 (2018), pp. 271–284.

[11] Élisabeth Guazzelli and Olivier Pouliquen. "Rheology of dense granular suspensions". In: *Journal of Fluid Mechanics* 852 (2018), P1.

[12] Farhang Radjai, Frédéric Dubois, et al. *Modélisation numérique discrète des matériaux granulaires*. Hermès science, 2010.

[13] Jidong Zhao, Shiwei Zhao, and Stefan Luding. "The role of particle shape in computational modelling of granular matter". In: *Nature Reviews Physics* 5.9 (2023), pp. 505–525.

[14] Brian Miller, Corey O'Hern, and RP Behringer. "Stress fluctuations for continuously sheared granular materials". In: *Physical Review Letters* 77.15 (1996), p. 3110.

[15] Daniel Howell, Robert P Behringer, and Christian Veje. "Stress fluctuations in a 2D granular Couette experiment: a continuous transition". In: *Physical Review Letters* 82.26 (1999), p. 5241.

[16] CT Veje, Daniel W Howell, and RP Behringer. "Kinematics of a two-dimensional granular Couette experiment at the transition to shearing". In: *Physical Review E* 59.1 (1999), p. 739.

[17] Lhassan Amarsid et al. "Viscoinertial regime of immersed granular flows". In: *Physical Review E* 96.1 (2017), p. 012901.

[18] Stany Gallier et al. "Rheology of Sheared Suspensions of Rough Frictional Particles". In: *Journal of Fluid Mechanics* 757 (Oct. 2014), pp. 514–549. ISSN: 0022-1120, 1469-7645. DOI: 10.1017/jfm.2014.507.

[19] François Boyer, Élisabeth Guazzelli, and Olivier Pouliquen. "Unifying suspension and granular rheology". In: *Physical review letters* 107.18 (2011), p. 188301.

[20] Thanh Trung Vo et al. "Additive rheology of complex granular flows". In: *Nature communications* 11.1 (2020), p. 1476.

[21] David Cantor et al. "Rheology and structure of polydisperse three-dimensional packings of spheres". In: *Physical Review E* 98.5 (2018), p. 052910.

[22] George Gabriel Stokes et al. "On the effect of the internal friction of fluids on the motion of pendulums". In: (1851).

[23] J. M. DallaValle and Alexander Klemin. *Micromeritics: The Technology of the Particles*. New York ; Chicago: Pitman Publishing Corporation, 1943.

[24] R. Di Felice. "The Voidage Function for Fluid-Particle Interaction Systems". In: *International Journal of Multiphase Flow* 20.1 (Feb. 1994), pp. 153–159. ISSN: 0301-9322. DOI: 10.1016/0301-9322(94)90011-6.

[25] DA Huerta et al. "Archimedes' principle in fluidized granular systems". In: *Physical Review E—Statistical, Nonlinear, and Soft Matter Physics* 72.3 (2005), p. 031307.

[26] Heinrich G Magnus. *Über die Abweichung der Geschosse*. Druckerei der Königlichen Akademie der Wissenschaften, 1853.

[27] Thorsten Kray, Jörg Franke, and Wolfram Frank. "Magnus effect on a rotating sphere at high Reynolds numbers". In: *Journal of wind engineering and industrial aerodynamics* 110 (2012), pp. 1–9.

[28] Philip Geoffrey Saffman. "The lift on a small sphere in a slow shear flow". In: *Journal of fluid mechanics* 22.2 (1965), pp. 385–400.

[29] Xu Zheng and Zhanhua Silber-Li. "The influence of Saffman lift force on nanoparticle concentration distribution near a wall". In: *Applied physics letters* 95.12 (2009).

[30] Christopher Earls Brennen. "A review of added mass and fluid inertial forces". In: *Naval Civil Engineering Laboratory* (1982).

[31] Louis Landweber and Ali Shahshahan. "Added masses and forces on two bodies approaching central impact in an inviscid fluid". In: *Journal of ship research* 36.02 (1992), pp. 99–122.

[32] Alfred Barnard Basset. *A treatise on hydrodynamics: with numerous examples*. Vol. 2. Deighton, Bell and Company, 1888.

[33] Patricio A Moreno-Casas and Fabian A Bombardelli. "Computation of the Basset force: recent advances and environmental flow applications". In: *Environmental Fluid Mechanics* 16 (2016), pp. 193–208.

[34] GK Batchelor and JT0246 Green. "The determination of the bulk stress in a suspension of spherical particles to order c2". In: *Journal of Fluid Mechanics* 56.3 (1972), pp. 401–427.

[35] Irvin M Krieger and Thomas J Dougherty. "A mechanism for non-Newtonian flow in suspensions of rigid spheres". In: *Transactions of the Society of Rheology* 3.1 (1959), pp. 137–152.

[36] Peter A Cundall and Otto DL Strack. "A discrete numerical model for granular assemblies". In: *geotechnique* 29.1 (1979), pp. 47–65.

[37] Nicolin Govender. "Study on the effect of grain morphology on shear strength in granular materials via GPU based discrete element method simulations". In: *Powder Technology* 387 (2021), pp. 336–347.

[38] Frédéric Dubois, Vincent Acary, and Michel Jean. "The Contact Dynamics Method: A Nonsmooth Story". In: *Comptes Rendus Mécanique*. The Legacy of Jean-Jacques Moreau in Mechanics / L'héritage de Jean-Jacques Moreau En Mécanique 346.3 (Mar. 2018), pp. 247–262. ISSN: 1631-0721. DOI: 10.1016/j.crme.2017.12.009.

[39] Hammad Mazhar et al. "Using Nesterov's method to accelerate multibody dynamics with friction and contact". In: *ACM Transactions on Graphics (TOG)* 34.3 (2015), pp. 1–14.

[40] Franck Jourdan, Pierre Alart, and Michel Jean. "A Gauss-Seidel like algorithm to solve frictional contact problems". In: *Computer methods in applied mechanics and engineering* 155.1-2 (1998), pp. 31–47.

[41] N Bessonov et al. "Numerical Modelling of Cell Distribution in Blood-Flow". In: *Mathematical Modelling of Natural Phenomena* 9.6 (2014), pp. 69–84.

[42] Thomas JR Hughes, Wing Kam Liu, and Thomas K Zimmermann. "Lagrangian-Eulerian finite element formulation for incompressible viscous flows". In: *Computer methods in applied mechanics and engineering* 29.3 (1981), pp. 329–349.

[43] Eugenio Oñate et al. "The particle finite element method—an overview". In: *International Journal of Computational Methods* 1.02 (2004), pp. 267–307.

[44] C.S. Peskin. "Numerical analysis of blood flow in the heart". In: *Journal of computational physics* 25.3 (1977), pp. 220–252.

[45] Erik Burman and Miguel A Fernández. "An unfitted Nitsche method for incompressible fluid–structure interaction using overlapping meshes". In: *Computer Methods in Applied Mechanics and Engineering* 279 (2014), pp. 497–514.

[46] Joseph J Monaghan. "Smoothed particle hydrodynamics and its diverse applications". In: *Annual Review of Fluid Mechanics* 44.1 (2012), pp. 323–346.

[47] AA Mohamad. *Lattice boltzmann method*. Vol. 70. Springer, 2011.

[48] T. B. Anderson and Roy Jackson. "Fluid Mechanical Description of Fluidized Beds. Equations of Motion". In: *Industrial & Engineering Chemistry Fundamentals* 6.4 (Nov. 1967), pp. 527–539. ISSN: 0196-4313. DOI: 10.1021/i160024a007.

[49] Jesse Capecelatro and Olivier Desjardins. "An Euler–Lagrange Strategy for Simulating Particle-Laden Flows". In: *Journal of Computational Physics* 238 (Apr. 2013), pp. 1–31. ISSN: 00219991. DOI: 10.1016/j.jcp.2012.12.015.

[50] Toni El Geitani, Shahab Golshan, and Bruno Blais. "A High-Order Stabilized Solver for the Volume Averaged Navier-Stokes Equations". In: *International Journal for Numerical Methods in Fluids* 95.6 (2023), pp. 1011–1033. ISSN: 1097-0363. DOI: 10.1002/fld.5182.

[51] ZY Zhou et al. “Discrete particle simulation of particle–fluid flow: model formulations and their applicability”. In: *Journal of Fluid Mechanics* 661 (2010), pp. 482–510.

[52] Zekun Wang, Yujun Teng, and Moubin Liu. “A semi-resolved CFD–DEM approach for particulate flows with kernel based approximation and Hilbert curve based searching strategy”. In: *Journal of Computational Physics* 384 (2019), pp. 151–169.

[53] Toni El Geitani and Bruno Blais. “Quadrature-centered averaging scheme for accurate and continuous void fraction calculation in computational fluid dynamics–discrete element method simulations”. In: *Industrial & Engineering Chemistry Research* 62.12 (2023), pp. 5394–5407.

[54] Matthieu Constant. “Simulations of immersed granular flows using an unresolved FEM-DEM model”. PhD thesis. UCL-Université Catholique de Louvain, 2020.

[55] Matthieu Constant et al. “Implementation of an Unresolved Stabilised FEM–DEM Model to Solve Immersed Granular Flows”. In: *Computational Particle Mechanics* (Sept. 2018). ISSN: 2196-4378, 2196-4386. DOI: 10.1007/s40571-018-0209-4.

[56] M. Constant et al. “Simulation of Air Invasion in Immersed Granular Beds with an Unresolved FEM–DEM Model”. In: *Computational Particle Mechanics* (Sept. 2020). ISSN: 2196-4386. DOI: 10.1007/s40571-020-00351-4.

[57] M. Constant et al. “Numerical investigation of the density sorting of grains using water jigging”. In: *Powder Technology* 393 (2021), pp. 705–721.

[58] Nathan Coppin. “Numerical methods for flows of immersed grain clusters”. PhD thesis. UCL-Université Catholique de Louvain, 2023.

[59] Nathan Coppin et al. “Numerical Analysis of the Drag on a Rigid Body in an Immersed Granular Flow”. In: *Particles 2021*. Hamburg, 2021.

[60] Nathan Coppin et al. “Collapse dynamics of two-dimensional dry and immersed granular columns of elongated grains”. In: *Physical Review Fluids* 8.9 (2023), p. 094303.

[61] Fangye Lin et al. *Deep Spontaneous Penetration of a Water Droplet into Hot Granular Materials*. Preprint. In Review, Dec. 2020. DOI: 10.21203/rs.3.rs-103868/v1.

[62] Alessandro Franci et al. “PFEM–DEM for particle-laden flows with free surface”. In: *Computational Particle Mechanics* 7 (2020), pp. 101–120.

[63] Wladimir Sarlin et al. “Nonlinear regimes of tsunami waves generated by a granular collapse”. In: *Journal of Fluid Mechanics* 919 (2021), R6.

[64] Hermann M Fritz, Fahad Mohammed, and Jeseon Yoo. "Lituya Bay landslide impact generated mega-tsunami 50 th Anniversary". In: *Tsunami Science four years after the 2004 Indian ocean tsunami: Part II: Observation and data analysis* (2009), pp. 153–175.

[65] Pierre Jop, Yoël Forterre, and Olivier Pouliquen. "A constitutive law for dense granular flows". In: *Nature* 441.7094 (2006), pp. 727–730.

[66] Ken Kamrin and Georg Koval. "Nonlocal constitutive relation for steady granular flow". In: *Physical review letters* 108.17 (2012), p. 178301.

[67] Olivier Pouliquen et al. "Flow of dense granular material: towards simple constitutive laws". In: *Journal of Statistical Mechanics: Theory and Experiment* 2006.07 (2006), P07020.

[68] Olivier Ozenda, Pierre Saramito, and Guillaume Chambon. "Shear–induced migration in concentrated suspensions: particle mass conservation, contact pressure and jamming". In: *Journal of Non-Newtonian Fluid Mechanics* 304 (2022), p. 104805.

[69] John G Rosser et al. "Investigation of Jamming Phenomenon in a Direct Reduction Furnace Pellet Feed System Using the Discrete Element Method". In: *Dynamics* 3.4 (2023), pp. 711–736.

[70] Federico A Tavarez and Michael E Plesha. "Discrete element method for modelling solid and particulate materials". In: *International journal for numerical methods in engineering* 70.4 (2007), pp. 379–404.

[71] ZX Yang, J Yang, and LZ Wang. "On the influence of inter-particle friction and dilatancy in granular materials: a numerical analysis". In: *Granular matter* 14 (2012), pp. 433–447.

[72] Kevin Francis Malone and Bao Hua Xu. "Determination of contact parameters for discrete element method simulations of granular systems". In: *Particuology* 6.6 (2008), pp. 521–528.

[73] Michel Jean. "The non-smooth contact dynamics method". In: *Computer methods in applied mechanics and engineering* 177.3-4 (1999), pp. 235–257.

[74] Frédéric Dubois, Vincent Acary, and Michel Jean. "The Contact Dynamics method: A nonsmooth story". In: *Comptes Rendus Mécanique* 346.3 (2018), pp. 247–262.

[75] Michel Jean and Jean Jacques Moreau. "Unilaterality and dry friction in the dynamics of rigid body collections". In: *1st Contact Mechanics International Symposium*. 1992, pp. 31–48.

[76] Jean J Moreau. "Unilateral contact and dry friction in finite freedom dynamics". In: *Nonsmooth mechanics and Applications*. Springer, 1988, pp. 1–82.

[77] Mihai Anitescu and Alessandro Tasora. “An iterative approach for cone complementarity problems for nonsmooth dynamics”. In: *Computational Optimization and Applications* 47.2 (2010), pp. 207–235.

[78] Mathieu Renouf and Pierre Alart. “Conjugate gradient type algorithms for frictional multi-contact problems: applications to granular materials”. In: *Computer Methods in Applied Mechanics and Engineering* 194.18-20 (2005), pp. 2019–2041.

[79] Efstathios E Michaelides, Martin Sommerfeld, and Berend van Wachem. *Multiphase flows with droplets and particles*. CRC Press, 2022.

[80] CB Rogers and JK Eaton. “The effect of small particles on fluid turbulence in a flat-plate, turbulent boundary layer in air”. In: *Physics of Fluids A: Fluid Dynamics* 3.5 (1991), pp. 928–937.

[81] Clayton T Crowe. “On models for turbulence modulation in fluid–particle flows”. In: *International Journal of Multiphase Flow* 26.5 (2000), pp. 719–727.

[82] Albert Einstein. “Eine neue bestimmung der moleküldimensionen”. PhD thesis. ETH Zurich, 1905.

[83] DZ Zhang and A Prosperetti. “Momentum and energy equations for disperse two-phase flows and their closure for dilute suspensions”. In: *International journal of multiphase flow* 23.3 (1997), pp. 425–453.

[84] Neelesh A Patankar and Daniel D Joseph. “Modeling and numerical simulation of particulate flows by the Eulerian–Lagrangian approach”. In: *International journal of multiphase flow* 27.10 (2001), pp. 1659–1684.

[85] Alberto Di Renzo and Francesco Paolo Di Maio. “Homogeneous and bubbling fluidization regimes in DEM–CFD simulations: hydrodynamic stability of gas and liquid fluidized beds”. In: *Chemical engineering science* 62.1-2 (2007), pp. 116–130.

[86] Ivo Babuška. “The finite element method with Lagrangian multipliers”. In: *Numerische Mathematik* 20.3 (1973), pp. 179–192.

[87] Franco Brezzi and Juhani Pitkäranta. “On the stabilization of finite element approximations of the Stokes equations”. In: *Efficient solutions of elliptic systems*. Springer, 1984, pp. 11–19.

[88] T.E. Tezduyar et al. “Incompressible flow computations with stabilized bilinear and linear equal-order interpolation velocity-pressure elements”. In: *Computer Methods in Applied Mechanics and Engineering* 95 (1992), pp. 221–242.

[89] A. N. Brooks and T. J. R. Hughes. “Streamline upwind/Petrov-Galerkin formulations for convection dominated flows with particular emphasis on the incompressible Navier-Stokes equations”. In: *Computer methods in applied mechanics and engineering* 32.1-3 (1982), pp. 199–259.

[90] T. E. Tezduyar and Y. Osawa. “Finite element stabilization parameters computed from element matrices and vectors”. In: *Computer Methods in Applied Mechanics and Engineering* 190.3-4 (2000), pp. 411–430.

[91] Chuan Miao Chen and Vidar Thomée. “The lumped mass finite element method for a parabolic problem”. In: *The ANZIAM Journal* 26.3 (1985), pp. 329–354.

[92] Daniel A. Clarke et al. “Investigation of Void Fraction Schemes for Use with CFD-DEM Simulations of Fluidized Beds”. In: *Industrial & Engineering Chemistry Research* 57.8 (Feb. 2018), pp. 3002–3013. ISSN: 0888-5885. DOI: 10.1021/acs.iecr.7b04638.

[93] Zekun Wang and Moubin Liu. “Semi-resolved CFD–DEM for thermal particulate flows with applications to fluidized beds”. In: *International Journal of Heat and Mass Transfer* 159 (2020), p. 120150.

[94] Thomas Engels et al. “Numerical simulation of fluid–structure interaction with the volume penalization method”. In: *Journal of Computational Physics* 281 (2015), pp. 96–115.

[95] Ramakrishnan Thirumalaisamy and Amneet Pal Singh Bhalla. “A consistent, volume preserving, and adaptive mesh refinement–based framework for modeling non–isothermal gas–liquid–solid flows with phase change”. In: *International Journal of Multiphase Flow* 183 (2025).

[96] A Piquet, Olivier Roussel, and Abdellah Hadjadj. “A comparative study of Brinkman penalization and direct-forcing immersed boundary methods for compressible viscous flows”. In: *Computers & Fluids* 136 (2016), pp. 272–284.

[97] Jan Ludvig Vinningland et al. “Experiments and simulations of a gravitational granular flow instability”. In: *Physical Review E—Statistical, Nonlinear, and Soft Matter Physics* 76.5 (2007), p. 051306.

[98] Geoffrey Ingram Taylor. “The instability of liquid surfaces when accelerated in a direction perpendicular to their planes. I”. In: *Proceedings of the Royal Society of London. Series A. Mathematical and Physical Sciences* 201.1065 (1950), pp. 192–196.

[99] Jan Ludvig Vinningland et al. “Size invariance of the granular Rayleigh-Taylor instability”. In: *Physical Review E—Statistical, Nonlinear, and Soft Matter Physics* 81.4 (2010), p. 041308.

[100] Sige Peng and John D Rice. “Measuring critical gradients for soil loosening and initiation of backward erosion-piping mechanism”. In: *Journal of Geotechnical and Geoenvironmental Engineering* 146.8 (2020), p. 04020069.

[101] Kak Namkoong, Jung Yul Yoo, and Hyoung G Choi. "Numerical analysis of two-dimensional motion of a freely falling circular cylinder in an infinite fluid". In: *Journal of Fluid Mechanics* 604 (2008), pp. 33–53.

[102] Zhi-Gang Feng and Efstathios E Michaelides. "The immersed boundary-lattice Boltzmann method for solving fluid–particles interaction problems". In: *Journal of computational physics* 195.2 (2004), pp. 602–628.

[103] L Wang, ZL Guo, and JC3198060 Mi. "Drafting, kissing and tumbling process of two particles with different sizes". In: *Computers & Fluids* 96 (2014), pp. 20–34.

[104] Sudeshna Ghosh and Manish Kumar. "Study of drafting, kissing and tumbling process of two particles with different sizes and densities using immersed boundary method in a confined medium". In: *Applied Mathematics and Computation* 386 (2020), p. 125411.

[105] Prabir Basu. *Circulating Fluidized Bed Boilers: Design, Operation and Maintenance*. Cham: Springer International Publishing, 2015. ISBN: 978-3-319-06172-6 978-3-319-06173-3. DOI: 10.1007/978-3-319-06173-3.

[106] Chanchal Loha et al. "ChemInform Abstract: Advances in Mathematical Modeling of Fluidized Bed Gasification". In: *Renewable and Sustainable Energy Reviews* 40 (Dec. 2014), pp. 688–715. DOI: 10.1016/j.rser.2014.07.199.

[107] David Quéré. "Leidenfrost Dynamics". In: *Annual Review of Fluid Mechanics* 45.1 (Jan. 2013), pp. 197–215. ISSN: 0066-4189, 1545-4479. DOI: 10.1146/annurev-fluid-011212-140709.

[108] Lucia Rueda Villegas et al. "A Ghost Fluid/Level Set Method for Boiling Flows and Liquid Evaporation: Application to the Leidenfrost Effect". In: *Journal of Computational Physics* 316 (July 2016), pp. 789–813. ISSN: 0021-9991. DOI: 10.1016/j.jcp.2016.04.031.

[109] *A High-order Stabilized Solver for the Volume Averaged Navier-Stokes Equations - Geitani - 2023 - International Journal for Numerical Methods in Fluids - Wiley Online Library*.

[110] Khuram Walayat et al. "An Efficient Multi-Grid Finite Element Fictitious Boundary Method for Particulate Flows with Thermal Convection". In: *International Journal of Heat and Mass Transfer* 126 (Nov. 2018), pp. 452–465. ISSN: 0017-9310. DOI: 10.1016/j.ijheatmasstransfer.2018.05.007.

[111] *CFD-DEM Simulation of Heat Transfer in Fluidized Beds: Model Verification, Validation, and Application | Elsevier Enhanced Reader*. DOI: 10.1016/j.ces.2018.12.031.

[112] WE Ranz. "Evaporation from Drops-I and-II". In: 48 (1952), pp. 141–146.

[113] I. C. Kemp, R. E. Bahu, and H. S. Pasley. "model development and experimental studies of vertical pneumatic conveying dryers". In: *DRYING TECHNOLOGY* (May 2007). ISSN: 1323-1340. DOI: 10.1080/07373939408961008.

[114] J Li and D.J Mason. "A Computational Investigation of Transient Heat Transfer in Pneumatic Transport of Granular Particles". In: *Powder Technology* 112.3 (Oct. 2000), pp. 273–282. ISSN: 00325910. DOI: 10.1016/S0032-5910(00)00302-8.

[115] N. Wakao and T. Funazkri. "Effect of Fluid Dispersion Coefficients on Particle-to-Fluid Mass Transfer Coefficients in Packed Beds: Correlation of Sherwood Numbers". In: *Chemical Engineering Science* 33.10 (Jan. 1978), pp. 1375–1384. ISSN: 0009-2509. DOI: 10.1016/0009-2509(78)85120-3.

[116] A. V. Patil, E. A. J. F. Peters, and J. A. M. Kuipers. "Comparison of CFD–DEM Heat Transfer Simulations with Infrared/Visual Measurements". In: *Chemical Engineering Journal* 277 (Oct. 2015), pp. 388–401. ISSN: 1385-8947. DOI: 10.1016/j.cej.2015.04.131.

[117] Farhang Radjaï and Frédéric Dubois. "Modélisation numérique discrète des matériaux granulaires". In: ().

[118] George Keith Batchelor and RW O'brien. "Thermal or Electrical Conduction through a Granular Material". In: *Proceedings of the Royal Society of London. A. Mathematical and Physical Sciences* 355.1682 (1977), pp. 313–333.

[119] M. Michael Yovanovich. "Thermal Contact Resistance across Elastically Deformed Spheres." In: *Journal of Spacecraft and Rockets* 4.1 (1967), pp. 119–122. ISSN: 0022-4650. DOI: 10.2514/3.28821.

[120] Adrian Bejan and Allan D. Kraus. *Heat Transfer Handbook*. John Wiley & Sons, June 2003. ISBN: 978-0-471-39015-2.

[121] Michel Henry et al. "Multiscale FEM-DEM model for spontaneous droplet digging in a hot granular bed". In: *International Journal of Heat and Mass Transfer* 241 (2025), p. 126755.

[122] Zhipeng Duan and Yuanyuan Duan. "Sphere Drag and Heat Transfer". In: *Scientific Reports* 5 (July 2015). DOI: 10.1038/srep12304.

[123] C Yu Wen. "Mechanics of Fluidization". In: *Fluid Particle Technology, Chem. Eng. Progress. Symposium Series* 62 (1966), pp. 100–111.

[124] James De Acetis and George Thodos. *Mass and Heat Transfer in Flow of Gases Through Spherical Packings*. Research-Article. May 2002. DOI: 10.1021/ie50612a026.

[125] Walter Komarnicky. “Effect of Packing Geometry on Heat and Mass Transfer in Stacked Beds of Spheres”. PhD thesis. University of British Columbia, 1956. DOI: 10.14288/1.0059067.

[126] G. F. Malling and George Thodos. “Analogy between Mass and Heat Transfer in Beds of Spheres: Contributions Due to End Effects”. In: *International Journal of Heat and Mass Transfer* 10.4 (Apr. 1967), pp. 489–498. ISSN: 0017-9310. DOI: 10.1016/0017-9310(67)90169-X.

[127] A. S. Gupta and G. Thodos. “Mass and heat transfer in the flow of fluids through fixed and fluidized beds of spherical particles”. In: *A.I.Ch.E. (Am. Inst. Chem. Engrs.) J.* Vol: 8 (Nov. 1962). DOI: 10.1002/aic.690080509.

[128] Charles R Wilke and OA Hougen. “Mass transfer in the flow of gases through granular solids extended to low modified Reynolds numbers”. In: *Trans. Am. Inst. Chem. Eng* 41.4 (1945), pp. 445–451.

[129] CN Satterfield. “Simultaneous Heat and Mass Transfer in a Duffusion-Controlled Chemical Reaction ; Part II : Studies in a Packed Bed”. In: *Chem. Eng. Prog.* 50 (1954), pp. 504–510.

[130] Jian Yang et al. “Experimental Analysis of Forced Convective Heat Transfer in Novel Structured Packed Beds of Particles”. In: *Chemical Engineering Science* 71 (Mar. 2012), pp. 126–137. ISSN: 0009-2509. DOI: 10.1016/j.ces.2011.12.005.

[131] John R Grace. “Shapes and velocities of single drops and bubbles moving freely through immisicible liquids”. In: *Trans. Inst. Chem. Eng.* 54 (1976), pp. 167–173.

[132] Charles Voivret et al. “Space-filling properties of polydisperse granular media”. In: *Physical Review E* 76.2 (2007), p. 021301.

[133] Fatima Zahra El Korchi, Frédéric Jamin, and Moulay Saïd El Youssoufi. “Etude Expérimentale à l’échelle Locale de La Coalescence de Ponts Capillaires Dans Les Sols Granulaires”. In: *35èmes Rencontres Universitaires de Génie Civil*. Actes Des 35èmes Rencontres Universitaires de Génie Civil. Nantes, France, May 2017.

[134] Steven N Ward. “Landslide tsunami”. In: *Journal of Geophysical Research: Solid Earth* 106.B6 (2001), pp. 11201–11215.

[135] Stéphane Abadie et al. “Numerical simulation of waves generated by landslides using a multiple-fluid Navier–Stokes model”. In: *Coastal engineering* 57.9 (2010), pp. 779–794.

[136] Cyril W Hirt and Billy D Nichols. “Volume of fluid (VOF) method for the dynamics of free boundaries”. In: *Journal of computational physics* 39.1 (1981), pp. 201–225.

[137] Mark Sussman et al. “An improved level set method for incompressible two-phase flows”. In: *Computers & Fluids* 27.5-6 (1998), pp. 663–680.

[138] Thomas Leyssens et al. “A Delaunay refinement algorithm for the particle finite element method applied to free surface flows”. In: *International Journal for Numerical Methods in Engineering* (2024), e7554.

[139] Joe J Monaghan. “Smoothed particle hydrodynamics”. In: *Reports on progress in physics* 68.8 (2005), p. 1703.

[140] Deborah Sulsky, Zhen Chen, and Howard L Schreyer. “A particle method for history-dependent materials”. In: *Computer methods in applied mechanics and engineering* 118.1-2 (1994), pp. 179–196.

[141] Andrea Pasqua, Alessandro Leonardi, and Marina Pirulli. “Coupling Depth-Averaged and 3D numerical models for the simulation of granular flows”. In: *Computers and Geotechnics* 149 (2022), p. 104879.

[142] Célestin Marot, Jeanne Pellerin, and Jean-François Remacle. “One machine, one minute, three billion tetrahedra”. In: *International Journal for Numerical Methods in Engineering* 117.9 (2019), pp. 967–990.

[143] Jia Mao et al. “A resolved CFD–DEM approach for the simulation of landslides and impulse waves”. In: *Computer Methods in Applied Mechanics and Engineering* 359 (2020), p. 112750.

[144] Fengze Xie, Weiwen Zhao, and Decheng Wan. “Numerical simulations of liquid-solid flows with free surface by coupling IMPS and DEM”. In: *Applied Ocean Research* 114 (2021), p. 102771.

[145] Xiaosong Sun, Mikio Sakai, and Yoshinori Yamada. “Three-dimensional simulation of a solid–liquid flow by the DEM–SPH method”. In: *Journal of Computational Physics* 248 (2013), pp. 147–176.

[146] Alessandro Franci et al. “3D simulation of Vajont disaster. Part 1: Numerical formulation and validation”. In: *Engineering Geology* 279 (2020), p. 105854.

[147] Herbert Edelsbrunner, David Kirkpatrick, and Raimund Seidel. “On the shape of a set of points in the plane”. In: *IEEE Transactions on information theory* 29.4 (1983), pp. 551–559.

[148] L Paul Chew. “Guaranteed-quality mesh generation for curved surfaces”. In: *Proceedings of the ninth annual symposium on Computational geometry* (1993), pp. 274–280.

[149] Pratik Suchde and Jörg Kuhnert. “Point cloud movement for fully Lagrangian meshfree methods”. In: *Journal of Computational and Applied Mathematics* 340 (2018), pp. 89–100.

[150] Marco Lucio Cerquaglia et al. “Free-slip boundary conditions for simulating free-surface incompressible flows through the particle finite element method”. In: *International Journal for numerical methods in engineering* 110.10 (2017), pp. 921–946.

[151] Eugenio Onate et al. “Advances in the particle finite element method (PFEM) for solving coupled problems in engineering”. In: *Particle-based methods: fundamentals and applications* (2011), pp. 1–49.

[152] Manon Robbe-Saule et al. “Experimental investigation of tsunami waves generated by granular collapse into water”. In: *Journal of Fluid Mechanics* 907 (2021), A11.

[153] Severin Strobl, Arno Formella, and Thorsten Pöschel. “Exact Calculation of the Overlap Volume of Spheres and Mesh Elements”. In: *Journal of Computational Physics* 311 (Apr. 2016), pp. 158–172. ISSN: 0021-9991. DOI: 10.1016/j.jcp.2016.02.003.

[154] Ellis Horowitz and Marco Papa. “Polygon clipping: Analysis and experiences”. In: *Theoretical Studies in Computer Science*. Elsevier, 1992, pp. 315–339.

[155] Inbar Vaknin et al. “Gas seepage and pockmark formation from subsurface reservoirs: Insights from table-top experiments”. In: *Journal of Geophysical Research: Solid Earth* 129.4 (2024), e2023JB028255.

[156] Erik Burman and Paolo Zunino. “Numerical approximation of large contrast problems with the unfitted Nitsche method”. In: *Frontiers in Numerical Analysis-Durham 2010*. Springer, 2011, pp. 227–282.

[157] Peter Hansbo and Mats G Larson. “Nitsche’s finite element method for model coupling in elasticity”. In: *Computer Methods in Applied Mechanics and Engineering* 392 (2022), p. 114707.